

学位論文（要約）

Strong electric field processes
in solids induced by
an intense mid-infrared light source

（高強度中赤外光源によって誘起される
固体中の強電場過程の研究）

平成 28 年 12 月 博士（理学）申請

東京大学大学院理学系研究科
物理学専攻

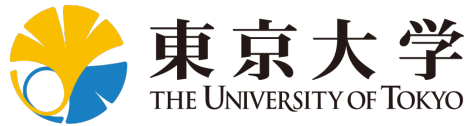
金島 圭佑

Strong electric field processes in solids induced by
an intense mid-infrared light source

Keisuke Kaneshima

December 20, 2016

The University of Tokyo



Department of Physics, Faculty of Science
The Institute for Solid State Physics
Prof. Itatani's Group

Dissertation

Strong electric field processes in solids induced by an intense mid-infrared light source

Keisuke Kaneshima

- Chief Reviewer* Prof. Dr. Junji Yumoto
Department of Physics, Faculty of Science
The University of Tokyo
- Reviewer* Prof. Dr. Fumio Komori
The Institute for Solid State Physics
The University of Tokyo
- Reviewer* Prof. Dr. Shingo Katsumoto
The Institute for Solid State Physics
The University of Tokyo
- Reviewer* Prof. Dr. Takeo Kato
The Institute for Solid State Physics
The University of Tokyo
- Reviewer* Dr. Takuro Ideguchi
Department of Physics, Faculty of Science
The University of Tokyo
- Supervisor* Prof. Dr. Jiro Itatani
The Institute for Solid State Physics
The University of Tokyo

December 20, 2016

Keisuke Kaneshima

Strong electric field processes in solids induced by an intense mid-infrared light source

Dissertation, December 20, 2016

Reviewers: Prof. Dr. Junji Yumoto, Prof. Dr. Fumio Komori, Prof. Dr. Shingo Katsumoto,
Prof. Dr. Takeo Kato, and Dr. Takuro Ideguchi

Supervisor: Prof. Dr. Jiro Itatani

The University of Tokyo

Prof. Itatani's Group

The Institute for Solid State Physics

5-1-5 Kashiwanoha

277-8581 Kashiwa

Abstract

Recent progress of ultrafast laser technology has opened a new research area in strong-field physics where atoms and molecules in strong laser fields exhibit extremely nonlinear responses such as tunnel ionization and high harmonic generation. Using such extreme nonlinearity, attosecond science has been well developed in the past decade, and our understanding of ultrafast electron dynamics in atoms and molecules have been expanded tremendously. Meanwhile, strong field physics in condensed matters is still unexplored because it is difficult to nondestructively apply intense optical fields to solids. In order to apply strong electric fields to solids, intense and long-wavelength sources are needed whose photon energy is much smaller than their bandgap energies. We propose and demonstrate a novel scheme to produce intense mid-infrared pulses with stable carrier-envelope phases. We successfully apply electric fields of several tens MV/cm to crystalline solids without inducing optical breakdown, and observe extremely nonlinear responses such as high harmonic generation and field-sensitive change in transient absorption.

The thesis contains three achievements. First is the generation and complete characterization of carrier-envelope phase-stable intense mid-infrared fields with a peak electric field strength exceeding 50 MV/cm. A newly developed technique of optical parametric amplification, namely dual-wavelength optical parametric amplification (OPA), is demonstrated to produce intense mid-infrared pulses. Owing to the intrinsic simplicity of the technique, a long-term carrier-envelope phase stability is assured. A novel scheme for the generation of 6.5-fs visible pulses is also demonstrated and used for the complete characterization of the mid-infrared fields. This scheme provides ultrashort visible pulses with smooth and stable spectra which are crucial to be used as a probe in sub-cycle spectroscopy. Complete waveform characterization of the mid-infrared field is realized via electro-optic sampling with a LGS crystal which has an extremely broad transparency range from ultraviolet to mid-infrared.

Second achievement is the generation of high harmonics in a crystalline solid with ellipsometric analysis to trace the electron dynamics in the band structure. High harmonics are produced in a semiconductor GaSe crystal, which cover the spectral range from mid-infrared to visible, extending beyond the bandgap energy of ~ 2 eV. We employ ellipsometric detection of emitted harmonics, and observe unusual appearance of the polarization components in the direction perpendicu-

lar to the driving mid-infrared field. Detailed analysis shows that the transition from the perturbative to non-perturbative regime occurs around ~ 10 MV/cm. The polarization rotation of high harmonics reflects the electronic structure of solids, especially the band gradients near the Brillouin-zone boundary. This method, high harmonic ellipsometry, can extract rich information on the electron dynamics and band structures, which is analogous to the high harmonic spectroscopy of atoms and molecules in attosecond sciences.

Third, we demonstrate the sub-cycle resolved transient absorption spectroscopy of a semiconductor GaSe crystal around its bandgap. Under the presence of weak electric-fields (< 10 MV/cm), Franz-Keldysh oscillations above the bandgap are clearly observed. At high electric fields (> 10 MV/cm), we discover novel absorption features where the absorption spectrum is modulated on the sub-cycle time scale, which suggest strong-field-driven coherent electron dynamics around the bandgap.

This series of experimental works is just the beginning of the strong field physics in condensed matters. Further development of mid-infrared sources and the theory of strongly-driven electronic states will deepen our understanding of extremely fast electron processes in solids and may become a foundation of new optical technologies in future.

Contents

I	General Introduction	1
1	Part I: Introduction	3
1.1	The birth of extreme nonlinear optics	3
2	Theoretical framework of strong electric field processes	7
2.1	Two-level system in strong electric fields	7
2.2	Atoms and molecules in strong electric fields	12
2.3	Ionization in strong electric fields	15
2.4	Strong-field-driven processes in solids	21
3	Experiments of strong electric field processes in solids	29
3.1	Sub-cycle spectroscopy	29
3.2	High harmonic generation in crystalline solids	34
3.3	Franz-Keldysh effect (FKE) induced by strong MIR fields	40
II	Development of an intense mid-infrared light sources	43
4	Part II: introduction and summary	45
5	Optical parametric amplifiers	47
5.1	Phase matching in OPA	47
5.2	CEP stabilization in nonlinear wave-mixing processes	50
6	Generation of carrier-envelope phase-stable intense mid-infrared pulses	53
6.1	Experiment	53
6.2	Summary	55
7	Generation of spectrally stable 6.5-fs visible pulses	59
7.1	Motivations	59
7.2	Experiment	59
7.3	Summary	64
8	Waveform characterization of MIR light fields	65
8.1	Electro-optic sampling of the MIR field	65
8.2	Summary	73

III Strong electric field processes in solids induced by an intense mid-infrared light source	75
9 Part III: introduction and summary	77
10 High harmonic ellipsometry	79
10.1 Motivations	79
10.2 Experiment	79
10.3 Discussions	85
10.4 Summary	91
11 Sub-cycle transient absorption spectroscopy	95
11.1 Motivation	95
11.2 Experiment	95
11.3 Discussions	103
11.4 Summary	103
IV Conclusion and outlook	105
12 Conclusion and outlook	107
Bibliography	113
List of Publications	125
Acknowledgment	131

List of Figures

1.1	Concept of chirped pulse amplification.	4
1.2	Illustration of carrier-envelope phase (CEP).	6
1.3	Concept of optical parametric chirped pulse amplification.	6
2.1	Illustration of conventional Rabi flopping and carrier-wave Rabi flopping.	10
2.2	Volkov sidebands for a ponderomotive energy of $\langle \mathcal{E}_{\text{kin}} \rangle / \hbar\omega_0 = 0.1, 1, 5$.	15
2.3	Illustration of tunneling of an electron out of a potential well.	16
2.4	Illustration of the instantaneous ionization rate versus the instantaneous laser electric field	18
2.5	Illustration of ionization of atoms via (a) electrostatic tunneling at large laser fields ($\gamma_K \ll 1$) and (b) multiphoton absorption at weak laser electric fields ($\gamma_K \gg 1$).	18
2.6	Schematic illustration of a typical high harmonic spectrum from atoms.	19
2.7	Schematic illustration of the valence and the conduction band of a direct gap semiconductor in the first Brillouin zone.	21
2.8	Radiated intensity spectrum I_{rad} for $\Omega_B/\omega_0 = 0.1, 1, 5$ according to (2.58).	25
2.9	Schematic drawing of Franz-Keldysh effect.	26
2.10	Schematic of absorption spectra of a three-dimensional semiconductor subject to static electric fields.	27
3.1	Schematic illustration of (a) <i>conventional</i> pump-probe spectroscopy, and (b) <i>sub-cycle</i> pump-probe spectroscopy.	30
3.2	Typical setup for strong-field THz-spectroscopy.	30
3.3	Attosecond transient absorption of SiO ₂	32
3.4	Strong-field conditions for ZnO.	35
3.5	MIR-driven HHG from bulk ZnO.	36
3.6	MIR-driven HHG from bulk GaSe.	37
3.7	Measured emission dynamics of MIR-driven HHG from bulk GaSe.	38
3.8	Transmission of a broadband probe pulses through a 350- μm -thick GaAs crystal as a function of time delay.	40
3.9	Wavelength dependence of electroabsorption in GaAs.	41
3.10	Scaling of the field induced redshift in the absorption edge for ZnO, and dependence of the yield of the MIR harmonics (9th to 21th) to the laser intensity.	42

5.1	Frequency and phase summation rules.	51
5.2	Comparison of inter-pulse and intra-pulse stabilization schemes.	52
6.1	Concept of the dual-wavelength OPA.	54
6.2	Schematic of the experimental setup.	55
6.3	WLG spectrum in a 4-mm-thick YAG plate.	56
6.4	Tunability of the dual-wavelength OPA.	56
6.5	Phase mismatch in 1-mm-thick LGS.	56
7.1	Schematic of the experimental setup.	60
7.2	(a) Measured reflectivity and (b) group delay of the band-stop mirror.	60
7.3	Relative group delays of 1-m-long air (black line), 0.5-mm-thick fused silica (red line), and 0.7-mm-thick CaF ₂ (blue dashed line).	61
7.4	Results of SHG-FROG measurement.	62
7.5	Beam profiles of the compressed pulse.	63
7.6	Results of the spectral stability measurement.	63
8.1	Schematic of the experimental setup of the timing-jitter measurement.	66
8.2	Single-shot interferogram in the timing-jitter measurement.	66
8.3	Result of the timing-jitter measurement.	67
8.4	Transmission spectra for 2-mm-thick Li-containing ternary chalcogenide crystals.	67
8.5	Phase mismatch of the DFG process between MIR components and 600-nm component for phase matching in <i>xy</i> -plane of a 100- μ m-thick LGS crystal.	68
8.6	Nonlinear wave mixing between the MIR pulses and the visible pulses in a 1-mm-thick LGS crystal.	69
8.7	Experimental setup for electro-optic sampling.	70
8.8	Schematic of the signal processing electronics.	70
8.9	MIR waveform measured by EOS.	72
8.10	Results of the knife edge measurement.	72
8.11	Tunability of the dual-wavelength OPA.	72
8.12	Time evolution of the electro-optically sampled MIR waveforms.	73
10.1	Top and perspective views of a unit of GaSe with indication of the MIR polarization and propagation directions.	80
10.2	High harmonics from a 100- μ m-thick GaSe crystal driven by the MIR fields generated via DFG in a 1-mm-thick LGS crystal.	80
10.3	High harmonics from a 100- μ m-thick GaSe crystal driven by the MIR fields generated via DFG in a 8-mm-thick LGS crystal.	81
10.4	Electric-field-strength dependence of the high harmonics from a 100- μ m-thick GaSe crystal.	81
10.5	Schematic of the experimental setup for high harmonic ellipsometry.	82

10.6	(a) MIR waveform measured by EOS and (b) its power spectrum. . . .	83
10.7	Intensity envelope of the waveform shown in Fig. 10.6.	83
10.8	Angle dependence of high harmonic spectra from a GaSe crystal. . . .	84
10.9	(a) MIR waveform measured by EOS and (b) its power spectrum. . . .	85
10.10	Intensity dependent change of the ϕ -dependence of the low-order harmonics.	86
10.11	Line plots of the THG intensities extracted from Fig. 10.10.	87
10.12	(a) Electric-field-strength dependence of the third harmonic intensities (blue: parallel, red: perpendicular) at $\phi=80^\circ$. (b) THG intensity ratio of the perpendicular components to the parallel.	88
10.13	Calculated dispersion of the lowest conduction band of GaSe.	91
10.14	Calculated high harmonic spectra.	92
11.1	MIR field applied and the measured transient transmission modulation ($\Delta T/T$).	96
11.2	Spectra of the transmitted visible probe pulses with and without the MIR fields.	97
11.3	Differential transmittance spectra $\Delta T/T$ extracted from Fig. 11.1 at several delays.	97
11.4	Differential transmittance spectra $\Delta T/T$ extracted from Fig. 11.1 at several delays where the applied MIR fields were > 10 MV/cm.	98
11.6	Measured transient transmission modulation ($\Delta T/T$) in a $10\text{-}\mu\text{m}$ -thick GaSe crystal at $\phi = 20$ [deg.].	99
11.7	Measured transient transmission modulation ($\Delta T/T$) in a $10\text{-}\mu\text{m}$ -thick GaSe crystal at $\phi = 50$ [deg.].	100
11.8	Measured transient transmission modulation ($\Delta T/T$) in a $10\text{-}\mu\text{m}$ -thick GaSe crystal at $\phi = 80$ [deg.].	100
11.9	Measured transient transmission modulation ($\Delta T/T$) in a $10\text{-}\mu\text{m}$ -thick GaSe crystal at $\phi = 110$ [deg.].	101
11.10	ϕ dependence of the sub-cycle $\Delta T/T$ modulation.	101
11.11	Modulation of $\Delta T/T$ with respect to the applied MIR fields.	102
11.12	Line plots of $\Delta T/T$ at the delay $\tau = 105$ and 118 fs of Fig. 11.8.	102
12.1	Picture of the laboratory taken in March 2014.	108
12.2	Picture of the laboratory taken in December 2015.	108
12.3	Layout of the developed laser system.	109
12.4	Absorption coefficients of water vapor and carbon dioxide in the air. . .	111

List of Tables

3.1	Previous studies of high harmonic generation from solids.	39
3.2	Previous studies of light-induced transient absorption of bulk crystals. .	42
5.1	Degenerate OPA schemes pumped below 1 μm	50
8.1	Overview of the transmission ranges of MIR nonlinear crystals.	68

Part I

General Introduction

Part I: Introduction

This thesis presents the development of novel light sources to study strong-electric-field-induced processes (> 10 MV/cm) in solids within a time scale of less than one optical cycle. At such high intensities, the nonlinear response of solids will become nonperturbative, i.e., optical response is determined not by the envelope of the oscillating electric fields, but by the instantaneous amplitudes and exact waveforms. Such novel nonlinear processes have become the basis of the new field called *extreme nonlinear optics*, which has led to the birth of attosecond sciences. In this introduction, I will briefly explain the important building blocks of intense ultrafast laser technologies and of strong field physics.

1.1 The birth of extreme nonlinear optics

1.1.1 Conventional nonlinear optics

Soon after the invention of ruby laser by Maimain in 1960 [1], the first experimental demonstration of nonlinear optical effect (i.e., second harmonic generation) was realized by Frenken in 1961 [2]. As the laser technology made progress in pulse duration and achievable intensities, such nonlinear response of matter had been regarded as general phenomena. The framework of perturbative nonlinear optics was established [3] where strong field effects are treated in a perturbative manner. In such treatments, polarization of matter P can be expanded in the Taylor series of the field amplitude E as

$$P = \epsilon_0 \left(\chi^{(1)} E + \chi^{(2)} E^2 + \chi^{(3)} E^3 + \dots \right), \quad (1.1)$$

where $\chi^{(n)}$ is n -th order susceptibility, and the n -th order term corresponds to a n -photon process. Another important feature of perturbative nonlinear optics is that nonlinear responses are determined by the envelope of the oscillating electric field. Today, this type of nonlinear optics has been widely used for frequency conversion of laser light, for example, extending the available spectral range of coherent light from THz to vacuum ultraviolet (VUV).

1.1.2 Progress of intense ultrashort pulse lasers

In the past three decades, ultrafast laser technologies have advanced tremendously in terms of pulse duration, peak power, and controllability. There have been many breakthroughs which can be categorized from the following viewpoints:

- Increase of pulse energy or peak intensity,
- Shortening of pulse durations,

- Precise control of pulse shape, polarization, and phase, and
- Extension of spectral region.

In the following, we will briefly overview the key technologies that are closely related to this thesis subject.

Chirped pulse amplification (CPA)

Amplification of femtosecond optical pulses in solid state lasers had been very difficult because of the high saturation fluence of laser media. When femtosecond pulses are amplified close to saturation fluence ($> 0.1 \text{ J/cm}^2$), peak intensity of the pulses exceeds the threshold of self focusing, resulting in a catastrophic damage of laser media. This problem was solved by chirped pulse amplification (CPA) invented by Strickland and Mourou in 1985 [4]. The concept of CPA is illustrated in Fig. 1.1. First, low-energy ultrashort laser pulses from a laser oscillator are sent to a dispersive optical setup with diffraction gratings to expand the pulse duration. This setup is called a pulse stretcher. The stretched (i.e., chirped) seed pulses are then amplified in solid-state laser amplifiers to saturation levels without nonlinear distortion and damage because the peak intensity is significantly lowered. Finally the amplified pulses are sent to a pulse compressor that consists of a pair of diffraction gratings to obtain high-energy ultrashort laser pulses. This CPA method has realized high-repetition-rate terawatt ($1 \text{ TW} = 10^{12} \text{ W}$) lasers with a tabletop size, or low-repetition-rate petawatt ($1 \text{ PW} = 10^{15} \text{ W}$) lasers with a building scale [5]. The emergence of such high-peak-power lasers opened wide opportunities in ultrafast strong field physics.

Nonlinear pulse compression

Extremely short pulse duration on the order of few cycles can be produced by nonlinear pulse compression [6]. Particularly, the development of Ti:sapphire CPA lasers has made possible the generation of intense few-cycle pulses in the near-infrared around 800 nm, corresponding to a photon energy of 1.55 eV and an optical cycle of 2.7 fs. The most successful method of pulse compression is

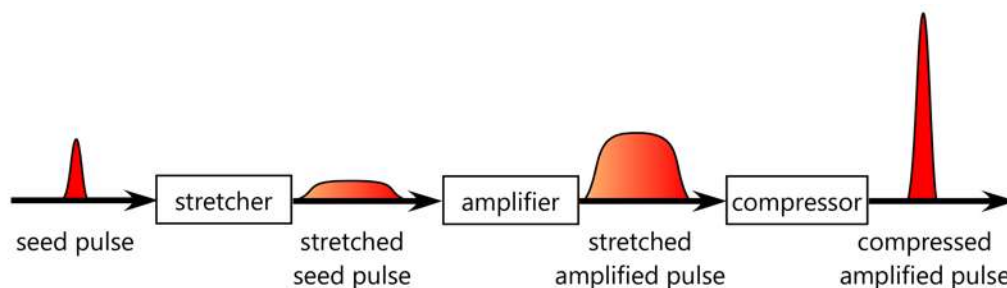


Fig. 1.1: Concept of chirped pulse amplification.

based on nonlinear propagation of femtosecond amplified pulses in a gas-filled hollow waveguide [7, 8], followed by precise dispersion compensation by chirped dielectric mirrors [9–11]. Typically a Ti:sapphire laser system with hollow-fiber pulse compression can produce 0.1 TW, 5 fs laser pulses at a repetition rate of 1 kHz [8].

Carrier-envelope phase (CEP) control

When the pulse duration of a laser pulse becomes close to a few cycles, the shape of electric waveform strongly depends on the phase of the carrier wave with respect to the field envelope. In the case of a mode-locked pulse train as shown in Fig. 1.2(a), the phase between the carrier wave and the position of the intensity envelope (*Carrier-Envelope Phase*, CEP) varies from pulse to pulse. Recent ultrafast laser technologies can detect and control CEP. When stabilized, we can obtain unchanged electric waveform as shown in Fig. 1.2(b). In the frequency domain, a pulse train with a stable CEP can be understood as a frequency comb where millions of monochromatic light fields are coherently superposed with constant frequency separation. In the time domain, intense CEP-stable pulses can be used to control strong field phenomena with sub-cycle temporal resolution.

Optical parametric amplification (OPA) and optical parametric chirped pulse amplification (OPCPA)

Optical parametric amplification is a method to coherently amplify optical pulses with parametric interaction between propagating optical waves in nonlinear crystals. This method has an advantage over laser amplification using population inversion because:

1. Gain spectra is not limited by the electronic structure of gain material, but by the phase matching condition. Therefore, we can amplify optical pulses in extreme wavelength (e.g., from IR to THz).
2. Since the parametric nonlinear crystal is transparent and does not store the energy, there are very little thermal load. This is suited for high-repetition-rate operation.

The CPA concept was also applied to optical parametric amplifiers (OPA), which is called the optical parametric chirped pulse amplification (OPCPA) method (Fig. 1.3).

Various OPCPA schemes have been demonstrated so far, covering the spectral range from UV to MIR, whose duration down to few cycles with stable CEPs, and the peak powers reaching the terawatt (TW) level and beyond.

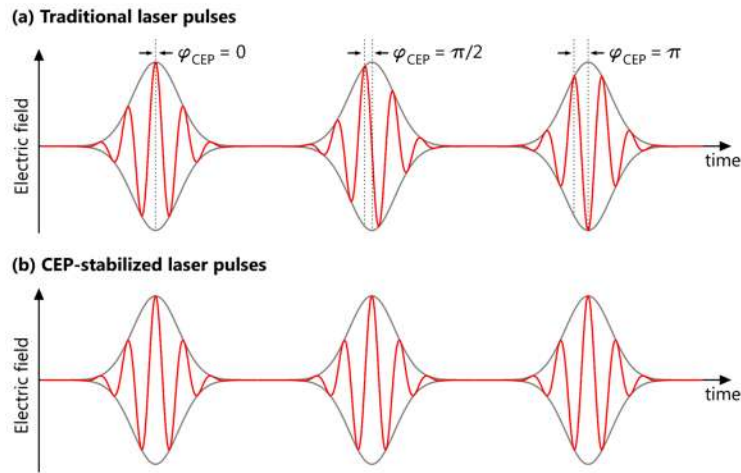


Fig. 1.2: Illustration of carrier-envelope phase (CEP). (a) Train of optical pulses from traditional pulsed lasers, (b) Train of optical pulses from CEP-stabilized lasers.

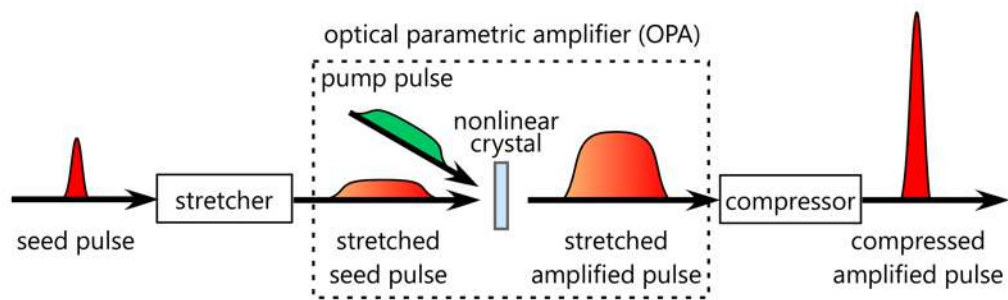


Fig. 1.3: Concept of OPCPA.

Theoretical framework of strong electric field processes

In this chapter, I will show the theoretical framework of strong electric field processes of various systems, starting with a two-level system. I will then show the case of isolated quantum system such as atoms and molecules with an emphasize on the dynamics of electron wavepackets in the continuum. Finally I will show the case of crystalline solids where electron wavepackets are driven by strong electric fields in the band structures. The theoretical description in this chapter is mostly based on the treatment in [12].

2.1 Two-level system in strong electric fields

We will start with a two-level system that interacts with strong electric fields. In spite of the simplicity of the system, classical and quantum treatments lead to fundamental concepts of Rabi energy and Rabi flopping. These concepts are closely related to high harmonic generation in solids via interband transition.

Classical analogue and Rabi energy

The equation of motion of an electron (charge $-e$, mass m_e) bound to a fixed positive charge with a restoring force is written as Eq. (2.1), where x is a displacement with respect to the fixed positive charge, and the restoring force is given by $\mathcal{D}x(t)$.

$$m_e \ddot{x}(t) + \mathcal{D}x(t) = -eE(t) . \quad (2.1)$$

The dots denote the derivative with respect to time t . The macroscopic polarization P is given by the product of the number of oscillators N_{osc} per volume V times the individual dipole moment $-ex$, i.e., $P = -e(N_{\text{osc}}/V)x$. The solution of Eq. (2.1) in the spectral domain is then given by

$$P(\omega) = \epsilon_0 \chi(\omega) E(\omega) . \quad (2.2)$$

Linear optical susceptibility $\chi(\omega)$ is given by

$$\begin{aligned} \chi(\omega) &= \frac{e^2 N_{\text{osc}}}{\epsilon_0 V m_e} \frac{1}{\Omega^2 - \omega^2} \\ &= \frac{e^2 N_{\text{osc}}}{\epsilon_0 V m_e} \frac{1}{2\Omega} \left(\frac{1}{\Omega - \omega} + \frac{1}{\Omega + \omega} \right) , \end{aligned} \quad (2.3)$$

where $\Omega = \sqrt{\mathcal{D}/m_e}$ is the characteristic frequency of this oscillator, which is analogous to the transition frequency of a two-level system. The susceptibility $\chi(\omega)$ has

poles at the two frequencies $\omega = \pm\Omega$. The pole in the positive frequency accounts for the linear optical response, while the pole in the negative frequency is the source of various nonlinear responses such as carrier-frequency Rabi flopping. By defining a dipole $d = e\hbar/(2m_e x_0 \Omega)$, one can write the equation of motion as

$$\ddot{u} + \Omega^2 u = 2\Omega\Omega_R(t) , \quad (2.4)$$

where $u = x/x_0$ is the normalized displacement, and the equation of motion is rewritten as

$$\hbar\Omega_R(t) = dE(t) . \quad (2.5)$$

The quantity $\Omega_R(t)$ has a unit of frequency and is called *Rabi frequency*. Equation (3.6) shows that d is the classical analogue of a dipole matrix element of the two-level system.

Quantum description of two-level system

Next, we will show a quantum treatment of a two-level system that consists of two lowest-energy states of an electron in a box of width L with infinite potential walls at $x = 0, L$. The time-dependent wavefunction for these two states are given by

$$\psi_1(x, t) = \sqrt{\frac{2}{L}} \sin\left(\frac{\pi}{L}x\right) e^{-i\frac{\mathcal{E}_1}{\hbar}t} = \psi_1(x)e^{-i\frac{\mathcal{E}_1}{\hbar}t} \quad (2.6)$$

$$\psi_2(x, t) = \sqrt{\frac{2}{L}} \sin\left(\frac{2\pi}{L}x\right) e^{-i\frac{\mathcal{E}_2}{\hbar}t} = \psi_2(x)e^{-i\frac{\mathcal{E}_2}{\hbar}t} \quad (2.7)$$

where $\mathcal{E}_1 = \hbar^2(\pi/L)^2/(2m_e)$ and $\mathcal{E}_2 = \hbar^2(2\pi/L)^2/(2m_e)$ are the corresponding eigenenergies. Note that the charge density of each eigen state (i.e., the absolute square of the wavefunction) is constant in time. Therefore, eigenstate alone cannot emit or absorb light. Only the superposition state such as,

$$\psi(x, t) = \frac{1}{\sqrt{2}} [\psi_1(x, t) + \psi_2(x, t)] \quad (2.8)$$

can have a time-dependent charge density $\rho(x, t)$ with

$$\rho(x, t) = -e|\psi(x, t)|^2 = -\frac{e}{2}|\psi_1(x, t) + \psi_2(x, t)|^2 \quad (2.9)$$

that oscillates in time. As a result, one gets a harmonic oscillation along x with the *transition frequency* Ω given by

$$\hbar\Omega = \mathcal{E}_2 - \mathcal{E}_1 . \quad (2.10)$$

We can see the analogy to the classical harmonic oscillator discussed in the previous section.

Usually a quantum system of interest is much smaller than the wavelength of light. In that case, we can apply the so-called *dipole approximation* where the interaction energy of a dipole d in a slowly oscillating electric field E is given by $-dE$. In quantum mechanics, d becomes the *dipole matrix element*, i.e.,

$$d = \langle \psi_2 | -ex | \psi_1 \rangle . \quad (2.11)$$

Bloch vector and carrier-wave Rabi flopping

The states of the two-level system can be described by the three real quantities forming the Bloch vector $(u, v, w)^T$, defined as

$$\begin{pmatrix} u \\ v \\ w \end{pmatrix} \equiv \begin{pmatrix} \langle c_1^\dagger c_2 \rangle + \langle c_2^\dagger c_1 \rangle \\ -i \left(\langle c_1^\dagger c_2 \rangle - \langle c_2^\dagger c_1 \rangle \right) \\ \langle c_2^\dagger c_2 \rangle - \langle c_1^\dagger c_1 \rangle \end{pmatrix} \quad (2.12)$$

where c^\dagger and c are the creation and annihilation operators, respectively. They create or annihilate electrons in states number 1 or 2. u and v are the real and imaginary parts of the optical polarization, respectively, and w is the population inversion.

The equation of motion of the Bloch vector (the Bloch equation) can describe the dynamics of the two-level system. Within the dipole approximation, but without employing the rotating wave approximation and without damping, the Bloch equation of the two-level system with transition frequency Ω can be written as

$$\begin{pmatrix} \dot{u} \\ \dot{v} \\ \dot{w} \end{pmatrix} = \begin{pmatrix} 0 & +\Omega & 0 \\ -\Omega & 0 & -2\Omega_R(t) \\ 0 & +2\Omega_R(t) & 0 \end{pmatrix} \begin{pmatrix} u \\ v \\ w \end{pmatrix} \quad (2.13)$$

Here we have introduced the *Rabi frequency* $\Omega_R(t)$ according to

$$\hbar\Omega_R = dE(t) \quad (2.14)$$

with a laser electric field

$$E(t) = \tilde{E}(t) \cos(\omega_0 t) . \quad (2.15)$$

Note that the definition of the Rabi energy, (2.14), is identical to that introduced in the classical analogue of a two-level system (2.5), except for a different expression for d in the classical case. Finally, considering that we have a number N of two-level systems per volume V , the optical polarization is given by

$$P(\mathbf{r}, t) = \frac{N}{V} du . \quad (2.16)$$

The (3×3) matrix in the equation of motion (2.13) of the Bloch vector only leads to rotations with two transition frequencies of Ω in the uv -plane and $2\Omega_R(t)$ in the vw -plane.

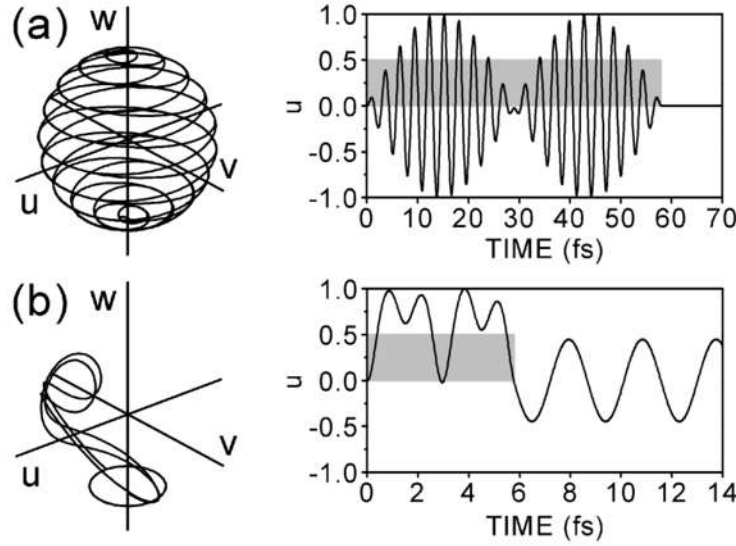


Fig. 2.1: Illustration of conventional Rabi flopping and carrier-wave Rabi flopping [15]. (a) Scheme of the trace of the Bloch vector for conventional Rabi flopping. Pulse duration is 20 optical cycles, envelope pulse area is $\Theta = 2\pi$. (b) Same for carrier-wave Rabi flopping. Pulse duration is 2 optical cycles, $\Theta = 2\pi$. The optical pulse envelopes are indicated by the grey areas.

Figures 2.1 show two cases with different field parameters. Figure 2.1(a) shows conventional Rabi flopping where the optical pulse contains many cycles and the field amplitude is small ($\Omega_R \ll \omega_0$). Meanwhile, Figure 2.1(b) shows the evolution of Bloch vector under a few-cycle strong electric field ($\Omega_R \sim \omega_0$). In this case, the Rabi frequency Ω_R itself oscillates with the carrier frequency of light ω_0 and periodically changes sign. This situation is called *carrier-wave Rabi flopping*, and is known to cause various interesting phenomena [13–19].

High harmonic generation from two-level system

As shown in the previous part, the dynamics of the Bloch vector without rotating approximation leads to unusual type of Rabi flopping. In this section, we will show an interesting case of the Bloch vector's motion that leads to high harmonic generation [18].

With a strong low-frequency electric field ($\Omega_R(t) > \omega_0$), we may apply the static-field approximation, i.e., Rabi frequency is approximated as a constant in time, $\Omega_R(t) = \Omega_R$. In this limit, the Bloch equation (2.13) can be analytically solved [18, 20, 21]. This leads to the Bloch vector

$$\begin{pmatrix} u(t) \\ v(t) \\ w(t) \end{pmatrix} = \mathcal{M}(t) \begin{pmatrix} u(0) \\ v(0) \\ w(0) \end{pmatrix} \quad (2.17)$$

with a (3×3) rotation matrix

$$\mathcal{M}(t) = \begin{pmatrix} \frac{4\Omega_R^2 + \Omega^2 \cos(\Omega_{\text{eff}} t)}{\Omega_{\text{eff}}^2} & \frac{\Omega}{\Omega_{\text{eff}}} \sin(\Omega_{\text{eff}} t) & \frac{2\Omega\Omega_R}{\Omega_{\text{eff}}^2} [\cos(\Omega_{\text{eff}} t) - 1] \\ -\frac{\Omega}{\Omega_{\text{eff}}} \sin(\Omega_{\text{eff}} t) & \cos(\Omega_{\text{eff}} t) & -\frac{2\Omega_R}{\Omega_{\text{eff}}} \sin(\Omega_{\text{eff}} t) \\ \frac{2\Omega\Omega_R}{\Omega_{\text{eff}}^2} [\cos(\Omega_{\text{eff}} t) - 1] & \frac{2\Omega_R}{\Omega_{\text{eff}}} \sin(\Omega_{\text{eff}} t) & \frac{\Omega^2 + 4\Omega_R^2 \cos(\Omega_{\text{eff}} t)}{\Omega_{\text{eff}}^2} \end{pmatrix} \quad (2.18)$$

The optical polarization $P(t) (\propto u(t))$ as well as the other two components of the Bloch vector oscillate with the effective frequency Ω_{eff} , which is given by

$$\Omega_{\text{eff}} = \sqrt{4\Omega_R^2 + \Omega^2} . \quad (2.19)$$

Since the Rabi frequency is proportional to the electric field strength, the cutoff-order of the harmonics is given by

$$N_{\text{cutoff}} = \frac{2\Omega_R}{\omega_0} . \quad (2.20)$$

In this model, the cutoff order of harmonics N_{cutoff} shows the linear dependence to the peak amplitude of the electric field.

2.2 Atoms and molecules in strong electric fields

2.2.1 Light-field-driven dynamics of electron wavepackets

Ponderomotive energy

Ponderomotive energy is the most important energy scale of an electron in an oscillating electric field. A free electron with mass m_e and charge $-e$, driven by the laser electric field $E(t)$ obeys Newton's second law according to

$$m_e \ddot{x}(t) = -eE(t) . \quad (2.21)$$

When the electric field $E(t)$ is given by

$$E(t) = \tilde{E}_0 \cos(\omega_0 t) , \quad (2.22)$$

the electron velocity $v(t) = \dot{x}(t)$ becomes

$$v(t) = -\frac{e\tilde{E}_0}{m_e\omega_0} \sin(\omega_0 t) . \quad (2.23)$$

Averaging the classical electron kinetic energy $\mathcal{E}_{\text{kin}}(t) = m_e v^2(t)/2$ over an optical cycle, we obtain the *ponderomotive energy* (also known as quiver energy)

$$\langle \mathcal{E}_{\text{kin}} \rangle = \frac{e^2 \tilde{E}_0^2}{4m_e \omega_0^2} . \quad (2.24)$$

The ponderomotive energy is proportional to the light intensity I ($\propto \tilde{E}_0^2$). The maximum kinetic energy of an electron is twice the ponderomotive energy, or $\langle \mathcal{E}_{\text{kin}} \rangle$.

Ponderomotive shift

Quantum mechanically, an electron in a laser electric field is analogous to that of the light field with carrier frequency ω_0 in a mode-locked laser oscillator. There, the electromagnetic wavepacket (the laser pulse) periodically oscillates back and forth between the laser mirrors with the round trip frequency f_r . This leads to sidebands of ω_0 - the frequency comb. These sidebands are rigidly upshifted by the carrier-envelope offset frequency f_ϕ as a result of the phase slip $\Delta\phi$ of the electromagnetic wavepacket from one roundtrip to the next.

In analogy to this, semiclassically speaking, the electron wavepacket in a periodic laser field acquires a quantum phase in one optical cycle, $\Delta\phi_e$, which is given by the cycle-average

$$\Delta\phi_e = \left\langle 2\pi \frac{(v_{\text{phase}} - v_{\text{group}}) \frac{2\pi}{\omega_0}}{\lambda_e} \right\rangle \quad (2.25)$$

with the electron de Broglie wavelength $\lambda_e = 2\pi/k_x$ and the period of light $2\pi/\omega_0$. Note that λ_e , v_{phase} , and v_{group} vary in time via $k_x = k_x(t)$. With the dispersion rela-

tion of vacuum electrons or crystal electrons within the effective-mass approximation

$$E_e(k_x) = \hbar\omega_e(k_x) = \frac{\hbar^2 k_x^2}{2m_e}, \quad (2.26)$$

and with $v_{\text{phase}} = \omega_e/k_x$ and $v_{\text{group}} = d\omega_e/dk_x$, we obtain the phase slip of the oscillating electron wavepacket from one optical cycle to the next

$$\begin{aligned} \Delta\phi_e &= \left\langle 2\pi \frac{\left(\frac{\hbar k_x}{2m_e} - 2\frac{\hbar k_x}{2m_e}\right) \frac{2\pi}{\omega_0}}{2\pi/k_x} \right\rangle \\ &= -2\pi \frac{\left\langle \frac{\hbar^2 k_x^2(t)}{2m_e} \right\rangle}{\hbar\omega_0} \\ &= -2\pi \frac{\langle \mathcal{E}_{\text{kin}} \rangle}{\hbar\omega_0}. \end{aligned} \quad (2.27)$$

Note that the minus sign is due to the fact that the electron group velocity is larger than its phase velocity, while for photon the situation is usually reversed.

According to (2.27), the phase slip becomes appreciable in magnitude if the ponderomotive energy approaches the photon energy, i.e.,

$$\frac{\langle \mathcal{E}_{\text{kin}} \rangle}{\hbar\omega_0} \approx 1. \quad (2.28)$$

Note that this ratio scales as $1/\omega_0^3$. Furthermore, in analogy to the light field in a laser cavity, we expect that the density of states of the combined system (electron and light field) exhibits photon sidebands of the electron density of states at $\pm N\hbar\omega_0$ (with integer N), which are upshifted in energy [22–24] according to

$$\hbar\omega_0 \frac{|\Delta\phi_e|}{2\pi} = \langle \mathcal{E}_{\text{kin}} \rangle, \quad (2.29)$$

i.e., upshifted by $\langle \mathcal{E}_{\text{kin}} \rangle$. Thus, the ponderomotive energy $\langle \mathcal{E}_{\text{kin}} \rangle$ for electrons is analogous to the carrier-envelope offset frequency f_ϕ for photons.

Dressed electrons

Quantum mechanically, the dynamics of an electron wavepacket can be given by time-dependent (nonrelativistic) Schrödinger equation, given by

$$i\hbar \frac{\partial}{\partial t} \psi(x, t) = \frac{1}{2m_e} (p_x + eA_x)^2 \psi(x, t) + V(x, t) \psi(x, t), \quad (2.30)$$

with the momentum operator

$$p_x = -i\hbar \frac{\partial}{\partial x}. \quad (2.31)$$

The laser electric field $\mathbf{E}(x, t)$ is related to the vector potential $\psi(x, t)$ (with $V(x, t) = -e\phi(x, t)$) via

$$\mathbf{E}(x, t) = -\frac{\partial \mathbf{A}(x, t)}{\partial t} - \frac{\partial \phi(x, t)}{\partial x} . \quad (2.32)$$

We will discuss the two gauges: (i) the radiation gauge, i.e., $\phi(x, t) = 0$, and (ii) the electric-field gauge, i.e., $A_x = 0$. Depending on the light-matter interaction of interest, one can choose either of these gauges.

(i) Radiation gauge The first possibility to introduce the laser electric field \mathbf{E} into the Schrödinger equation (2.30) is to set $V(x) = -e\phi = 0$. Assuming the laser electric field to be constant in space, we get

$$\mathbf{E} = -\frac{\partial \mathbf{A}}{\partial t} . \quad (2.33)$$

With a linearly polarized electric field $E(t) = \tilde{E}_0 \cos(\omega_0 t)$, we obtain

$$A_x(t) = -\frac{1}{\omega_0} \tilde{E}_0 \sin(\omega_0 t) . \quad (2.34)$$

This leads to the time-dependent Schrödinger equation

$$i\hbar \frac{\partial}{\partial t} \psi(x, t) = \frac{1}{2m_e} \left[-i\hbar \frac{\partial}{\partial x} - \frac{e\tilde{E}_0}{\omega_0} \sin(\omega_0 t) \right]^2 \psi(x, t) . \quad (2.35)$$

The solution of Eq. (2.35) is obtained by making the ansatz [12]

$$\psi(x, t) = e^{ik_x x} \sum_{N=-\infty}^{+\infty} a_N e^{-i(\omega_N t)} , \quad (2.36)$$

with the frequencies ω_N given by

$$\hbar\omega_N = \frac{\hbar^2 k_x^2}{2m_e} + \langle \mathcal{E}_{\text{kin}} \rangle + N\hbar\omega_0 , \quad (2.37)$$

i.e., we have a comb of equidistant frequencies, upshifted by the ponderomotive energy $\langle \mathcal{E}_{\text{kin}} \rangle$. The term $\hbar^2 k_x^2 / (2m_e)$ may be viewed as the initial kinetic energy of the electron. The ansatz (2.36) together with (2.37) can be verified by inserting it into the time-dependent Schrödinger equation (2.35). For the special case $k_x = 0$, the amplitudes of the sidebands is given as

$$a_N = J_{-N/2} \left(\frac{\langle \mathcal{E}_{\text{kin}} \rangle}{2\hbar\omega_0} \right) \quad \text{for even integer } N, \quad a_N = 0 \text{ else} \quad (2.38)$$

where J_N is the N -th-order Bessel function of the first kind. The states according to (2.36) together with (2.37) and (2.38) are called *Volkov states* [25, 26]. Figure 2.2 shows numerical examples of the Volkov states. They have discrete wave numbers k_x , which means that they are delocalized in real space. The Volkov states are

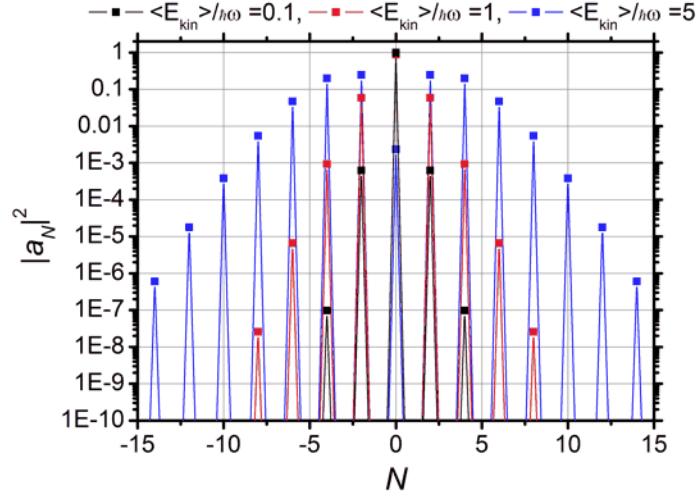


Fig. 2.2: Volkov sidebands for a ponderomotive energy of $\langle \mathcal{E}_{\text{kin}} \rangle / \hbar\omega_0 = 0.1, 1, 5$ according to (2.38).

often referred to as *dressed states* because the influence of the light field modifies the momentum distribution of electrons.

The Volkov states are an important starting point for discussing extreme nonlinear optics such as *dynamical Franz-Keldysh effect* and *multiphoton absorption*. There, a transition into a N -photon sideband of the electron can be viewed as a N -photon absorption process.

(ii) Electric-field gauge Choosing $A_x = 0$ as the second option, the laser electric field corresponds to a potential energy $V(x, t) = +xeE(t)$ of the electron. Thus we have the partial differential equation

$$i\hbar \frac{\partial}{\partial t} \psi(x, t) = -\frac{\hbar^2}{2m_e} \frac{\partial^2}{\partial x^2} \psi(x, t) + xe\tilde{E}_0 \cos(\omega_0 t) \psi(x, t). \quad (2.39)$$

This expression becomes important when we consider the static-field limit, i.e., $\omega_0 = 0$. In this case, the corresponding electron wave functions are given by Airy functions and result in *Franz-Keldysh effect*. See Sect. 2.4.3.

2.3 Ionization in strong electric fields

The Keldysh parameter

The light intensities necessary to rapidly ionize an atom are on the order of $I \approx 10^{14} - 10^{16} \text{ W/cm}^2$. In the case of a static electric field, one can simply consider quantum-mechanical tunneling through potential barriers. However, it is not clear whether the concept of electrostatic tunneling can be applied for light fields oscillating on a femtosecond timescale. Let us look at the problem semiclassically and call the time the electron spends within the barrier *the electron tunneling time* t_{tun} . The inverse of this time is *the tunneling frequency* Ω_{tun} . If the tunneling time is shorter than

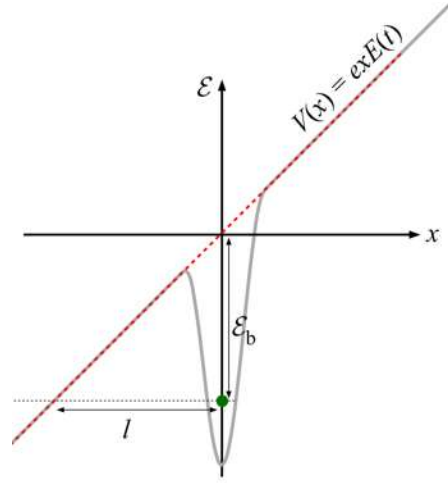


Fig. 2.3: Illustration of tunneling of an electron out of a potential well. An instantaneous electric field $E(t) > 0$ bends the potential profile. The resulting potential barrier width l and the binding energy (or ionization potential) \mathcal{E}_b are indicated.

the period of light, the laser electric field can be viewed as a static field along x that parametrically changes its instantaneous value. Let us estimate the tunneling time, which is given by the width of the barrier divided by the electron velocity in the barrier: The potential energy profile is bent by an instantaneous electric field by an amount of $xeE(t)$, and the total potential energy profile $V(x)$ becomes $V(x) = U(x) + exE(t)$, where $U(x)$ is the original Coulomb binding potential profile (Fig. 2.3). The width of the potential barrier, l , depends on the instantaneous value of the electric field $E(t)$. The potential drop over length l is identical to the electron binding energy \mathcal{E}_b . At the peak of the field, where $E(t) = \tilde{E}_0$, this leads to $le\tilde{E}_0 = \mathcal{E}_b$, equivalent to

$$l = \frac{\mathcal{E}_b}{e\tilde{E}_0}. \quad (2.40)$$

If we consider the total electron energy \mathcal{E}_e , i.e., $\mathcal{E}_e = m_e v^2/2 + V(x)$, we see that the electron velocity v is purely imaginary within the barrier, where the potential energy $V(x) > \mathcal{E}_e$. Its modulus is given by $|v(x)| = \sqrt{2(V(x) - \mathcal{E}_e)/m_e}$. Hence, the electron velocity $|v|$ within the barrier is large if the potential barrier is high. At the same time, the tunneling rate is low. At the maximum of the barrier, where $[V(x) - \mathcal{E}_e] = \mathcal{E}_b$, the electron velocity is given by $|v| = \sqrt{2\mathcal{E}_b/m_e}$. While propagating through the barrier, the electron slows down and when it has traversed the barrier, we have $V(x) = \mathcal{E}_e$ and its kinetic energy (and the velocity) is zero. Thus, the average electron velocity in the barrier is roughly the mean, i.e.,

$$\langle |v| \rangle = \frac{1}{2} \left(\sqrt{\frac{2\mathcal{E}_b}{m_e}} + 0 \right) = \sqrt{\frac{\mathcal{E}_b}{2m_e}}. \quad (2.41)$$

We obtain the tunneling time

$$t_{\text{tun}} = \frac{l}{\langle |v| \rangle} = \frac{\sqrt{2m_e \mathcal{E}_b}}{e \tilde{E}_0}. \quad (2.42)$$

To summarize, the “static-field approximation” is justified for $\Omega_{\text{tun}}/\omega_0 \gg 1$ with the peak tunneling frequency given by

$$\Omega_{\text{tun}} = \frac{e}{\sqrt{2m_e \mathcal{E}_b}} \tilde{E}_0. \quad (2.43)$$

The dimensionless ratio

$$\gamma_K = \frac{\omega_0}{\Omega_{\text{tun}}} = \frac{\omega_0 \sqrt{2m_e \mathcal{E}_b}}{e \tilde{E}_0} = \sqrt{\frac{\mathcal{E}_b}{2\langle \mathcal{E}_{\text{kin}} \rangle}} \quad (2.44)$$

is *Keldysh parameter* γ_K introduced by L. V. Keldysh [27]. For $\gamma_K \ll 1$, the picture of electrostatic tunneling can be applied. On the RHS of (2.44), we have alternatively expressed the Keldysh parameter using the ponderomotive energy $\langle \mathcal{E}_{\text{kin}} \rangle$, which can easily be verified by insertion of (2.24) into (2.44). Thus, we can equivalently say that something special is expected to happen if the peak kinetic energy $2\langle \mathcal{E}_{\text{kin}} \rangle$ becomes comparable to the electron binding energy \mathcal{E}_b .

Tunnel ionization and multiphoton ionization

Under a low-frequency strong electric field (typically, $\gamma_K < 1$), the ionization of atoms and molecules can be understood by tunneling. The ionization rate $\Gamma_{\text{ion}}(t)$ depends exponentially on the instantaneous barrier width $l(t)$ because the electron wave function is decaying exponentially. The probability of tunneling through the barrier is $\propto |\psi(l)|^2$. General behavior of tunneling ionization rate is then given by

$$\Gamma_{\text{ion}}(t) \propto \exp \left[-\frac{\sqrt{2m_e \mathcal{E}_b}}{\hbar} l(t) \right] = \exp \left[-\frac{\sqrt{2m_e}}{\hbar e} \frac{\mathcal{E}_b^{\frac{3}{2}}}{|E(t)|} \right]. \quad (2.45)$$

Because of this exponential dependence of the ionization rate on the electric field strength, ionization occurs predominantly around the peak electric field (Fig. 2.4). This non-perturbative behavior is one of the fundamental processes in extreme nonlinear optics, and is used to produce attosecond electron wavepackets. When $\gamma_K > 1$ (i.e., high frequency or weak electric fields), field-induced ionization is dominated by multiphoton absorption (Fig. 2.5). The Gamma parameter is an appropriate parameter to classify the field-induced ionization of isolated quantum systems.

2.3.1 High harmonic generation from atoms and molecules

High harmonic generation from atoms was discovered in 1987 [28–30], although the underlying mechanism was not revealed at that time. Figure 2.6 illustrates a typical spectral structure of high harmonics from atoms. Typically, the intensity of the harmonic orders decays rapidly over several orders of magnitude up to about

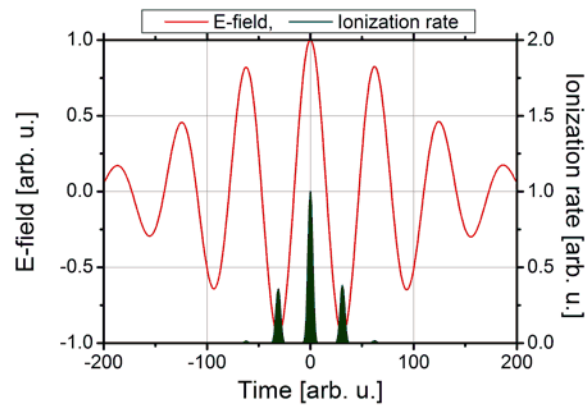


Fig. 2.4: Illustration of the instantaneous ionization rate (green curve) versus the instantaneous laser electric field (red curve) in the static-field approximation according to Eq. (2.45).

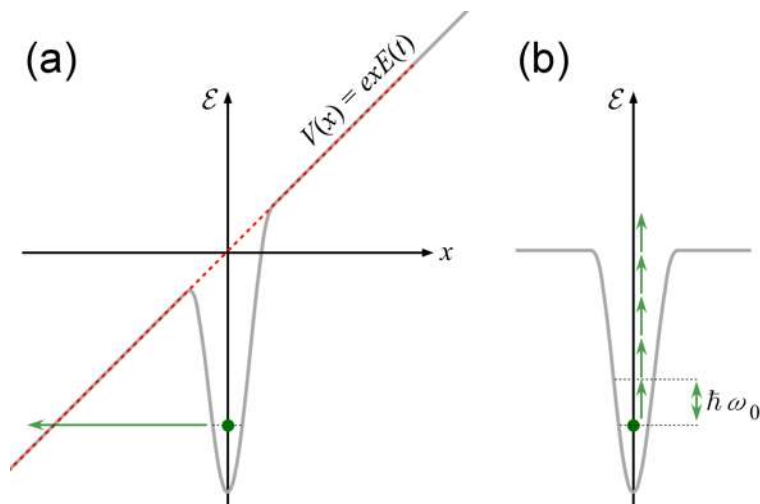


Fig. 2.5: Illustration of ionization of atoms via (a) electrostatic tunneling at large laser fields ($\gamma_K \ll 1$) and (b) multiphoton absorption at weak laser electric fields ($\gamma_K \gg 1$).

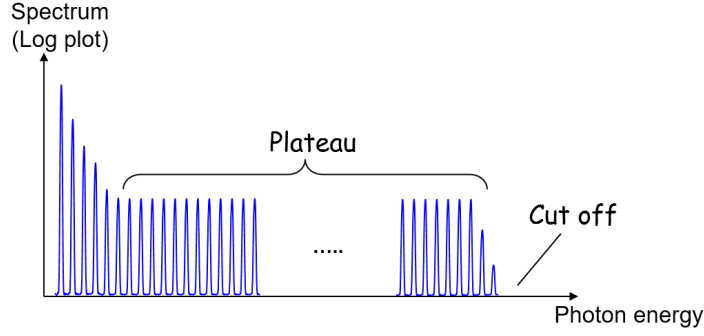


Fig. 2.6: Schematic illustration of a typical high harmonic spectrum from atoms.

order ten or twenty. This is followed by a *plateau region* of more or less constant harmonic orders and a rapid fall for orders above the *cutoff order* N_{cutoff} . The latter depends on the laser intensity and the atom or ion under consideration.

In 1993, a simple semiclassical model was proposed that explained main features of high harmonics from atoms, such as the cut-off scaling law, the existence of *short* and *long* trajectories, and *atto-chirp* (For details, see Ref [31]).

In this semiclassical model, which is called *three-step model*, the atom is ionized instantaneously at the crest of the electric field via tunneling (step 1). In the case of linearly polarized laser field, the freed electron initially have a zero kinetic energy. The electron is then accelerated by the field (step 2). When the polarity of the field is reversed, the electron is accelerated towards the opposite direction and returns to the ionized position with a finite kinetic energy. The recombination to the ground state leads to the emission of photon (step 3). The emitted photon energy $\hbar\omega(t_r) = \mathcal{E}_e(t)$ depends on the recombination time t_r . By considering the classical electron trajectories, the maximum kinetic energy of the electron at the time of recombination is equal to $3.17\langle\mathcal{E}_{\text{kin}}\rangle$. Thus the order of high harmonic cutoff is given by

$$N_{\text{cutoff}} = \frac{\mathcal{E}_b + 3.17\langle\mathcal{E}_{\text{kin}}\rangle}{\hbar\omega_0}. \quad (2.46)$$

Note that the cutoff harmonic scales linearly with the laser intensity $I(\propto \langle\mathcal{E}_{\text{kin}}\rangle)$. This is in contrast to the corresponding expression for two-level systems, (2.20), where N_{cutoff} is proportional to $\sqrt{I} \propto \Omega_R$ in the "static-field limit". In addition, the cutoff-order has quadratic dependence to the reciprocal of the laser frequency $\langle\mathcal{E}_{\text{kin}}\rangle \propto 1/\omega_0^2$. High harmonic generation from atoms is the very foundation of attosecond science [31].

As we just have seen, high harmonics are generated as a result of interaction of the freed electrons and their parent ions, and therefore, the generated high harmonics contains the information of the electron-ion interaction. The spectroscopic method which uses the process of HHG as a probe is called *high harmonic spectroscopy* [32].

In a quantum-mechanical point of view, an ionized electron wavepacket $\Psi_c(t)$ will coherently probe what was left of itself in the ground state $\Psi_g(t)$, resulting

the time-dependent dipole, $\mathbf{d}(t) = \langle \psi_g(t) | -e\mathbf{r} | \psi_c(t) \rangle + \text{c.c.}$, which emits the harmonics. Based on this picture, tomographic imaging of molecular orbitals has been demonstrated [33–36].

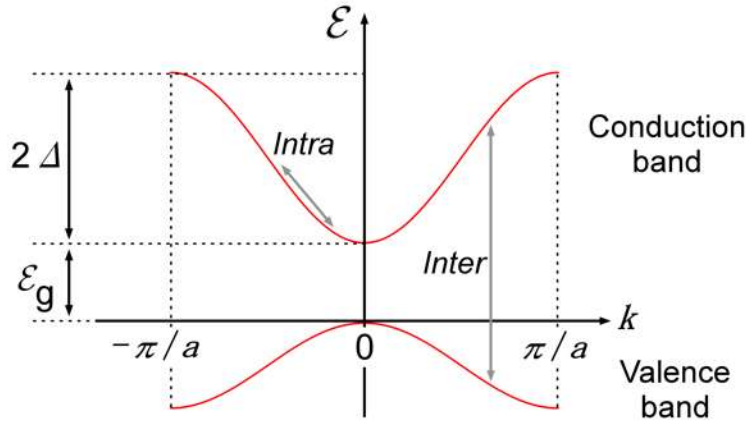


Fig. 2.7: Schematic illustration of the valence and the conduction band of a direct gap semiconductor in the first Brillouin zone. \mathcal{E}_g , 2Δ , and a are the bandgap energy, the width of the band, and the lattice constant, respectively.

2.4 Strong-field-driven processes in solids

2.4.1 Crystal electrons

In crystalline solids, atoms are arranged in the form of a periodic lattice with lattice constant a . The overlap of the electronic wavefunctions lifts the degeneracy of the discrete atomic energy levels and leads to energy bands. The wavefunctions become Bloch waves, which have a particular dispersion relation. Figure 2.7 schematically shows this dispersion relation for a direct-gap semiconductor with bandgap energy \mathcal{E}_g . Light can couple to the crystal electrons in two ways: via *interband* transitions and via *intra*band transitions.

Interband transitions

Light can promote an electron from an occupied state in the valence band into an empty state in the conduction band - provided the dipole moment is nonzero. The photon wavelength is much larger than typical lattice constants. Consequently, the photon wavevector is a thousand times smaller than the electron wavevector at the edge of the first Brillouin zone, π/a , and such a transition looks very nearly vertical in the band structure. Thus, a state with wavevector k in the valence band is coupled to a state with the same wavevector k in the conduction band. Looking at these two states with transition frequency $\Omega(k)$ only, this problem is similar to what we have seen about two-level systems in Sect. 2.1. On this level of description, extreme nonlinear optical responses can be understood by considering an ensemble of uncoupled two-level systems. Although there are deviations from this simple picture, the important energy scale of interband transitions is the *Rabi energy* $\hbar\Omega_R$. If it becomes comparable with the transition energy $\hbar\Omega$, the regime of extreme nonlinear optics starts, as shown in the discussion of the two-level system.

In order to actually evaluate the peak Rabi energy $\hbar\Omega_R = d_{cv}E_0$, one needs to know the dipole matrix element for a transition from the valence (v) to the conduction (c) band at wavevector \mathbf{k} . Within $\mathbf{k} \cdot \mathbf{p}$ perturbation theory [21], the dipole matrix element d_{cv} is approximately wavevector independent and can be estimated on the basis of known material parameters by the following "rule of thumb"

$$|d_{cv}|^2 = \frac{\hbar^2 e^2}{2\mathcal{E}_g} \left(\frac{1}{m_e} - \frac{1}{m_0} \right), \quad (2.47)$$

with the effective electron mass m_e and the free electron mass, m_0 .

Intraband transitions

The light field can also influence the states in the conduction (valence) band. Classically, this corresponds to the acceleration of an electron in the band. Near the center of the Brillouin zone, the bands can often be approximated by parabolas and the resulting physics is that of Volkov states (Sect. 2.2.1). Extreme nonlinear optics starts if the Volkov sidebands acquire appreciable strength. This happens if the *ponderomotive energy* $\langle \mathcal{E}_{kin} \rangle$ becomes comparable to the carrier photon energy $\hbar\omega_0$. The bands develop a series of sidebands, separated by $\hbar\omega_0$. For a given laser intensity, the electron ponderomotive energy is usually much larger than the hole ponderomotive energy, because the electron effective mass is typically smaller than the hole effective mass by a factor of order ten, which makes a very large difference. We anticipate that the optical spectrum also develops sidebands separated by $\hbar\omega_0$, leading to oscillatory features in the optical spectrum. The low-energy sidebands lie in the gap of the semiconductor and lead to induced absorption below the gap. This altogether constitutes the *dynamical Franz-Keldysh effect* (see Sect. 2.4.3).

Bloch energy For a given intensity of light I , the ponderomotive energy of electrons in semiconductors according to (2.24) is usually much larger than for vacuum electrons, because typical effective electron masses are about an order of magnitude smaller than the free electron mass m_0 . For crystal electrons, however, the concept of the ponderomotive energy is only valid within the effective-mass approximation, which fails for large values of $\langle \mathcal{E}_{kin} \rangle$, often already above several 0.1 eV. This limits the importance of the ponderomotive energy for optical excitation of semiconductors under extreme conditions.

For larger laser intensities, therefore, an alternative quantity which reflects the kinetic energy of the electron without employing the effective-mass approximation is required. Within the acceleration theorem, the crystal-electron momentum $\hbar k_x$, obeys Newton's second law according to $\hbar \dot{k}_x = F$. Inserting the laser electric field $E(t)$ into the force $F = -eE(t)$, we can easily rewrite the acceleration theorem according to

$$a \frac{\partial}{\partial t} k_x(t) = -\Omega_B(t) \quad (2.48)$$

where we have introduced the instantaneous *Bloch frequency* $\Omega_B(t)$ with

$$\hbar\Omega_B(t) = aeE(t) . \quad (2.49)$$

At any given time t , the Bloch energy $\hbar\Omega_B(t)$ corresponds to the potential drop over one unit cell of the crystal lattice with lattice constant a . Note that the Bloch frequency $\Omega_B(t)$ oscillates in time and periodically changes sign.

In order to get intuitive understanding of the meaning of the Bloch frequency, we consider a static electric field $E(t) = E_0$. In this case, we can easily solve (2.48) together with the initial condition $k_x(0) = 0$ and obtain

$$k_x(t) = -\frac{\Omega_B t}{a} . \quad (2.50)$$

At time $t = \pi/\Omega_B$, the electron hits the end of the first Brillouin zone, i.e., we have $k_x = -\pi/a$. This leads to Bragg reflection of the crystal electron to the other end of the first Brillouin zone with $k_x = +\pi/a$. After another time span of π/Ω_B , the electron is back to its initial state, $k_x = 0$, and one oscillation period $2\pi/\Omega_B$ is completed. This oscillation in wave-number space leads to an oscillation of the electron along the x -direction in real space, which is known as a *Bloch oscillation*. Note that its frequency, the Bloch frequency, does not depend on the particular dispersion relation (the band structure) of the crystal electron.

2.4.2 Bloch oscillation and high harmonic generation in solids

Let us discuss the spectrum of light radiated from a crystal-electron wavepacket within a one-dimensional tight-binding band with energy dispersion

$$E_e(k_x) = \hbar\omega_e(k_x) = -\Delta \cos(k_x a) \quad (2.51)$$

semiclassically. 2Δ is the width of the band. We consider continuous-wave excitation, i.e., $E(t) = E_0 \cos(\omega_0 t)$, which is equivalent to

$$\Omega_B(t) = \Omega_B \cos(\omega_0 t) \quad (2.52)$$

with the *peak Bloch frequency*

$$\Omega_B = aeE_0/\hbar . \quad (2.53)$$

The ratio Ω_B/ω_0 is called the *dynamical localization parameter*. Furthermore, we neglect any type of damping and use the single-particle approximation. The intensity spectrum $I_{\text{rad}}(\omega)$ radiated by this wavepacket via its intraband motion is given by $I_{\text{rad}}(\omega) \propto |\omega v_g(\omega)|^2$. The electron group velocity v_g at wave number k_x results from

$$v_g = \frac{d\omega_e}{dk_x} , \quad (2.54)$$

then

$$v_g(t) = \frac{a\Delta}{\hbar} \sin[k_x(t) a] . \quad (2.55)$$

With the initial condition $k_x(0) = 0$, we obtain the electron wave number $k_x(t)$ from (2.48)

$$k_x(t) = -\frac{\Omega_B}{a\omega_0} \sin(\omega_0 t) . \quad (2.56)$$

Inserting (2.56) into (2.55) leads to

$$\begin{aligned} v_g(t) &= -\frac{a\Delta}{\hbar} \sin \left[\frac{\Omega_B}{\omega_0} \sin(\omega_0 t) \right] \\ &= -\frac{a\Delta}{\hbar} 2 \sum_{M=0}^{\infty} J_{2M+1} \left(\frac{\Omega_B}{\omega_0} \right) \sin [(2M+1)\omega_0 t] . \end{aligned} \quad (2.57)$$

Here J_N is the N -th-order Bessel function of the first kind. From (2.57), the peak heights of the odd harmonics in the radiated intensity spectrum results in

$$I_{\text{rad}}(N\omega_0) \propto (N\omega_0)^2 J_N^2 \left(\frac{\Omega_B}{\omega_0} \right) . \quad (2.58)$$

The radiated intensity spectrum is illustrated in Fig. 2.8. For $\Omega_B/\omega_0 \ll 1$, the first sine in (2.57) can be approximated by its argument and the group velocity becomes a harmonic oscillation at the carrier frequency ω_0 , i.e., $v_g \propto -\sin(\omega_0 t)$. For $\Omega_B/\omega_0 \approx 1$, the behavior deviates from this and odd harmonics of ω_0 appear in the Fourier domain via the $\sin[\dots \sin(\dots t)]$ behavior that stems from the nonparabolicity of the band. For $\Omega_B/\omega_0 \gg 1$ and at around times t with $\omega_0 t = 0, \pi, \dots$, the second sine can be approximated by its argument, hence the crystal electron harmonically oscillates with the peak Bloch frequency, i.e., $v_g \propto \mp \sin(\Omega_B t)$. This represents the static-field limit, which we have already discussed above. As the peak Bloch frequency is the largest frequency in the system within this limit, it determines the cutoff harmonic order, which is approximately given by

$$N_{\text{cutoff}} = \frac{\Omega_B}{\omega_0} . \quad (2.59)$$

This cutoff is closely similar to that of the two-level system in the high-field limit, Eq. (2.20).

Note that, here we have neglected any type of damping (scattering), which prevents the Bloch oscillations in practice. Especially when the electron is high in the band, where it has many channels to relax, ultrafast scattering in the order of few femtoseconds may occur. Furthermore, we have only accounted for the intraband contribution of the optical polarization in this section. The intraband driving, however, can also modify the interband optical polarization in which case one generally expects a complicated mixture of Rabi oscillations and Bloch oscillations (see Chap. 3.2).

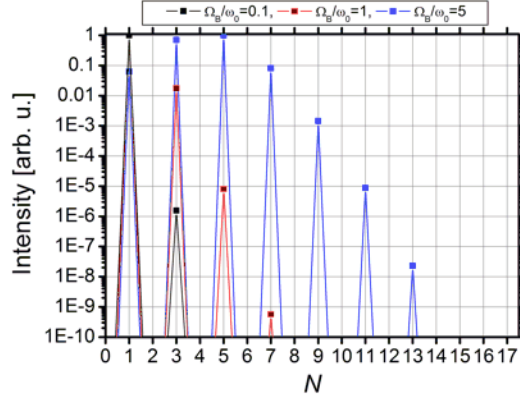


Fig. 2.8: Radiated intensity spectrum I_{rad} for $\Omega_B/\omega_0 = 0.1, 1, 5$ according to (2.58).

2.4.3 Franz-Keldysh effect (FKE)

Recently the light induced absorption changes which are considered due to the Franz-Keldysh effect (FKE) have been observed (see Sect. 3.3), thanks to the development of long-wavelength laser technology. Here I briefly introduce the static FKE and the dynamical FKE.

Static-field approximation

The main theoretical prediction by Franz and Keldysh in 1958 [37, 38] was that applying a static electric field on the order of 10^5 to 10^6 V/cm to a direct-gap semiconductor, results in an exponential absorption tail below the fundamental bandgap. Later, additional spectral features above the bandgap were discovered. All these features can be understood in terms of photon-assisted tunneling of electrons from the valence to the conduction band: In the presence of the static electric field \tilde{E}_0 along the x -direction, the stationary one-dimensional Schrödinger equation becomes

$$-\frac{\hbar^2}{2m_e} \frac{\partial^2}{\partial x^2} \psi(x) + xe\tilde{E}_0 \psi(x) = \mathcal{E}_e \psi(x), \quad (2.60)$$

with the electron energy \mathcal{E}_e . Substituting

$$X = x \left(\frac{2m_e e \tilde{E}_0}{\hbar^2} \right)^{\frac{1}{3}} - \frac{2m_e \mathcal{E}_e}{\hbar^2} \left(\frac{2m_e e \tilde{E}_0}{\hbar^2} \right)^{-\frac{2}{3}} \quad (2.61)$$

leads to the standard nonlinear differential equation

$$\frac{d^2 \psi}{dX^2}(X) = X \psi(X). \quad (2.62)$$

Its solution is $\psi(X) = \text{Ai}(X)$ with the Airy function $\text{Ai}(X)$, which decays exponentially for $X \rightarrow +\infty$ and that oscillates with a wavelength proportional to $1/\sqrt{X}$ for negative X . The important aspect is that this wave function has a tail that extends into the gap of the semiconductor. This is illustrated in Fig. 2.9. For an electron

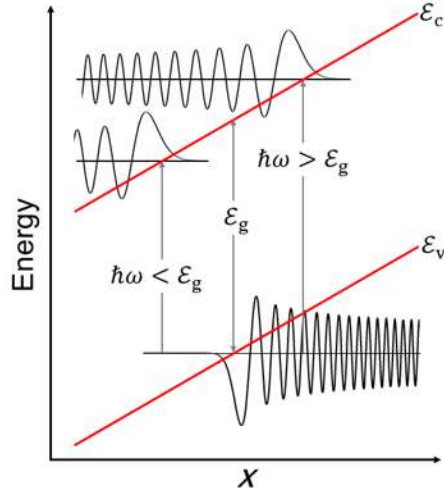


Fig. 2.9: Schematic drawing of conduction band edge E_c and valence band edge E_v in the presence of a strong electric field. Typical Franz-Keldysh eigenstates and possible optical transitions are also shown.

wave function and a hole wave function separated in energy by less than the gap energy \mathcal{E}_g , the probability to find an electron and a hole at the same position has become finite. The larger the applied electric field, the larger the overlap. This allows for optical transitions at photon energies $\hbar\omega < \mathcal{E}_g$ below the gap energy \mathcal{E}_g . The resulting shape of the absorption spectrum $\alpha(\hbar\omega)$ within the effective-mass approximation is given by [20, 21]

$$\alpha(\hbar\omega) \propto \omega |\tilde{E}_0|^{\frac{1}{3}} \left\{ \tilde{\omega} [\text{Ai}(-\tilde{\omega})]^2 + [\text{Ai}'(-\tilde{\omega})]^2 \right\}, \quad (2.63)$$

with the derivative of the Airy function $\text{Ai}'(X)$ and the normalized spectrometer frequency

$$\tilde{\omega} = \frac{\hbar\omega - \mathcal{E}_g}{\mathcal{E}_b} \left(\frac{\mathcal{E}_b}{er_B |\tilde{E}_0|} \right)^{\frac{2}{3}}. \quad (2.64)$$

Here, \mathcal{E}_b is the exciton binding energy and r_B the exciton Bohr radius. We have taken advantage of the fact that, in a semiconductor with inversion symmetry, the sign of \tilde{E}_0 does not matter. The absorption spectrum is depicted in Fig. 2.10. It consists of an exponential tail for frequencies ω below the bandgap (the Franz-Keldysh effect) and an oscillatory behavior above the gap. The visibility of the oscillations decreases with increasing frequency. This has to be compared with the zero-field absorption spectrum

$$\alpha(\hbar\omega) \propto \Theta(\hbar\omega - \mathcal{E}_g) \sqrt{\hbar\omega - \mathcal{E}_g} \quad (2.65)$$

of a three-dimensional semiconductor within the effective-mass approximation (gray curve in Fig. 2.10a).

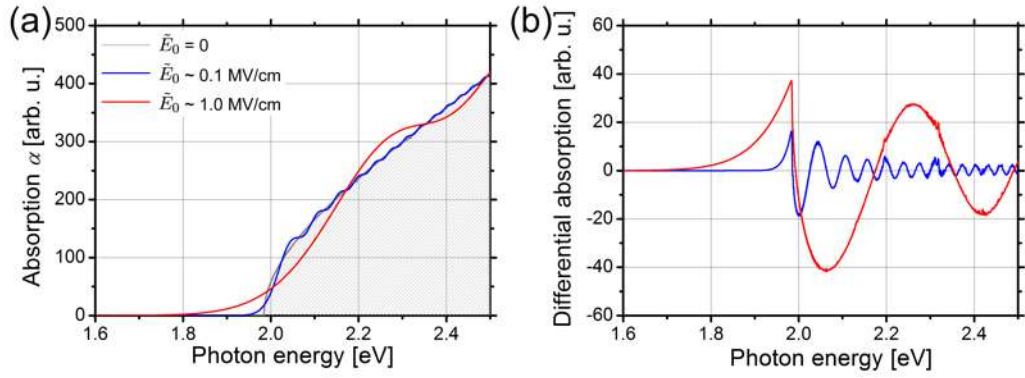


Fig. 2.10: Schematic of absorption spectra of a three-dimensional semiconductor subject to static electric fields according to (2.63).

Dynamical Franz-Keldysh effect

In Sect. 2.2.1, we have seen that Volkov states are solutions of the time-dependent Schrödinger equation within the effective-mass approximation for a harmonically varying electric field [39]. For sufficiently large ω_0 , i.e., when the static-field approximation is not valid, Volkov sidebands may show up in the absorption spectrum by a series of equidistant absorption onsets [22, 23]. This phenomena is called *dynamical Franz-Keldysh effect*. The "high" and "low" frequency can be quantified in terms of γ_K [40]. The static FKE corresponds to $\gamma_K \ll 1$; multiphoton effects dominantly occur for $\gamma_K \gg 1$; and the case of $\gamma_K \sim 1$ is a dynamical FKE regime. To observe dynamical FKE, the ponderomotive energy $\langle \mathcal{E}_{\text{kin}} \rangle$ must not significantly exceed values of order 0.1 eV, otherwise the effective-mass approximation for the electrons is no longer valid. Practically, when both $\hbar\omega_0$ and $\langle \mathcal{E}_{\text{kin}} \rangle$ are on the order of a few tenths of an electron Volt, the conditions for the observation of dynamical FKE can be fulfilled for typical semiconductors. Experimental results of previous works are discussed in Chap. 3.3.

Experiments of strong electric field processes in solids

3.1 Sub-cycle spectroscopy

3.1.1 Concept of sub-cycle spectroscopy

Time-resolved spectroscopies typically rely on a pump-probe approach. A sufficiently short pump pulse initiates a process, while a short probe pulse measures changes in the system response as a function of the pump-probe delay (Fig. 3.1(a)). In most cases, time resolution in such a (conventional) pump-probe measurement is limited by the duration of the pump and probe pulses, and the conventional time-resolved spectroscopy is only able to detect the phenomena in the regime of linear and perturbative nonlinear optics which depend on the pulse envelopes, i.e., unable to detect extremely-fast strong-field processes which occur within one-laser cycle, because the phase of the pump fields changes shot-by-shot and the field-dependence is averaged out.

The crucial step to time-resolved spectroscopy of extremely nonlinear light-matter interactions within the sub-cycle time scale (*sub-cycle spectroscopy*) has been heralded by the recent progress of the ultrafast laser technologies, especially the CEP-locking technology. Fig. 3.1 shows the difference between conventional time-resolved spectroscopies and sub-cycle spectroscopies. This revolutionary change occurred nearly at the same time in the field of THz science and Attosecond science. In this section, we briefly review the achievements of sub-cycle spectroscopy in THz science and Attosecond science, focusing our interest to strong electric-field processes in solids.

3.1.2 Sub-cycle spectroscopy in THz science

Recent progress of the generation of intense THz pulses has opened sub-cycle spectroscopy with all-optical methods. Thanks to the tilted-pulse-front method [41], THz pulses beyond $1 \mu\text{J}$, whereby peak electric fields above 1 MV/cm have been reached, have become available [42, 43]. Figure 3.2 shows a typical experimental setup for strong-field THz-spectroscopy. Waveform sampling of THz transients can be easily done by electro-optic sampling method [44] or terahertz air-biased-coherent-detection (THz-ABCD) method [45, 46] with Ti:sapphire pulses which is also used to generate THz pulses and whose pulse duration is intrinsically much shorter than the oscillation period of THz transients. For the case of sub-cycle spectroscopy, the Ti:sapphire beam was split into three parts and, the sample is additionally illuminated by optical probe pulses.

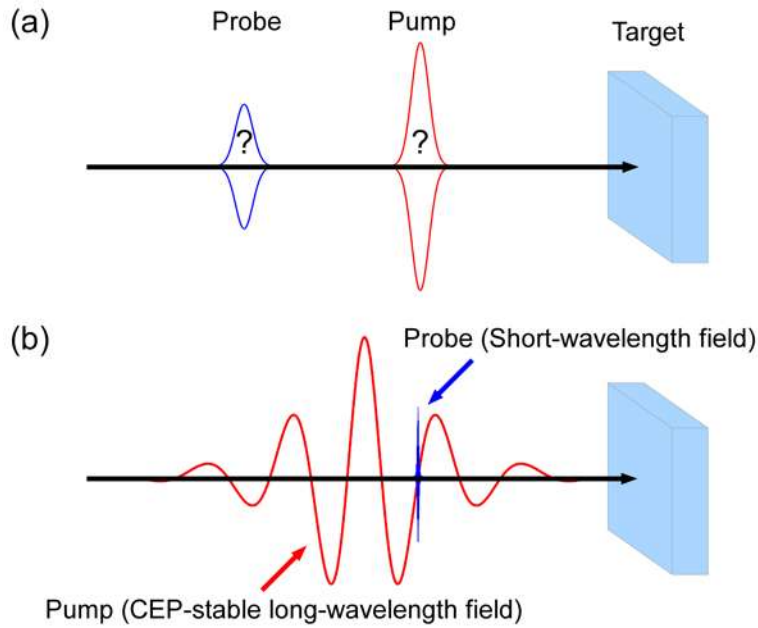


Fig. 3.1: Schematic illustration of (a) *conventional* pump-probe spectroscopy, and (b) *sub-cycle* pump-probe spectroscopy.

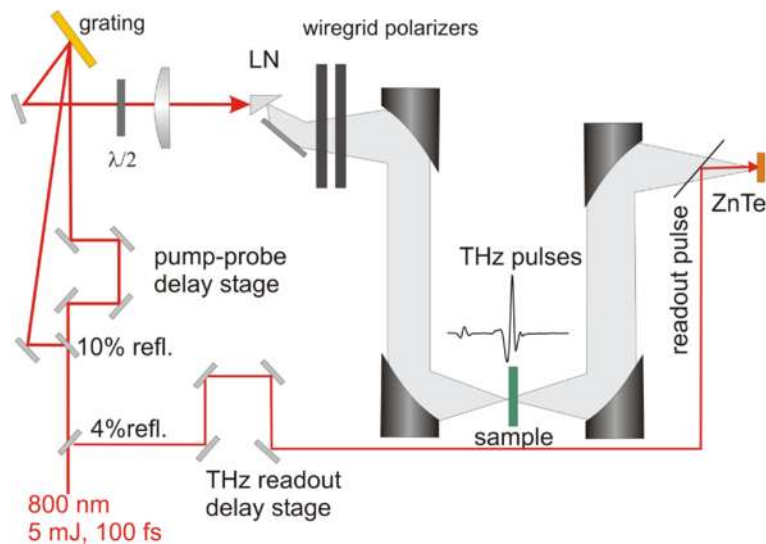


Fig. 3.2: Typical setup for strong-field THz-spectroscopy [47]. Collinear THz pulses are generated by tilted pulse front excitation in LiNbO₃ and detected electro-optically. For the case of sub-cycle spectroscopy, the sample is additionally illuminated by optical probe pulses.

The sub-cycle spectroscopy in THz science is targeting solids from the earliest stage due to the low energy scale of the THz pulses (photon energy and field strength). When intense THz fields interact with solids, a variety of non-equilibrium scenarios may result [48, 49]. Most studies have concentrated on the effects of THz excitation after the coherence between the external driving field and the induced polarization has decayed. On the other hand, first examples of coherent THz nonlinearities have been demonstrated with semiconductors [50–53] and rotational states of gas molecules [54–56]. These studies emphasized the importance of dynamics occurring on time scales shorter than the dephasing time of the system. As increasing number of interesting results are obtained from the strong THz experiments, much stronger THz pulses were required for further studies of the nonlinear light-matter interaction in the limit of extremely non-perturbative optics. Such a demand leads to the development of CEP-stable intense MIR sources.

3.1.3 Sub-cycle spectroscopy in attosecond science

Sub-cycle spectroscopy in attosecond science is developed primarily for the gas phase experiments in the past decade thanks to the availability of attosecond pulses. This approach uses a pump–probe pair consisting of an attosecond extreme ultraviolet (XUV) pulse and an CEP-stabilized near-infrared (NIR) pulse. In this case, the envelope of the XUV pulse is locked to the oscillations of the IR field. The IR pulse can be long, e.g. tens of femtoseconds, without limiting the time resolution. The latter is determined by the accuracy with which the envelope of the XUV pulse can be locked to the instantaneous oscillations of the IR field. The technique called *attosecond streaking* [57–59] is widely adopted in attosecond science.

Attosecond sub-cycle spectroscopy of solids

Attosecond metrology has been applied to condensed matters to trace electron dynamics on attosecond time scales. In this section, I will show several pioneering attosecond experiments with solids.

In 2013, Schultze *et al.* demonstrated the observation of an insulator-to-conductor transition in fused silica [60]. Figure 3.3(b) shows the measured modulation of the absorbance at 109 eV. The sample transmission exhibits large oscillations at a frequency of $2\omega_0$ (where ω_0 is the NIR frequency) perfectly synchronized with the laser field. This measurement clearly demonstrated the complete and ultrafast reversibility of the field-induced changes of the optical properties of the dielectric sample up to the critical field strength.

Also in 2013, Schiffrin *et al.* [61] demonstrated that the AC conductivity of fused silica can be increased by more than 18 orders of magnitude within 1 fs, by using few-optical-cycle NIR pulses, with stable CEP and electric field amplitude approaching the critical value given by the following expression:

$$E_{\text{cr}} = \frac{\mathcal{E}_{\text{g}}}{ea} \approx 2 \text{ V/\AA} \quad (3.1)$$

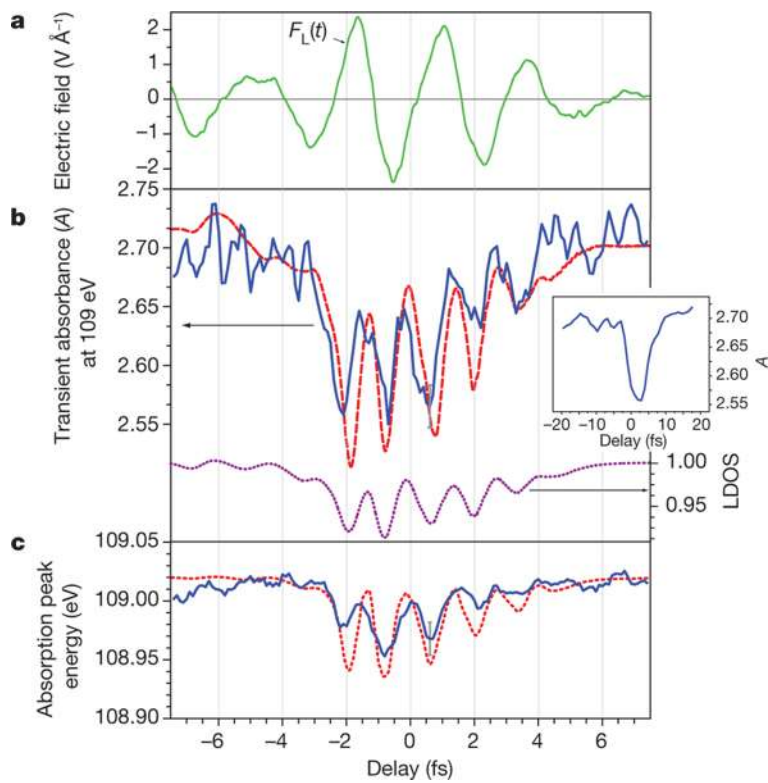


Fig. 3.3: Attosecond transient absorption of SiO_2 [60]. (a) Applied electric field; (b) Experimentally observed transient change of the absorbance (blue curve), the result of the TDDFT calculation (red and violet curve); (c) Experimentally observed absorption peak shift (blue curve) and the calculation result (red curve).

where \mathcal{E}_g is the energy gap of the dielectric material ($\mathcal{E}_g \approx 9$ eV for fused silica); e is the electron charge and a is the lattice period ($a \approx 5$ Å). If the above condition is satisfied, the NIR driving pulse is able to inject carriers from the valence to the conduction band of fused silica. The use of few-cycle pulses is essential to prevent damage of the dielectric exposed to electric fields of a few volts per angstrom [62].

3.2 High harmonic generation in crystalline solids

We have discussed high harmonic generation from a two-level system in Sect. 2.1, and from Bloch oscillation in Sect. 2.4.2. When the Rabi energy and the Bloch energy of the system become comparable to the carrier photon energy, the high harmonic generation from the interband and intraband transition are expected to occur. Although it is not clear at this stage which process is dominant in HHG in solids, we will explain the HHG in solids as a result of Bloch oscillation.

Bloch oscillation was first experimentally observed in semiconductor superlattices [63]. Immediately after that, it was also found in a variety of other artificial systems [64]. However, no clear experimental evidence for Bloch oscillations had been reported for bulk solids, and it was believed that the Bloch oscillations in bulk solids was extremely difficult until quite recently. The difficulty to observe Bloch oscillation in a bulk solid is mainly due to crystal damage by strong electric fields and scattering processes (electron-electron, electron-phonon, impurity scattering etc.). For superlattices, the condition for Bloch oscillation is drastically relaxed due to their large lattice constant a .

If we could avoid the damage issues, the conditions for the high harmonic generation from the interband and intraband contributions are quite easily fulfilled with typical Ti:sapphire CPAs, which can achieve an intensity on the order of 100 TW/cm² at a wavelength of 0.8 μ m. Figure 3.4 shows the strong field conditions, i.e., $\Omega_R/\omega_0 = 1$, $\Omega_B/\omega_0 = 1$ and $\Omega_{\text{tun}}/\omega_0 = 1$, with the parameter set of a ZnO crystal ($m_e = 0.24 \times m_0$, $a = 5.21 \text{ \AA}$, $\mathcal{E}_g = 3.3 \text{ eV}$, $d_{\text{cv}} = 0.19e \text{ nm}$ calculated from Eq. (2.47)), where

$$\Omega_R = \frac{d}{\hbar} E(t) , \quad (3.2)$$

$$\Omega_B = \frac{ea}{\hbar} E(t) , \quad (3.3)$$

$$\Omega_{\text{tun}} = \frac{e}{\sqrt{2m_e}\mathcal{E}_b} \tilde{E}_0 . \quad (3.4)$$

From the figure, we can expect the strong-field processes may appear in ZnO above 10 MV/cm ($\sim 100 \text{ GW/cm}^2$) at 0.8 μ m. Of course, in realistic situation, there would be little hope to observe such strong-field phenomena because the crystal will be damaged under such intense irradiation.

The key question is how we apply a strong electric field without damaging a crystal. Recent dramatic progress in the generation of intense MIR pulses has realized Bloch oscillation and HHG in bulk solids because ultrashort MIR pulses can achieve appropriate field strength ($\sim 100 \text{ MV/cm}$ at a frequency of 30THz (9 μ m) [65]) and have sufficiently low photon energy (few tenths of eV) to avoid optical damage. Hence, strong MIR pulses seem to be the ideal tool to study strong-field phenomena in solids.

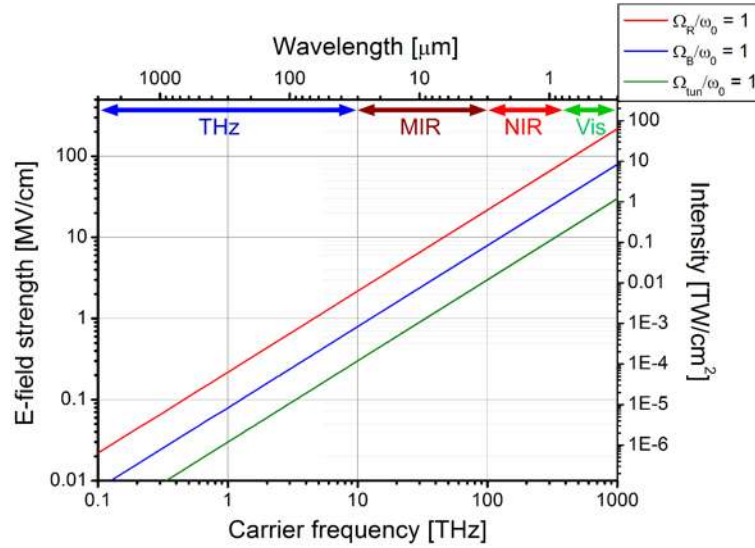


Fig. 3.4: Strong-field conditions for ZnO.

On the basis of the pioneering work [66], where harmonics up to seventh from ZnS were observed, the study of HHG from solids has become quite activated in 2011, when Ghimire et al. [67] observed HHG from solids up to 25th harmonic order extending to > 9.5 eV photon energy (see Fig. 3.5). 9-cycle-long pulses from a MIR OPA (~ 100 -fs, 3.25 - μm (0.38 eV) pulses with up to 2.63 μJ energy) were focused into a 500 - μm -thin ZnO crystal, where focused field strengths up to 60 MV/cm were achieved. Three observations made in [67] are particularly important:

1. In contrast to HHG from gases, the cutoff scales linearly with electric field strength (see Fig. 3.5(b)), as expected from Eq. (2.59),
2. The observation of HHG extending more than 6 eV above the ZnO bandgap ($\mathcal{E}_g \sim 3.3$ eV) suggests that these harmonics are generated within a few tens of nm near the output surface of the ZnO crystal. This is also valid in terms of phase matching.
3. HHG up to the 25th order was observed for experimental conditions corresponding to only $\Omega_B/\omega_0 \sim 5$. The generation of high harmonics up to 25th-order can not be expected from the simplified model of Bloch oscillation (see Fig. 2.8). This result suggests the importance of the interaction between interband and intraband dynamics. Indeed, Golde *et al.* demonstrated that interband and intraband dynamics are nontrivially coupled, within the framework of two-band semiconductor Bloch equations [68]. Their complex interplay leads to a strong enhancement of HHG towards much higher frequencies.

In 2014, HHG from 220 - μm -thick bulk GaSe crystals was investigated with CEP-stabilized MIR pulses at a wavelength of 9 μm generated by DFG [69, 70]. The observed spectrum is shown in Fig. 3.6. The authors explained that the source

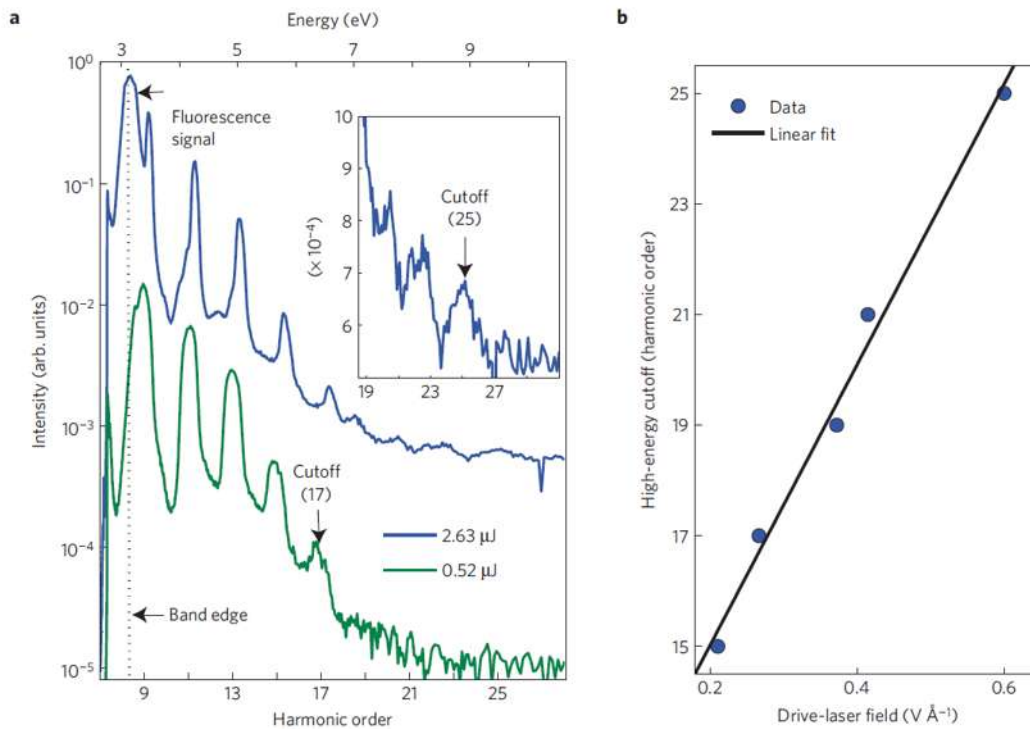


Fig. 3.5: MIR-driven HHG from bulk ZnO [67]. (a) Measured HHG spectra from 500- μm -thin ZnO crystal (optical axis perpendicular to surface) driven by 3.25- μm OPA pulses. The indicated pulse energies 0.52 μJ and 2.63 μJ correspond to (vacuum) electric field strength of 27 MV/cm and 60 MV/cm, respectively. The inset shows a zoom into the cutoff region on a linear scale. (b) Linear scaling of the HHG cutoff with laser electric field strength.

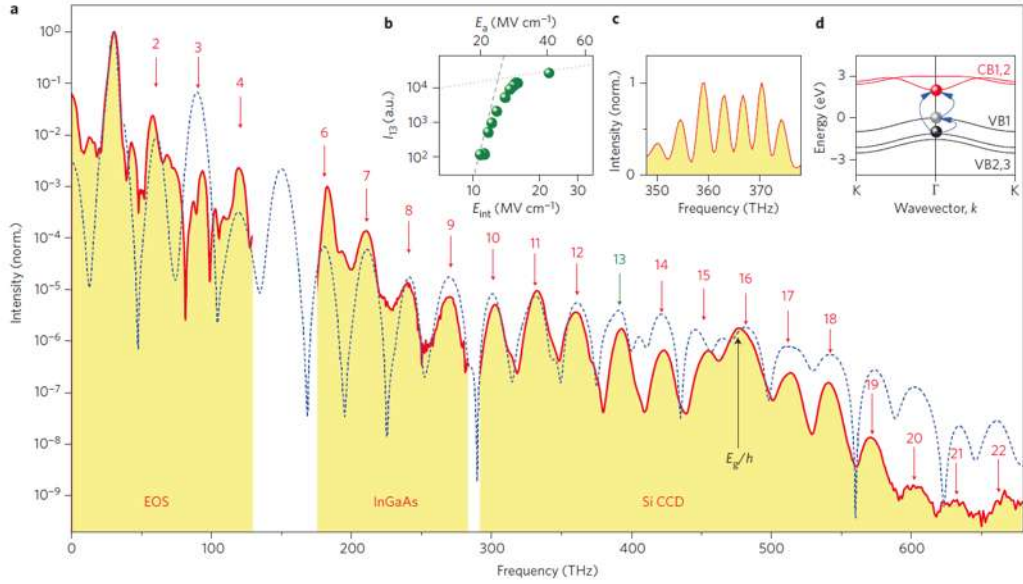


Fig. 3.6: MIR-driven HHG from bulk GaSe [69]: The blue dashed curve shows the computed HHG resulting from a 30 THz ($9 \mu\text{m}$) pump field by using the five-band model shown in the inset. The shaded area shows the corresponding measurement. The observed HHG covers more than 22 harmonic orders, reaching into the visible spectral range (above the indicated bandgap).

of odd and even order harmonics can be attributed to a nonperturbative two-path quantum interference effect in GaSe. As can be seen from the time-frequency analysis data shown in Fig. 3.7 experimentally achieved by a sum-frequency upconversion technique, due to this quantum interference, the emission bursts occur at the times of positive electric field extrema only. Importantly, attochirp was not observed in the experiment. This fact may indicate that the three-step model for gas HHG is not valid for the solid case.

Although various solid HHG has been reported so far (Table 3.1), the mechanism and underlying physics are still not well understood. Therefore, new experimental schemes to extract the information of electron dynamics in solids, as well as clear theoretical frameworks, are highly demanded [71–76].

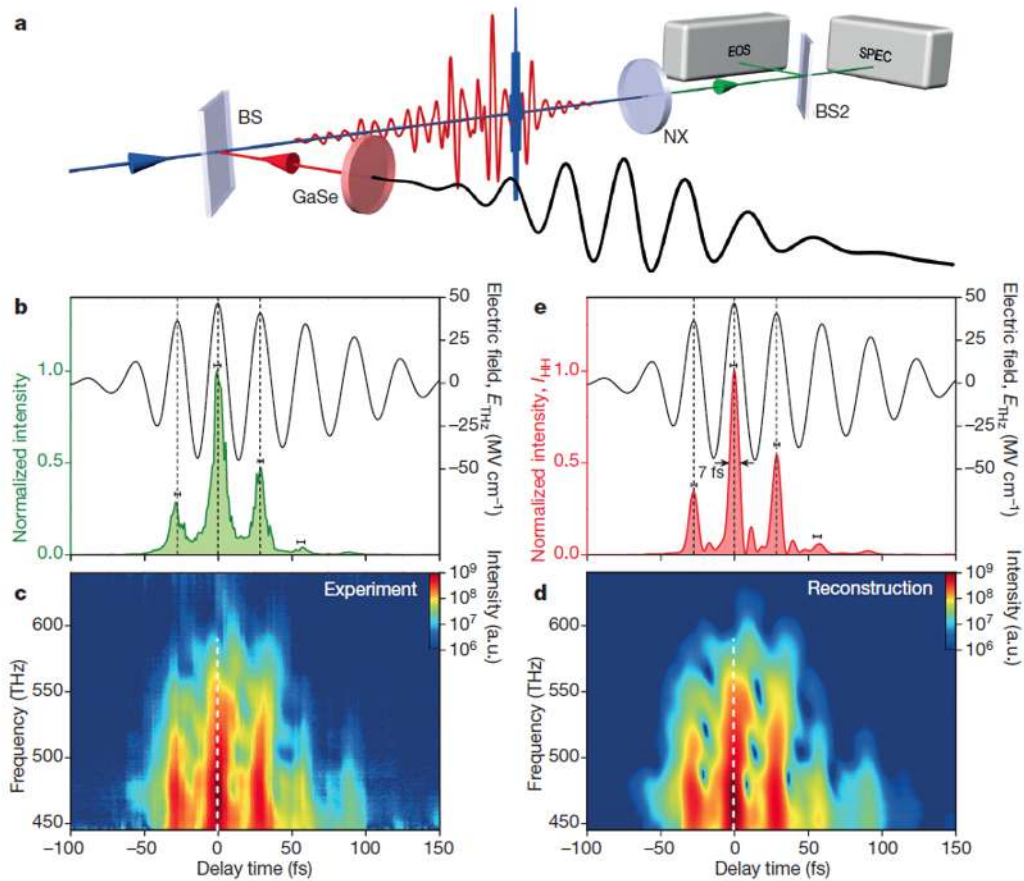


Fig. 3.7: Measured emission dynamics of MIR-driven HHG from bulk GaSe [70]. (a) Experimental setup of the cross-correlation scheme. (b) Waveform of the MIR driving field featuring peak amplitudes of 47 MV/cm and a central frequency of 33 THz ($9 \mu\text{m}$) confirmed by electro-optic detection. (c, d) Spectrograms showing the intensity of the measured sum-frequency signal for different delay times and frequencies as recorded with a Si CCD detector (c) and reconstructed using a double-blind XFROG algorithm (d), respectively. (e) Temporal shape of intensity I_{HH} (red) of the reconstructed HH pulse sequence relative to the driving multi-terahertz waveform (black).

Tab. 3.1: Previous studies of high harmonic generation from solids.

Laser wavelength	Material (\mathcal{E}_g)	Cutoff energy (order) etc.	Reference
3.3 μm (0.38 eV)	ZnO (3.2 eV)	9.5 eV (25th)	[67]
10 μm (0.12 eV)	GaSe (2 eV)	2.7 eV (22nd)	[69]
0.7 μm (1.77 eV)	SiO ₂ (9 eV)	27 eV (15th)	[77]
3.8 μm (0.33 eV)	ZnO (3.2 eV)	5.9 eV (18th), Two-color excitation	[75]
9 μm (0.14 eV)	GaSe (2 eV)	Measurement of the temporal structure of HHG	[70]
1.3 μm (0.93 eV)	Solid Ar, Kr	32.5 eV (35th)	[78]
0.7 μm (1.77 eV)	SiO ₂ (9 eV)	~25 eV, Generation of isolated attosecond pulses and their complete characterization	[79]
1.3 μm (0.93 eV)	MgO (7.8 eV)	19.5 eV (21st), Measurement of the ellipticity dependence	[80]
4.1 μm (0.3 eV)	MoS ₂ (1.8 eV)	3.9 eV (13th), Polarization-resolved measurement	[81]

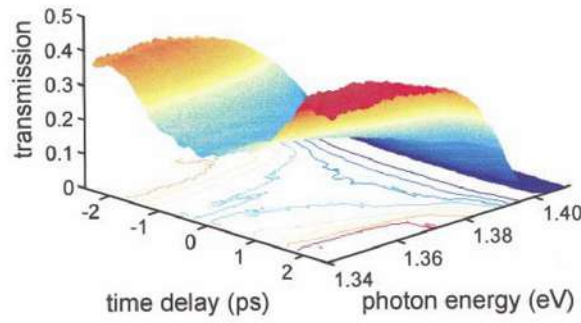


Fig. 3.8: Transmission of a broadband probe pulses through a 350- μm -thick GaAs crystal [24], as a function of time delay between the arrival of the intense 3.5 μm MIR driving pulse and the broadband probe pulses (negative delays correspond to MIR pulses arriving first).

3.3 Franz-Keldysh effect (FKE) induced by strong MIR fields

In this section, we briefly review the recent experimental results for the Franz-Keldysh effect (FKE) induced by strong MIR fields, which is also reported in Chap. 11 of this thesis.

In 1998, Nordstrom *et al.* demonstrated the observation of the experimental signature of excitonic dynamical FKE through its interplay with the AC stark effect [40]. They employed a semiconductor multiple quantum well and the UCSB free-electron laser, which is tunable from $\hbar\omega_0 \sim 0.5$ to 20 meV [82]. The applied electric-field strength is not specified (probably in the range of 1-10 kV/cm, which corresponds to $\gamma_K \approx 1$).

As in the case of HHG from solids, recent developments of laser-based intense MIR sources enabled us to study strong-field phenomena in solids. Using one such source, Chin *et al.* demonstrated the observation of ultrafast induced absorption below the band edge [24]. Figure 3.8 shows the transmission data taken using a 3.5- μm MIR driving field with ~ 1 ps pulse duration and $\sim 2 \times 10^{10}$ W/cm² peak incident intensity ($\langle \mathcal{E}_{\text{kin}} \rangle \approx \hbar\omega_0 = 0.35$ eV). Under these conditions, a dramatic decrease in transmission that extends past 0.2 eV below the band edge ($\mathcal{E}_g = 1.4$ eV) of the 350- μm -thick GaAs sample was observed. This decrease in transmission occurs only during the presence of the intense MIR pulse. The authors also report that the effect is not found to depend on rotation of the sample in the surface plane, suggesting no dependence on crystal orientation. Figure 3.9 shows the line plot of the measured transmission modulation, comparing the 3.5 μm ($\langle \mathcal{E}_{\text{kin}} \rangle \approx \hbar\omega_0 = 0.35$ eV) case and the 6.2 μm case with $\sim 3 \times 10^9$ W/cm² peak incident intensity ($\langle \mathcal{E}_{\text{kin}} \rangle \approx \hbar\omega_0 = 0.2$ eV). With excitation, significant induced absorption is found for photon energies well below the GaAs absorption edge.

In 2011, Ghimire *et al.* reported the intensity dependence of the redshift of the absorption spectra of ZnO crystals induced by intense MIR pulses [83]. In the

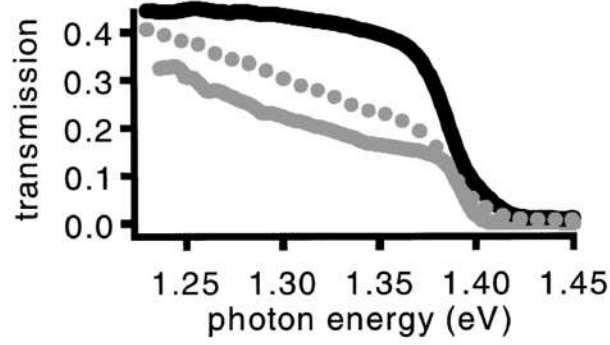


Fig. 3.9: (a) Wavelength dependence of electroabsorption in GaAs (350 μm thick): transmission below the band edge with $\langle \mathcal{E}_{\text{kin}} \rangle \approx \hbar\omega_0$ using 3.5- μm MIR driving pulse (gray line), with $\langle \mathcal{E}_{\text{kin}} \rangle \approx \hbar\omega_0$ using 6.2- μm MIR driving pulse (gray circles), and with no driving pulse (black line). Reprinted from [24].

experiment, strong MIR pulses (3.25 μm , 100 fs) up to ~ 61 MV/cm (5 TW/cm²) were applied to a 500 μm -thick ZnO crystal. Figure 3.10(a) shows the redshift in the absorption edge as a function of the MIR intensity. The data can be fit to a single power law $\propto I^{1/3}$ (dashed line). The $I^{1/3}$ scaling is what is expected for the induced redshift in the static FKE, consistent with tunnel ionization in the instantaneous field of the MIR laser (see Eq. 2.45), where the ionization rate is determined by the ratio $\mathcal{E}_b^{3/2}/|E(t)|$. Thus, the redshift will be proportional to $|E(t)|^{2/3}$ (i.e., $I^{1/3}$). For intensities, $I > 1$ TW/cm², saturation of the redshift was observed. While the redshift saturates, both the spectrally integrated absorption of the probe and the direct tunneling of the MIR laser continue to grow (see Fig. 2 of [83]). The HHG yield is shown in Fig. 3.10(b). The yield for various harmonic orders shows two regimes with different intensity scaling. The redshift deviates from $I^{1/3}$ scaling at the same intensity where the HHG also changes scaling, represented by the shaded regions. In these regions, $\langle \mathcal{E}_{\text{kin}} \rangle$ (~ 7 eV) well exceeding the photon energy, the bandgap, and even the conduction band width (~ 5 eV).

Note that, as summarized in Table 3.2, the above mentioned all experiments with MIR excitation were performed with non-CEP-stabilized pulses with relatively long pulse durations (> 1 ps). Therefore, all the carrier-dependent responses were smeared out.

Transient absorption measurements have also been performed with attosecond pulses with sub-cycle time resolution (Table 3.2). In these experiments, however, attosecond pulses probe the electron states far from the bandgaps, around which are the most important energy regions for the practical applications.

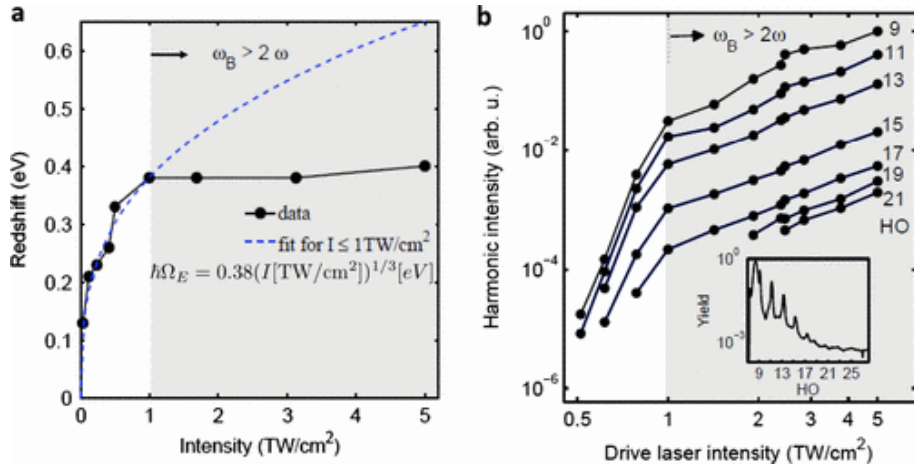


Fig. 3.10: (a) Scaling of the field induced redshift in the absorption edge for ZnO. The data fit a simple Franz-Keldysh model for photon-assisted tunneling up to 1 TW/cm^2 . (b) Dependence of the yield of the MIR harmonics (9th to 21th) to the laser intensity. The individual harmonic yields show two distinct scalings to the drive laser intensity. A portion of the harmonic spectra collected from a $500\text{-}\mu\text{m}$ -thick ZnO crystal at 5 TW/cm^2 is shown in the inset. In both (a) and (b) the shaded region represents a high-intensity regime where the Bloch frequency exceeds twice the MIR frequency. Reprinted from [83].

Tab. 3.2: Previous studies of light-induced transient absorption of bulk crystals.

Laser photon energy pump & probe	Material (\mathcal{E}_g)	Temporal resolution	Reference
0.35 eV & 1.4 eV	GaAs (1.4 eV) etc.	> 1 ps	[24]
0.14-0.26 eV & 1.4 eV	GaAs (1.4 eV)	> 1 ps	[84]
0.38 eV & 3.2 eV	ZnO (3.2 eV)	> 1 ps	[83]
1.6 eV & 105 eV	SiO ₂ (9 eV)	< 1 fs, sub-cycle resolved	[60]
1.6 eV & 100 eV	Si (3.2 & 1.1 eV)	< 1 fs, sub-cycle resolved	[85]
1.6 eV & 43 eV	Diamond (5.5 eV)	< 1 fs, sub-cycle resolved	[86]

Part II

Development of an intense mid-infrared
light sources

In this part, we focus on the development of the light sources which lead us to the frontier of strong-field physics in solids. Before describing the experimental details, a brief introduction of optical parametric amplifiers (OPA) is given in Chap. 5, focusing on their ultra-broadband amplification properties and CEP stabilization properties.

In Chap. 6, I introduce and demonstrate a novel method of OPA to produce CEP-stable intense mid-infrared (MIR) pulses. This method, namely *dual-wavelength OPA*, produces two-color near-infrared (NIR) pulses in a broadband OPA. CEP-stable intense MIR fields are generated via DFG between the generated two-color IR pulses. The generated MIR fields are completely characterized by an electro-optic sampling method (Chap. 8) using 6.5-fs visible pulses generated (Chap. 7).

Through the works demonstrated in this part, the generation and complete characterization of CEP-stable intense MIR fields with a peak electric field exceeding 50 MV/cm are achieved.

Optical parametric amplifiers

Advances in laser technology together with the development of novel high-quality nonlinear optical crystals have transformed ultrafast optical parametric amplifiers (OPAs) to be powerful and practical tools for the study of ultrafast phenomena. OPAs can provide CEP-stabilized intense few-cycle femtosecond pulses tunable across the visible, near and far infrared spectral ranges, and have become a core technology for strong laser-field physics. Here we briefly review the phase-matching properties and CEP stabilization properties of OPA, which have a crucial importance in the state-of-the-art ultrafast laser technology. For comprehensive descriptions of OPA, see Refs [87–90].

5.1 Phase matching in OPA

Optical parametric amplification (OPA) is a three-wave-mixing process in a nonlinear medium, in which a high frequency, high energy pump pulse is depleted in favor of an existing lower frequency, lower energy seed pulse that gets amplified (at least parts of it) to the signal pulse. This process can be described as three-wave mixing process in the regime of conventional nonlinear optics.

In the process, a third pulse is generated, called idler pulse, whose angular frequency is determined by energy conservation. For the instantaneous angular frequencies ω_p , ω_s , and ω_i of the pump, signal and idler, respectively, energy conversion reads

$$\hbar\omega_p = \hbar\omega_s + \hbar\omega_i . \quad (5.1)$$

If we assume the signal is at higher frequency, i.e., $\omega_s > \omega_i$, the signal and idler frequency can range from $\omega_p/2 < \omega_s < \omega_p$ and the corresponding idler ranges from $\omega_p/2 > \omega_i > 0$. The case, where signal and idler are both $\omega_p/2$, is called degenerate parametric amplification, which is a delicate process especially if both the signal and idler beam occupy the same mode, i.e., they can not be distinguished and are identical.

Besides energy conservation, momentum conservation (called *phase matching*) also has to be fulfilled for an efficient interaction. This can be written as

$$\hbar\mathbf{k}_p = \hbar\mathbf{k}_s + \hbar\mathbf{k}_i \quad (5.2)$$

with \mathbf{k}_p , \mathbf{k}_s , \mathbf{k}_i being the respective wave vectors. In the following, we consider the three waves are linearly polarized (not necessary to be parallel each other) and

propagates collinearly, i.e., k_p, k_s, k_i . To achieve maximum gain in OPA, we need to satisfy the phase-matching condition,

$$\Delta k = k(\omega_p) - k(\omega_s) - k(\omega_i) = 0. \quad (5.3)$$

For ultrafast applications, in addition, we need to satisfy the phase-matching condition as broad as possible because the phase matching bandwidth determines the gain bandwidth of OPA.

Let us assume that perfect phase matching is achieved for a given signal frequency ω_s (and for the corresponding idler frequency $\omega_i = \omega_p - \omega_s$). If the signal frequency increases to $\omega_s + \Delta\omega$, energy conservation requires that the idler frequency decreases to $\omega_i - \Delta\omega$. The wave vector mismatch can then be approximated to first order as

$$\Delta k = -\frac{dk_s}{d\omega} \Delta\omega + \frac{dk_i}{d\omega} \Delta\omega = \left(\frac{1}{v_i} - \frac{1}{v_s} \right) \Delta\omega, \quad (5.4)$$

where $v_q = dk/d\omega|_{\omega_q}$ ($q = p, s, i$) are the corresponding group velocities of pump, signal and idler. Within the large-gain approximation, the FWHM phase-matching bandwidth can then be calculated as [91, 92]

$$\Delta f = -\frac{2\sqrt{\ln 2}}{\pi} \sqrt{\frac{\Gamma}{L}} \frac{1}{|1/v_i - 1/v_s|}. \quad (5.5)$$

Here, Γ is the maximum gain achieved under perfect phase matching, i.e., $\Delta k = 0$. Large group velocity mismatch between signal and idler waves dramatically decreases the phase-matching bandwidth. Inversely, larger gain bandwidth can be expected when the OPA approaches degeneracy, i.e., $\omega_s = \omega_i$, in type-I phase matching or in the case of group-velocity matching between signal and idler ($v_s = v_i$). Obviously, in this case Eq. (5.5) loses validity and the phase mismatch Δk must be expanded up to second order yielding

$$\Delta f = -\frac{2\sqrt[4]{\ln 2}}{\pi} \sqrt[4]{\frac{\Gamma}{L}} \frac{1}{2|d^2k_s/d\omega^2|}. \quad (5.6)$$

The OPAs operated under this condition are called *Degenerate OPA*.

Degenerate OPA

As mentioned above, a degenerate OPA means that the the signal and the idler have the same central frequency, $\omega_{s0} = \omega_{i0}$, and the same dispersion (i.e., their in the same polarization and propagation direction), $k_s(\omega) = k_i(\omega)$. This condition intrinsically zeroes the group velocity mismatch, making it suitable for broadband parametric amplification.

In order to obtain analytical expressions for the phase-matching bandwidth, the phase mismatch, $\Delta k (= k_p - k_s - k_i)$, is usually expanded by a Taylor series. Assuming

in a first approximation that the pump is monochromatic, the signal wave vector is expanded as

$$k_s(\omega) = k_s(\omega_{s0}) + \left. \frac{\partial k_s(\omega)}{\partial \omega} \right|_{\omega=\omega_{s0}} \Delta\omega + \frac{1}{2!} \left. \frac{\partial^2 k_s(\omega)}{\partial \omega^2} \right|_{\omega=\omega_{s0}} (\Delta\omega)^2 + \dots \quad (5.7)$$

In the same way, the idler wave vector is expanded as

$$k_i(\omega) = k_i(\omega_{i0}) - \left. \frac{\partial k_i(\omega)}{\partial \omega} \right|_{\omega=\omega_{i0}} \Delta\omega + \frac{1}{2!} \left. \frac{\partial^2 k_i(\omega)}{\partial \omega^2} \right|_{\omega=\omega_{i0}} (\Delta\omega)^2 + \dots, \quad (5.8)$$

where $\Delta\omega$ denotes the frequency change of the signal, and by energy conservation, $\omega_p = \omega_s + \omega_i$, the idler frequency change is $-\Delta\omega$. With Eqs. (5.7) and (5.8), the phase mismatch can be expressed as

$$\begin{aligned} \Delta k &= k_p(\omega_p) - k_s(\omega_{s0}) - k_i(\omega_{i0}) \\ &- \left(\left. \frac{\partial k_s(\omega)}{\partial \omega} \right|_{\omega=\omega_{s0}} - \left. \frac{\partial k_i(\omega)}{\partial \omega} \right|_{\omega=\omega_{i0}} \right) \Delta\omega \\ &- \frac{1}{2!} \left(\left. \frac{\partial^2 k_s(\omega)}{\partial \omega^2} \right|_{\omega=\omega_{s0}} + \left. \frac{\partial^2 k_i(\omega)}{\partial \omega^2} \right|_{\omega=\omega_{i0}} \right) (\Delta\omega)^2 \\ &- \frac{1}{3!} \left(\left. \frac{\partial^3 k_s(\omega)}{\partial \omega^3} \right|_{\omega=\omega_{s0}} - \left. \frac{\partial^3 k_i(\omega)}{\partial \omega^3} \right|_{\omega=\omega_{i0}} \right) (\Delta\omega)^3 \\ &- \frac{1}{4!} \left(\left. \frac{\partial^4 k_s(\omega)}{\partial \omega^4} \right|_{\omega=\omega_{s0}} + \left. \frac{\partial^4 k_i(\omega)}{\partial \omega^4} \right|_{\omega=\omega_{i0}} \right) (\Delta\omega)^4 + \dots \end{aligned} \quad (5.9)$$

Apparently, all of the odd terms in (5.9) are cancelled out if $k_s(\omega) = k_i(\omega)$ and $\omega_{s0} = \omega_{i0}$. It is this characteristics that the gain-bandwidth of a degenerate-OPA to be broadband. The zeroth-order phase mismatch, $k_p(\omega_p) - k_s(\omega_{s0}) - k_i(\omega_{i0})$, imposes the condition $\omega_p = 2\omega_{s0}(= 2\omega_{i0})$ in the case of a degenerate OPA. This condition, for example, can be automatically fulfilled by using the second harmonic as pump and the (spectrally-broadened) fundamental as seed [93].

When a degenerate OPA is operated at a signal wavelength where the GDD of the OPA crystal becomes zero, $\partial^2 k_s(\omega)/\partial \omega^2|_{\omega=\omega_{s0}} = 0$ ($= \partial^2 k_i(\omega)/\partial \omega^2|_{\omega=\omega_{i0}}$), the gain-bandwidth can be further broadened. Table 5.1 shows the possible schemes of a degenerate OPA fulfilling the zero-GDD condition. Note that the zero GDD of BiB_3O_6 (BiBO) crystals occurs at $\omega_{s0} \sim 1.6$ [μm], which implies $\omega_p \sim 0.8$ [μm], hence, Ti:sapphire lasers can be employed as a pump source. It has been experimentally confirmed that this scheme provides a nearly one-octave gain-bandwidth which supports sub-two-cycle pulse durations around a wavelength of 1.6 μm [94–98], and can be one of ideal drivers for HHG aiming the generation of attosecond soft X-ray pulses [99].

Tab. 5.1: Degenerate OPA schemes pumped below 1 μm . Gain bandwidths ($\Delta\lambda$, $\Delta\nu$) are calculated at the 1/2 level (5-mm crystal length, 50-GW/cm² pump intensity). Adapted from [96].

Crystals	Interaction type (Principal plane)	λ_p [μm]	$\Delta\lambda$ [μm]	$\Delta\nu$ [THz]
KDP	ooe	0.49	0.82–1.23	123 THz
PPSLT	eee	0.56	0.97–1.34	87 THz
LBO	ooe (x - y)	0.60	0.94–1.63	133 THz
CLBO	ooe	0.63	1.00–1.71	135 THz
BBO	ooe	0.72	1.12–1.98	116 THz
BiBO	ooe (x - z)	0.79	1.23–2.14	104 THz
BiBO	ooe (x - z)	0.81	1.28–2.18	98 THz
PPKTP	eee	0.89	1.51–2.19	61 THz
LiNbO ₃	ooe	0.95	1.69–2.17	39 THz
PPLN	eee	0.96	1.71–2.18	39 THz
LiIO ₃	ooe	0.97	1.61–2.94	84 THz
KNbO ₃	ooe (x - y)	0.99	1.63–2.51	65 THz
KNbO ₃	ooe (y - z)	1.00	1.66–2.55	64 THz

5.2 CEP stabilization in nonlinear wave-mixing processes

One of the most intriguing and technologically important features of ultrashort-pulse parametric amplifiers is the possibility to realize passively carrier-envelope phase (CEP)-stable pulses. Because of the paramount importance of this self-CEP-stabilization technique for attosecond science and strong-field physics, we briefly review the phase relations in parametric amplifiers, as discussed in greater detail in [89, 90].

5.2.1 Phase sum rules of nonlinear processes

The CEP of a light pulse can be manipulated both by linear and nonlinear processes. In linear processes, such as propagation in a dispersive medium, the difference between the group and phase velocities leads to a slip of the carrier with respect to the envelope; by means of wedged glass plates of variable thickness, it is possible to exploit this effect to set the CEP and to compensate for drifts. If nonlinear optical processes occur, they lead to the mixing of the optical frequencies and of the spectral phases. In the following, we will briefly explain how nonlinear processes allow manipulating the CEP and measuring its fluctuations. We first consider the case of nonlinear three-wave mixing, in which three waves of frequencies ω_1 , ω_2 and ω_3 , with $\omega_3 = \omega_1 + \omega_2$, are coupled in a second-order nonlinear crystal. Similarly to the frequency conservation, the CEPs of the three waves are also linked by the relationship: $\phi_3 = \phi_1 + \phi_2 + \text{const.}$ [90]. The value const. varies depending on the boundary condition applied. For the case of difference-frequency generation (DFG),

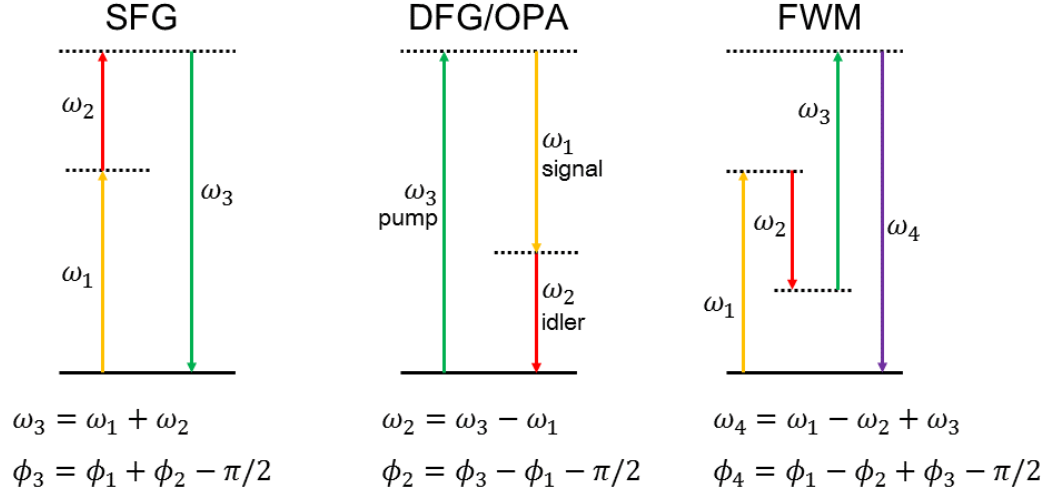


Fig. 5.1: Frequency and phase summation rules for (a) sum-frequency generation (SFG), (b) difference-frequency generation (DFG), equivalent to the generation of the idler wave in an OPA, and (c) four-wave mixing (FWM) process.

which is equivalent to the process of idler generation in an OPA, i.e., $\omega_2 = \omega_3 - \omega_1$, $\text{const.} = \pi/2$ [90]. Consequently, $\phi_2 = \phi_3 - \phi_1 - \pi/2$ (Fig. 5.1(b)).

A very similar effect occurs in the third-order nonlinear process of four-wave mixing (FWM), in which four waves at frequencies $\omega_1, \omega_2, \omega_3$ and ω_4 , with $\omega_4 = \omega_1 - \omega_2 + \omega_3$, are coupled in a third-order nonlinear medium. The CEPs of the waves are linked by the relationship: $\phi_4 = \phi_1 - \phi_2 + \phi_3 - \pi/2$ (Fig. 5.1(c)). If we consider that the mixing frequencies belong to the same beam and hence share the same CEP $\phi_1 = \phi_2 = \phi_3 = \phi$, then the newly generated frequency component ω_4 will have the CEP $\phi_4 = \phi_1 - \phi_2 + \phi_3 - \pi/2$. This demonstrates that the newly added frequency components inherit the original value of the CEP of the driving pulse. This discussion is applicable to self phase modulation (SPM), which is the dominant nonlinear interaction behind the spectral broadening in transparent materials (gases and solids) [100–102].

5.2.2 Passive stabilization of the CEP

The passive method is all-optical approach for the generation of CEP-stable pulses (see [90] for *active CEP stabilization*). If a DFG process $\omega_2 = \omega_3 - \omega_1$ occurs between two pulses with the same shot-to-shot CEP fluctuations ϕ , so that $\phi_1 = \phi$ and $\phi_3 = \phi + \mathcal{C}$, then $\phi_2 = \phi_3 - \phi_1 - \pi/2 = \mathcal{C} - \pi/2 = \text{const.}$, i.e., the fluctuations of ϕ are automatically cancelled. Passive CEP stabilization has some clear advantages with respect to the active one: (i) being an all-optical technique, it does not require any electronic feedback circuits imposing bandwidth limitations; (ii) it directly produces a train of CEP-stable pulses, avoiding the need to pick pulses at a fraction of ν_{CEO} .

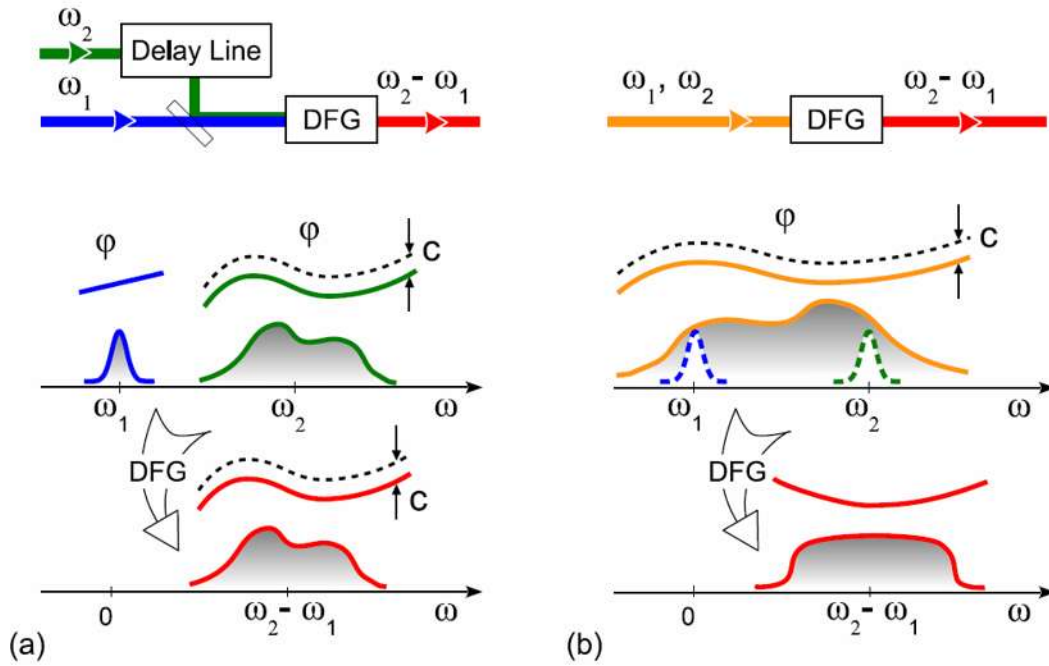


Fig. 5.2: Comparison of (a) inter-pulse and (b) intra-pulse stabilization schemes. Lower panels provide the evolution of both intensity and phase in the frequency domain; ϕ is the absolute phase, \mathcal{C} denotes fluctuations of the CEP [90].

There are two possible experimental implementations to realize passive CEP stabilization, i.e., *interpulse* DFG and *intrapulse* DFG. Interpulse DFG processes involve mixing of two separate frequency-shifted pulses with the same CEP synchronized by a delay line, as schematically represented in Fig. 5.2(a). Inter-pulse DFG also occur in OPAs, since DFG is equivalent to the process of idler generation in an OPA. When the signal and the pump pulses of the OPA are derived from the same source, the idler pulses become CEP-stable. Intra-pulse schemes involve mixing between different frequency components of a single ultrabroadband pulse, as depicted in Fig. 5.2(b). In this case, the frequencies are intrinsically CEP-locked.

In the case of inter-pulse DFG, the resulting CEP of the difference-frequency components is influenced by any relative fluctuation of the CEP \mathcal{C} . In the case of the intra-pulse DFG, in contrast, the effects of fluctuations \mathcal{C} are completely cancelled out via DFG process.

Generation of carrier-envelope phase-stable intense mid-infrared pulses

In this chapter, the development of an intense femtosecond MIR light source with passive CEP stabilization is described. The CEP stabilization of the MIR pulses is achieved by generating a difference frequency between the two spectral components in the NIR region produced from an inline dual-wavelength BiBO OPA. The characterization of electric waveform of the MIR pulses will be presented later in Chapter 8 by the electro-optics sampling (EOS).

6.1 Experiment

6.1.1 Dual-wavelength OPA

Femtosecond MIR pulses are conventionally generated as difference frequencies between signal and idler pulses from an NIR OPA pumped by femtosecond 800-nm pulses from a Ti:sapphire amplifier. Although this method is easy to implement and efficient, the CEP of the MIR pulses cannot be stabilized because the phases of the signal and idler pulses change randomly from shot to shot without having specific relationship between them. So far CEP-stabilized MIR pulses are generated by difference frequency mixing between the signal pulses produced in individual OPAs seeded from a common white light [65]. However, in this method, inevitable timing jitter between the two signals causes the fluctuation of the difference frequency's CEP, making a light source complicated and unreliable. A dual-wavelength OPA is proposed and demonstrated (Fig. 6.1), where two-color NIR pulses for DFG are produced in a common NIR OPA. White light generation in a thin YAG crystal is used to supply a seed for the dual-wavelength OPA because the spectral intensity of the white light from the YAG crystal tends to be stronger than that of the white light from a commonly used sapphire plate [103]. The seed pulses pass through a fused silica block and are stretched in time. The spectral dispersion introduced in the fused silica is dominated by the third-order dispersion (TOD) rather than the second-order dispersion in the NIR region because the zero group delay dispersion (GDD) occurs at 1270 nm in fused silica. Therefore, the temporal distribution of the seed spectrum becomes parabolic. After the pulse stretching, a short pump pulse amplifies selectively the discrete two color components at the same time. The frequency difference of the two colors can be controlled by the timing between the pump and the seed pulses, providing spectral tunability of the MIR pulses, while the central wavelength of the two colors is always at the zero GDD wavelength (1270

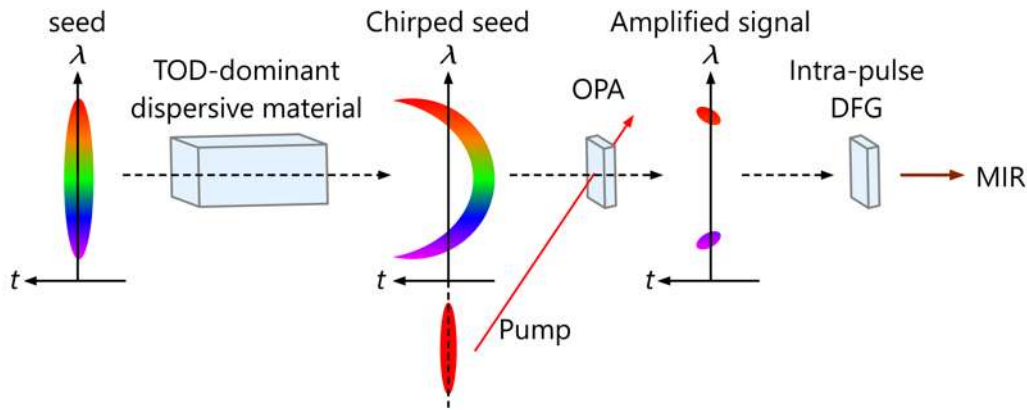


Fig. 6.1: Concept of the dual-wavelength OPA.

nm). Because of the common seed for these two amplified components and this inline scheme without spatial and temporal separations, CEP-stabilization of the MIR pulses in DFG is intrinsically ensured as described in Sect. 5.2.2.

6.1.2 Generation of CEP-stable mid-Infrared pulses

Figure 6.2 shows a schematic of the dual-wavelength OPA followed by DFG. A Ti:sapphire CPA system produced 7-mJ, 40-fs, 0.8 μm pulses at a repetition rate of 1 kHz with a shot-to-shot energy stability of 1.9%, which were divided into four pulses.

One of the four pulses with an energy of 1 mJ was focused into a krypton-filled gas cell to broaden its spectrum via filamentation. These pulses were used as a sub-cycle probe in the EOS. For details of the visible pulse generation, see Chap. 7. The spectral components from 530 to 700 nm were selected and compressed using several dielectric mirrors, resulting in 6.5-fs pulses and a pulse energy of 5 μJ with a shot-to-shot energy stability of less than 2%.

The other three pulses were used to generate a white light continuum in a 4-mm-thick YAG crystal and pump pulses for two-stage OPAs. Figure 6.3 shows the white light spectrum in the NIR, where the strong short-wavelength components below 1100 nm were suppressed by a Si filter. The NIR components of the white light continuum, which extended to >1800 nm, were used as a seed for the following OPA stages. The seed pulses passed through a 150-mm-long synthetic fused silica (SK1310, Ohara quartz) in two pass configuration. Figure 6.4(a) shows the group delays introduced by 300-mm-long fused silica, where the zero GDD occurs at 1270 nm [104]. The highly dispersed seed pulses were then amplified as a signal in the two-stage OPAs that employed 1-mm-thick BiB_3O_6 (BiBO) crystals. A BiBO-based OPA using a 800-nm pump supports ultrabroadband amplification from 1200 to 2200 nm, fully covering the entire spectral range required in the dual-wavelength OPA [97, 105], as seen in Sect. 5.1.

Because of the parabolic group delays introduced by the fused silica, two spectral components were selectively amplified by the OPAs that were pumped by 40-fs

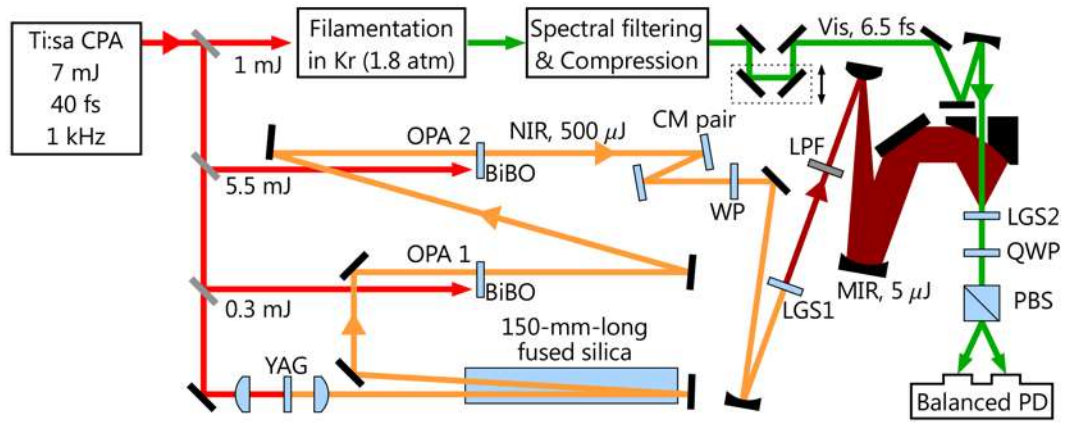


Fig. 6.2: Schematic of the experimental setup. YAG, 4-mm-thick YAG crystal; BiBO, 1-mm-thick BiB_3O_6 crystals; CM pair, a pair of broadband NIR chirped mirrors; WP, waveplate; LGS1, 1-mm-thick LiGaS_2 crystal; LPF, low-pass filter; LGS2, 15- μm -thick LiGaS_2 crystal; QWP, quarter waveplate; PBS, polarizing beam splitter.

pulses at 800 nm as shown in Fig. 6.4(b). An output energy of 500 μJ was typically obtained after the second OPA stage with a shot-to-shot energy stability of 3.9%. We evaluated the influence of the timing jitter between the pump and seed pulses on the spectral fluctuation of the two components. The spectral stability of the short and long spectral components were measured to be 1.1 and 2.9 nm, respectively, which corresponded to a timing jitter of 3.8 fs. A pair of broadband NIR chirped mirrors [106] was set after the OPAs to compensate the group delay difference between the two spectral components. To achieve type II phase matching in DFG, a specially designed waveplate was used to rotate the polarization of the component at 1200 nm by 90° while retaining the polarization of the 1400-nm component. The NIR pulses were then fed into a 1-mm-thick LiGaS_2 (LGS) crystal for DFG [107, 108]. Figure 6.5 plots the phase mismatch $|\Delta k L|$ for phase matching in the xy -plane of LGS with a pump at 1200 nm and $L = 1$ mm. The focused intensity at the LGS crystal was estimated to be 200 GW/cm^2 . A germanium low-pass filter, indicated as LPF in Fig. 6.2, was placed behind the crystal to remove the co-propagating NIR pulses. The MIR pulse energy after the filter was measured to be 5 μJ . The MIR spectrum is shown in Fig. 8.9(b) in Chap. 8, where the waveform characterization of the MIR fields is demonstrated. As shown in Fig. 6.4(a), the tunable range of this method is from 4.6 to 11 μm . The shorter wavelength limit is determined by the gain bandwidth of BiBO where the parametric gain drops below 1.2 μm , while the longer wavelength limit is determined by the transmission range of the LGS crystal.

6.2 Summary

In this chapter, an intense femtosecond MIR light source with passive CEP stabilization using the novel dual-wavelength OPA is proposed and demonstrated. Two-color NIR pulses with an energy of up to 500 μJ are produced from the dual-wavelength OPA. Difference frequency mixing of the NIR pulses results in the 5 μJ

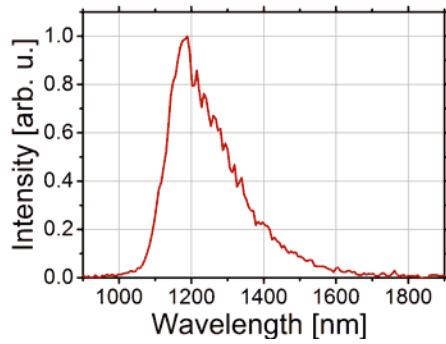


Fig. 6.3: WLG spectrum in a 4-mm-thick YAG plate. The short wavelength components below 1100 nm were cut by a Si filter.

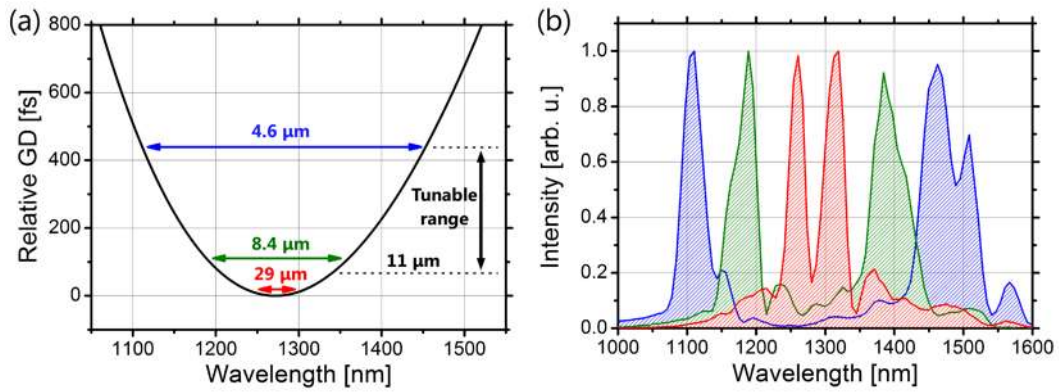


Fig. 6.4: (a) Relative group delays of 300-mm-long fused silica [10]. (b) Typical output spectra from the second stage OPA (OPA 2) in Fig. 6.2. The colors of the plots correspond to the colors of the arrows in Fig. 6.4(a) that indicate the intervals of the spectral peaks.

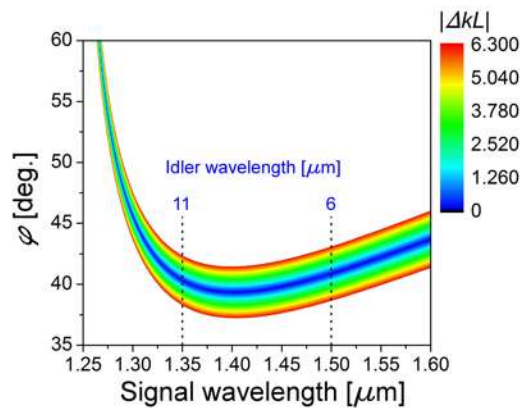


Fig. 6.5: Phase mismatch in 1-mm-thick LGS (xy -plane, pumped at $1.2 \mu\text{m}$), calculated from the Sellmeier equation in Ref. [109].

MIR pulses spanning from 5 to 11 μm . The pulse characterization of the MIR pulses by the EOS using 6.5-fs visible pulses and the passive CEP stabilization and its drift will be presented in Chapter 8.

Generation of spectrally stable 6.5-fs visible pulses

7.1 Motivations

Sub-cycle spectroscopy requires short-wavelength probe pulses whose pulse duration is much shorter than at least a half of one optical cycle of a CEP-stable long-wavelength pump field. For example, MIR light fields with a wavelength of $8\ \mu\text{m}$ needs the probe pulse duration well below 13.3 fs. Here the generation of ultrashort visible pulses with a pulse duration of 6.5 fs is demonstrated. These visible pulses are indispensable to characterize the waveform of the MIR pulses from the dual-wavelength OPA, which were described in Chap. 6 as well as to probe sub-cycle dynamics in transient absorption spectroscopy as will be presented in Chap. 11.

Ultrashort visible pulses can be achieved by several approaches. The first is a BBO-based noncollinear OPA (NOPA) pumped by the second harmonic of Ti:sapphire lasers [110, 111]. A NOPA is usually complicated and less stable due to many nonlinear processes involved. In addition, the total beam path required to set the NOPA is quite long, making it difficult to synchronize the MIR and probe pulses. The second is to use self-phase modulation (SPM) in a gas-filled hollow fiber [112]. There are few applications in pump-probe spectroscopy [113], mainly because the output spectra are less smooth than the output from NOPAs. Furthermore, good pointing stability and short pulse duration (<30 fs) of the input pulses are necessary for stable and broad output spectra.

In this chapter, we demonstrate the generation of 6.5-fs visible pulses adopting spectral broadening based on filamentation in a gas-filled cell [114–117], which is advantageous over the two approaches mentioned above in several aspects: (i) wide and smooth output spectra that cover the visible region with an energy of $>1\ \mu\text{J}$, (ii) free-space nonlinear propagation that has spatial filtering effects [118] as well as removing the beam pointing issue, (iii) a wide acceptance range of the input pulse duration up to ~ 100 fs, and (iv) simplicity and robustness.

7.2 Experiment

7.2.1 Filamentation and pulse compression

Figure 7.1 shows the experimental setup of filamentation and pulse compression. The output pulses from a Ti:sapphire CPA system (1 mJ, 40 fs, 800 nm) operated at 1 kHz were loosely focused by a lens ($f = 1000$ mm) to a 1-m-long gas cell filled with krypton at 1.8 atm. Filamentation in the gas cell produced white light that covered from 350 to 2000 nm. Shorter wavelength components below 350

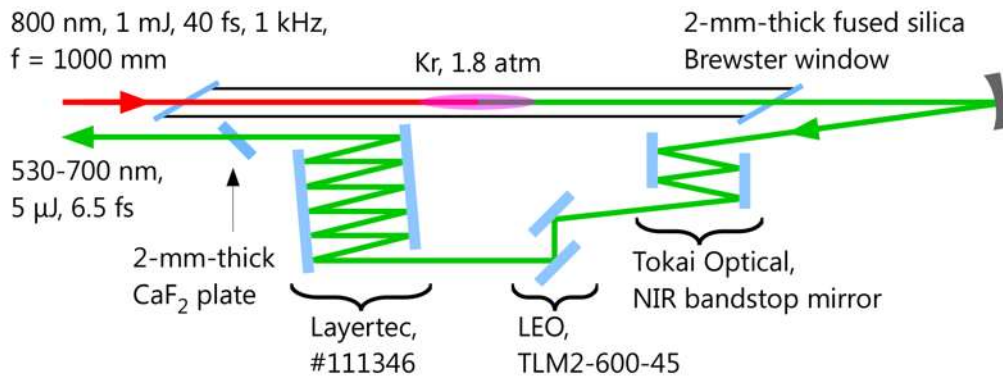


Fig. 7.1: Schematic of the experimental setup. Note that all beams are perpendicularly polarized with respect to the plane of the paper. The Brewster windows of the gas-filled cell were drawn to be rotated by 90 degrees intentionally for readers.

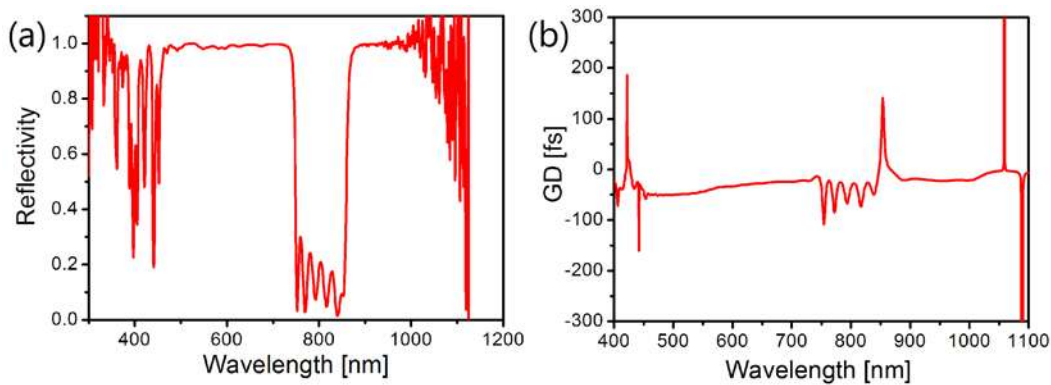


Fig. 7.2: (a) Measured reflectivity and (b) group delay of the band-stop mirror.

nm are suppressed due to the low reflectivity of silver mirrors. As shown in Fig. 7.1, we used two kinds of dielectric mirrors for spectral selection and a pair of chirp mirrors for pulse compression. First, the pulses were reflected 4 times on two NIR band-stop mirrors (Tokai Optical Co., Ltd), which were specially designed to suppress the fundamental spectral components in 720-850 nm. Figures 7.2a) and (b) show the measured reflectivity and group delay of the band-stop mirror, respectively. The reflectivity was measured with a spectrophotometer (JASCO Co., V-570), and the group delays was measured by a home-built white-light interferometer [14]. The group delay dispersion is approximately -30 fs^2 at 630 nm. This mirror can efficiently block the fundamental components while it does not affect the phase of the spectrally broadened components. This band-stop mirror was originally designed for difference frequency generation between the short and long wavelength components after spectral broadening [95]. Therefore, it has the high reflectivities in a long-wavelength region above 850 nm. To reduce the remaining long-wavelength components, we used two dielectric mirrors (Lattice Electro Optics, Inc., TLM2-600-45). The incoming beam was s-polarized at these mirrors to maximize the reflected bandwidth. In total, four bounces on the band-stop mirrors and two bounces on the broadband dielectric mirrors allowed us to select the visible part in 530-700 nm,

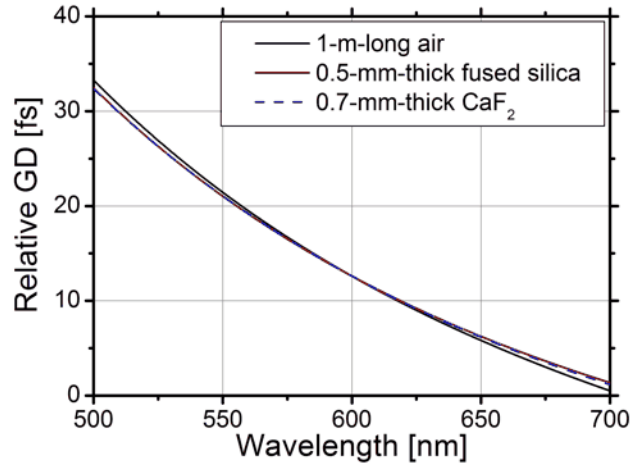


Fig. 7.3: Relative group delays of 1-m-long air (black line), 0.5-mm-thick fused silica (red line), and 0.7-mm-thick CaF₂ (blue dashed line).

as shown in the black line in Fig. 7.4(d). Dispersion compensation was achieved by five bounces on each of a pair of chirped mirrors (Layertec GmbH, #111346, approximately -80 fs^2 per double bounces at 630 nm). This chirped mirror pair can compensate the dispersion of 1.5-mm-thick fused silica or 2.1-mm-thick calcium fluoride (CaF₂) plates per one round trip. We slightly rotate a 2-mm-thick CaF₂ plate around the Brewster angle to control the dispersion by changing the incident angle.

Figure 7.3 shows the dispersion of 1-m-long air in the standard condition [119] that is nearly identical to the dispersion of 0.5-mm-thick fused silica [104] or 0.7-mm-thick CaF₂ [120]. As can be seen in Fig. 7.3, the dispersion of the air would significantly introduce the group delay dispersion when the propagation length exceeds $\sim 0.1 \text{ m}$. Therefore, we optimized the dispersion of the visible pulses at the point of use by adjusting the number of reflections on the chirped mirrors as well as changing the effective thickness of a fused silica or CaF₂ plate in the beam path.

The compressed pulses were characterized by the second-harmonic generation-based frequency-resolved optical gating (SHG-FROG) [121, 122] that employed an 8- μm -thick BBO crystal. We obtained the nearly-transform-limited 6.5-fs pulses with a pulse energy of 5 μJ and a smooth spectrum in 530-700 nm as shown in Fig. 7.4.

7.2.2 Beam profile and pointing stability measurement

The beam profile and pointing stability after the pulse compression are investigated. Figures 7.5(a) and (b) show the near-field and the far-field beam profiles, respectively. Because of the spatial filtering effect in filamentation, both of the beam profiles had a nearly Gaussian shape. The $1/e^2$ intensity beam radii of the near-field beam profile were measured to be 936 μm and 862 μm along the horizontal (X) and vertical (Y) directions, respectively, and those of the far-field beam profile were 79 μm and 82 μm . Pointing stability of the beam before focusing was measured by a

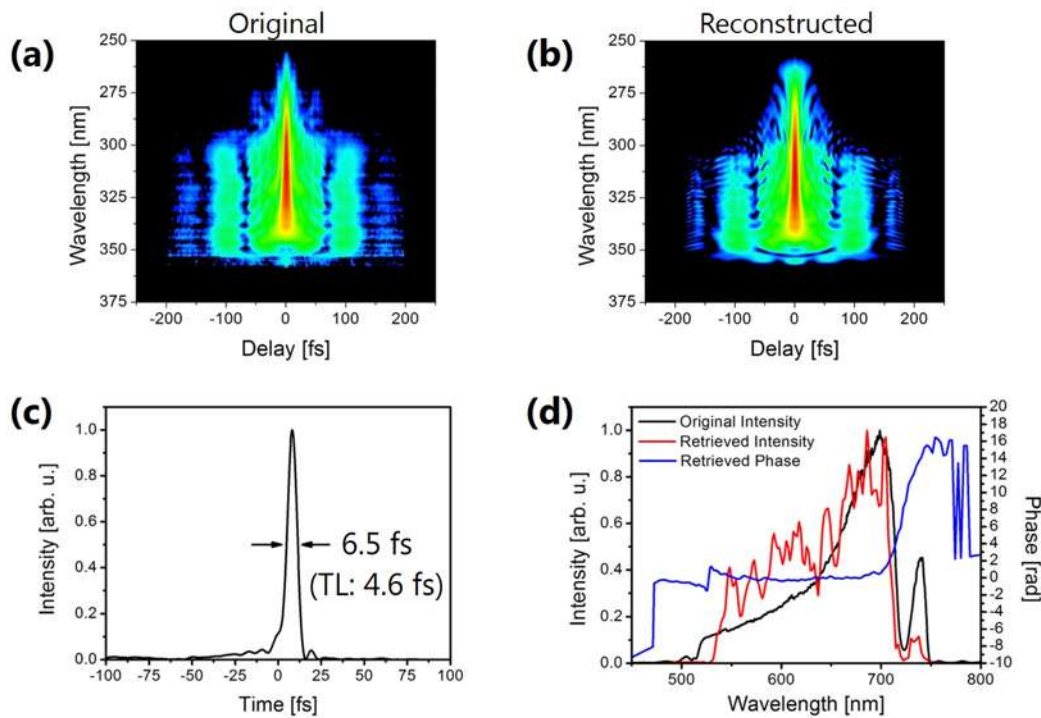


Fig. 7.4: Results of SHG-FROG measurement. (a), (b) Measured and reconstructed FROG traces, respectively. (c) Retrieved temporal intensity profile (measured: 6.5 fs, transform-limited case: 4.6 fs), (d) Intensity spectrum measured by a spectrometer (black line), retrieved spectrum (red line), and retrieved spectral phase (blue line).

quadrant-cell photo-detector. The fluctuation of the beam center with respect to the $1/e^2$ intensity beam radius was $\sim 5 \times 10^{-3}$.

7.2.3 Spectral stability measurement

We also measured the stability of the broadened spectral components from 400 to 700 nm since shot-to-shot reproducibility is essential for various spectroscopic applications. A bandpass filter (Thorlabs, Inc., FESH0700) was set just behind the gas-filled cell to select the spectral components from 400 to 700 nm, then measured a collection of single-shot spectra using a spectrometer (Ocean Optics, Inc., HR2000+). Figures 7.6 (a) and (b) show the averaged spectrum over 1,000 shots and the standard deviation of each spectral component, respectively. The standard deviation of the pulse energies before filamentation process was measured to be 1.97%. Figure 7.6(b) shows that the spectral instabilities of the white light in 420-650 nm were $\sim 2\%$, which are similar to the fluctuation of the input pulse energy. The shot-to-shot fluctuation in 650-750 nm is slightly higher than that of 420-650 nm, which was probably due to the self-phase modulation in the exit window of the cell. These results show that the white light continuum produced by filamentation in a gas-filled cell is suitable for spectroscopic applications.

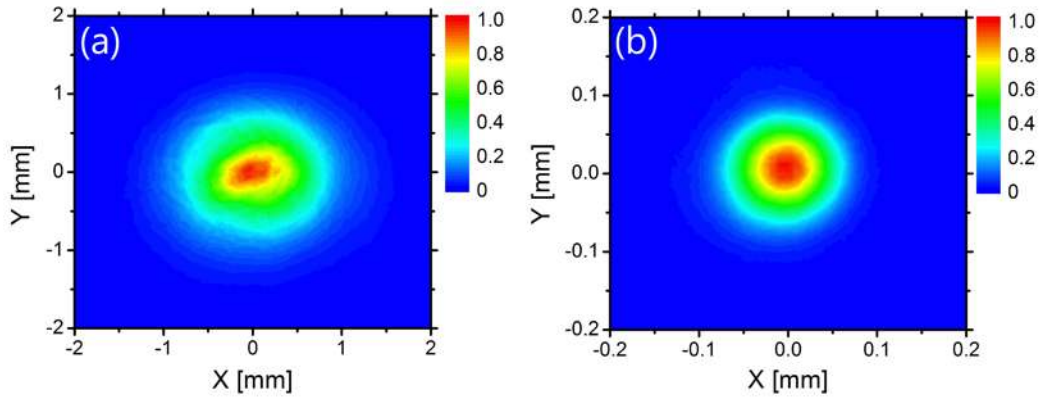


Fig. 7.5: Beam profiles of the compressed pulse (a) before and (b) after focusing with a concave mirror ($f=300$ mm).

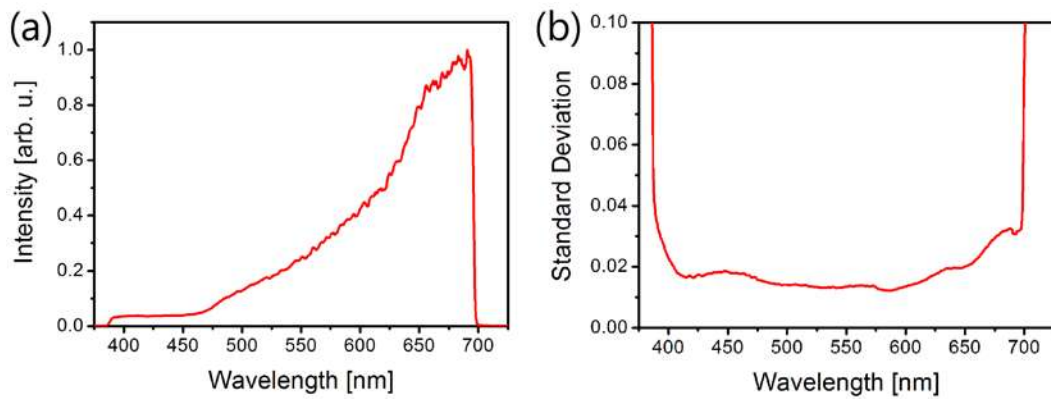


Fig. 7.6: Results of the spectral stability measurement. (a) Averaged spectrum of 1,000 single-shot spectra. (b) Standard deviation of each spectral component.

7.3 Summary

We produced 5- μ J, 6.5-fs visible pulses at a repetition rate of 1 kHz using filamentation in a gas cell filled with krypton followed by spectral selection and dispersion compensation by a combination of dielectric mirrors. This pulse compression scheme is simple and robust, and can be easily integrated into intense ultrashort-pulse laser systems. The generated visible pulses are used as a sub-cycle probe for the CEP-stabilized MIR light fields in Chaps. 8 and 11. The shot-to-shot spectral instabilities of the visible continuum were measured to be $\sim 2\%$ (standard deviation) in 420-650 nm, which was almost the same as the energy fluctuation of the output pulses from the Ti:sapphire chirped pulse amplifier. Note that, the smoothness and the stability of the spectral profile are crucial for spectroscopic studies, as will be demonstrated in Chap. 11.

Waveform characterization of MIR light fields

In this chapter, the electro-optical sampling (EOS) technique [44] by a LGS crystal is used to characterize the waveform of the MIR pulses, which was described in Chap. 6. The visible pulses with a duration of 6.5 fs, presented in Chap. 7, are used as a probe for the EOS. Timing-jitter between the MIR and visible pulses is evaluated independently, verifying possibility to adopt the EOS technique in our system. Long-term EOS measurements allow us to set the upper limit in the CEP drift of the MIR pulses as well as the timing drift between the two pulses.

Direct sampling of an electric field has been realized to characterize a terahertz electric field with synchronized 100-fs NIR pulses by either photoconductive switching [123] or the EOS [44]. This method has been extended into the MIR spectral region by using few-cycle pulses in the NIR [124–128]. Recently, EOS of electric waveforms at NIR wavelengths as short as 1.2 μm (230 THz) has been demonstrated by use of 4-fs NIR pulses and a 10- μm -thick BBO crystal [129].

8.1 Electro-optic sampling of the MIR field

8.1.1 Timing jitter between MIR and visible pulses

The EOS technique requires strict synchronization between a waveform to be characterized and a probe pulse. Large amount of the timing jitter may cause smearing of the waveform. Therefore, we characterize the timing jitter between the MIR pulses and the visible pulses by single-shot spectral interferometry. Especially, in our optical setup, the distant between the beam splitter to the point where the MIR and visible pulses are combined is about 10 meters, which is a quite different and challenging situation compared to most cases (Fig. 6.2).

Figure 8.1 shows a schematic of the experimental setup of the timing-jitter measurement. Instead of using the MIR pulses, we adopted the second harmonic of the shorter-wavelength components of the DW-OPA outputs (~ 1200 nm) and the visible probe pulses, where there exists their spectral overlap around 600 nm. Figure 8.2 shows an example of the single-shot interferogram, from which the relative delay between the two pulses is derived. A collection of the relative delays continuously measured approximately 3300 shots is shown in Fig. 8.3. The standard deviation σ was obtained to be 12.1 fs, which means around 68 percent of the data points are within the range $\pm\sigma = 24.2$ fs if we assume a normal distribution. Although this value is comparable to a 1-cycle of MIR light fields, i.e., not so small, we decided to proceed to EOS because the distribution seems to have a peak shape and we can

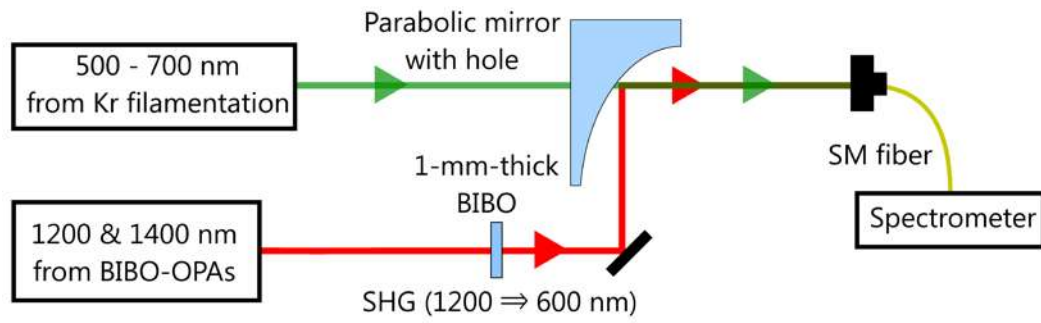


Fig. 8.1: Schematic of the experimental setup of the timing-jitter measurement.

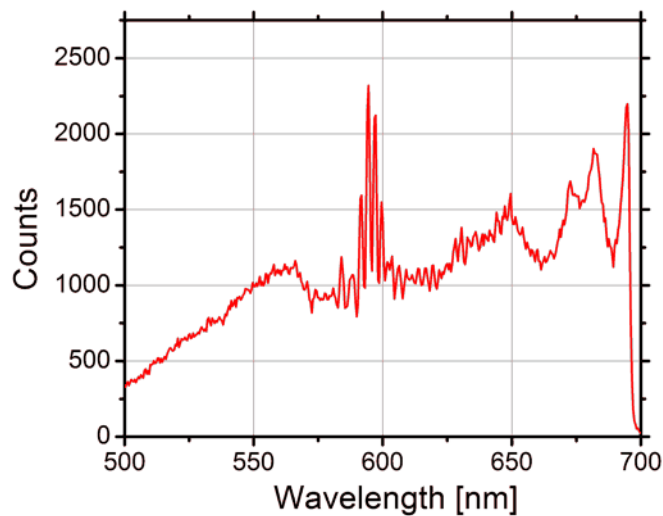


Fig. 8.2: Single-shot interferogram in the timing-jitter measurement.

expect that by just increasing the number of averaging improves the accuracy of the measurement (law of large numbers).

8.1.2 Selection of a nonlinear crystal

A nonlinear crystal for the EOS must fulfill the following two conditions: (i) transparency over the spectral ranges of both a waveform and a probe, (ii) possibility to obtain a crystal thin enough to fulfill the phase-matching condition in a parametric interaction among the waveform, the probe, and resulting sum- or difference-frequency. This condition is related to differential velocity between the phase velocity of the target waveform and the group velocity of the probe pulse. In addition to the above two conditions, large d_{eff} at the phase-matching condition and small dispersion for the target waveforms and the sampling pulses are preferable.

ZnTe, GaP, or GaSe are usually used for the EOS in the MIR. However these crystals are not transparent in the entire spectral range of the visible probe pulses (500-700 nm). In our case, a nonlinear crystal must be transparent from less than 500 nm to over 10 μm . Table 8.1 shows the transmission ranges of MIR crystals.

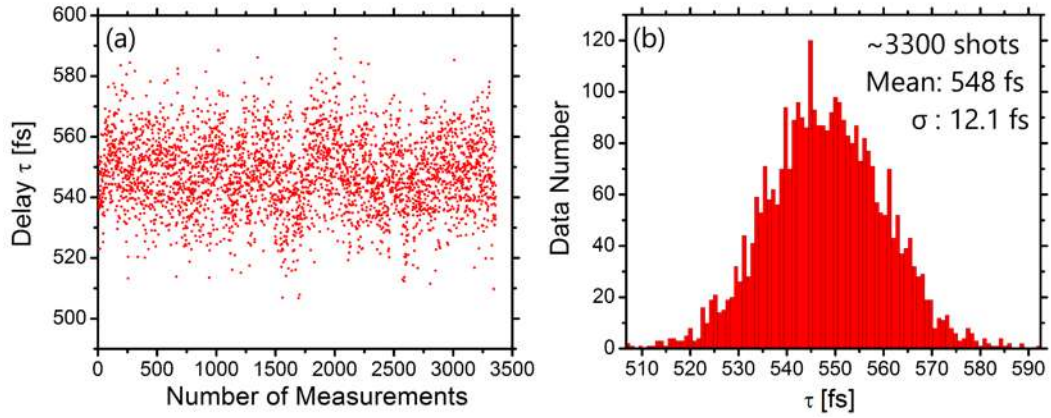


Fig. 8.3: Result of the timing-jitter measurement as a scatter plot (a) and a histogram (b). The mean time of the relative delay was 548 fs and the standard deviation σ was 12.1 fs.

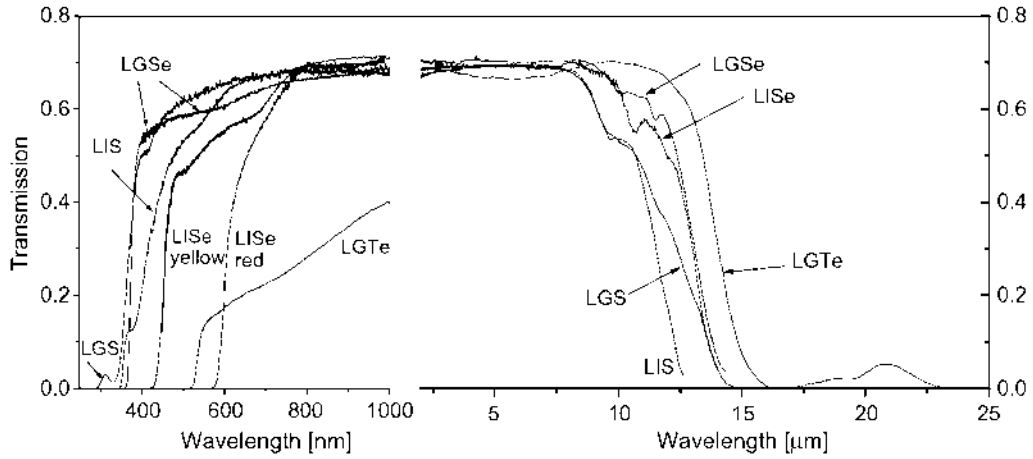


Fig. 8.4: Room-temperature transmission spectra for 2-mm-thick Li-containing ternary chalcogenide crystals in the 0.25–1 μm and 2–25 μm ranges (after annealing in Li_2C vapor) [108].

Lithium-containing chalcogenide crystals, i.e., LiGaS_2 (LGS), LiGaSe_2 (LGSe), and LiInS_2 (LIS), are promising candidates [108]. Figure 8.4 shows the transmission spectra of these crystals.

Among these chalcogenide crystals, because of preferable phase matching bandwidth, we decided to use LGS. Figure 8.5 plots the value of phase mismatch $|\Delta kL|$ of the DFG process between MIR components (horizontal axis) and 600-nm component (fixed) for phase matching in xy -plane of a 100- μm -thick LGS crystal.

The capability of LGS for the EOS has been experimentally checked as seen in Fig 8.6. A 1-mm-thick LGS crystal (xy -plane) was used to generate sum-and difference-frequency components shown by the red and blue lines of Fig. 8.6(b). The whole band of the probe pulse (black line of Fig. 8.6b) is fully either up- or down-converted with the 1-mm-thick LGS crystal, showing its capability in the EOS measurement. Then, the minimum thickness of 15 μm is achieved by careful polish

Tab. 8.1: Overview of the transmission ranges of MIR nonlinear crystals. The largest tensor components are shown as d . Adapted from [130].

MIR nonlinear crystals	Transparency range [μm]	d [pm/V]
Oxide crystals		
KNbO ₃ (KNO)	0.4–4.5	8
KTiOAsO ₄ (KTA)	0.4–4.0	2
KTiOPO ₄ (KTP)	0.4–4.5	2
LiIO ₃ (LIO)	0.3–6.0	2
LiNbO ₃ (LNO)	0.3–5.5	4
LiTaO ₃ (LTO)	0.3–5.5	7
Non-oxide crystals		
AgGaS ₂ (AGS)	0.5–13	23
AgGaSe ₂ (AGSe)	0.7–18	41
CdSiP ₂ (CSP)	0.65–6.5	85
GaSe	0.65–18	54
HgGa ₂ S ₄ (HGS)	0.5–13	31
LiGaS ₂ (LGS)	0.3–12	11
LiGaSe ₂ (LGSe)	0.4–13	18
LiInS ₂ (LIS)	0.4–12	16
LiInSe ₂ (LISe)	0.5–12	16
LiGaTe ₂ (LGT)	0.5–15	42
ZnGeP ₂ (ZGP)	2.0–11	23

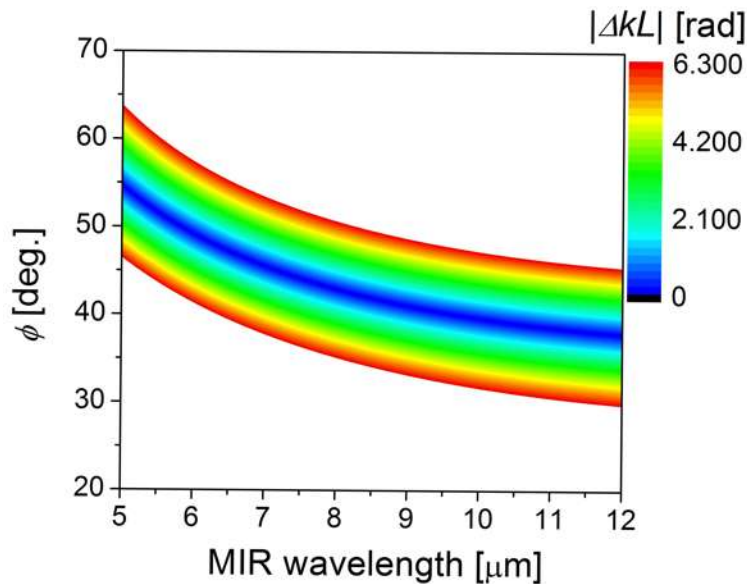


Fig. 8.5: Phase mismatch of the DFG process between MIR components (horizontal axis) and 600-nm component (fixed) for phase matching in xy -plane of a 100- μm -thick LGS crystal, calculated from the Sellmeier equation in Ref. [108].

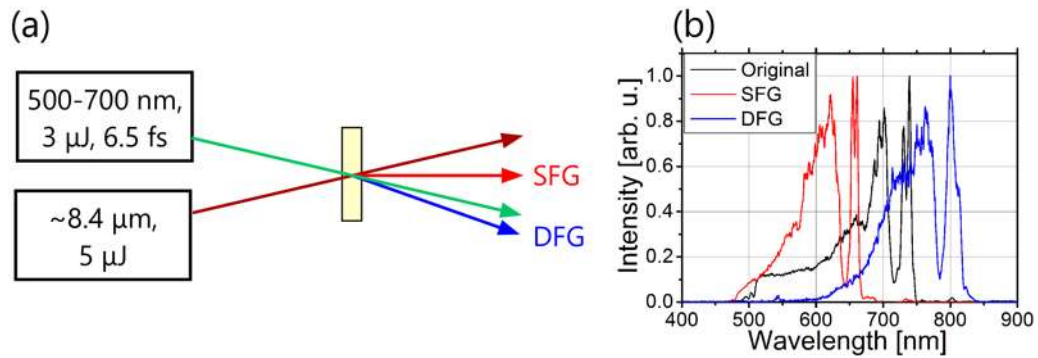


Fig. 8.6: Nonlinear wave mixing between the MIR pulses and the visible pulses in a 1-mm-thick LGS crystal (xy -plane). (a) Schematic of the experimental setup, (b) Obtained results for SFG (red curve) and DFG (blue curve).

(Kogakugiken Corp.) to reduce the smearing effect due to the difference between the phase velocity of the MIR fields and the group velocity of the sampling pulses.

8.1.3 Experimental setup

Figure 8.7 shows a schematic of the experimental setup. The MIR beam and the visible beam are focused onto a 15- μm -thick free-standing LGS crystal by an off-axis parabolic mirror ($f = 100$ mm) and a spherical mirror ($f = 200$ mm), respectively. When the MIR pulses and the visible pulses are spatially and temporally overlapped in the LGS, the polarization state of the visible pulses are modified by the MIR fields. Their focal points are adjusted by using a pinhole and a power-meter to maximize the spatial overlap at the focal position. The middle line, connected to a spectrometer, is used to check the temporal (and spatial) overlap by measuring the spectra of the visible component polarized perpendicular to the input visible probe. After adjusting the overlaps, the visible beam is sent to the bottom line, where the setup for balanced detection is implemented. A narrow band-pass filter ($\lambda_c = 630$ nm, FWHM 10 nm, Edmund Optics Inc.) is used to prevent smearing mainly due to the chromatic dispersion of the following quarter-wave plate (for $\lambda = 632.8$ nm, true-zero order, CRYLIGHT Photonics, Inc.), which is used to add the fixed bias. Then, the visible beam is split by a polarizing beam splitter (Wollaston prism). Two photo detectors (PD) of the same model (DET36A, Thorlabs, Inc.) are employed for balanced detection.

Figure 8.8 shows a schematic of the signal processing electronics. The signals from the two photo detectors are independently pre-amplified (SR240, Stanford Research Systems, Inc.) and fed into a servo controller (LB1005, Newport Corp.), where an output for error monitoring is used to obtain differential signals. Then, the signals are integrated and averaged by SR250 (Stanford Research Systems, Inc.) with the polarity of the signals inverted on every other shot before being added to the moving average. SR250 and an A/D converter are triggered by 1kHz TTL signal synchronized to the light pulses. Note that the MIR pulses are chopped down to 500

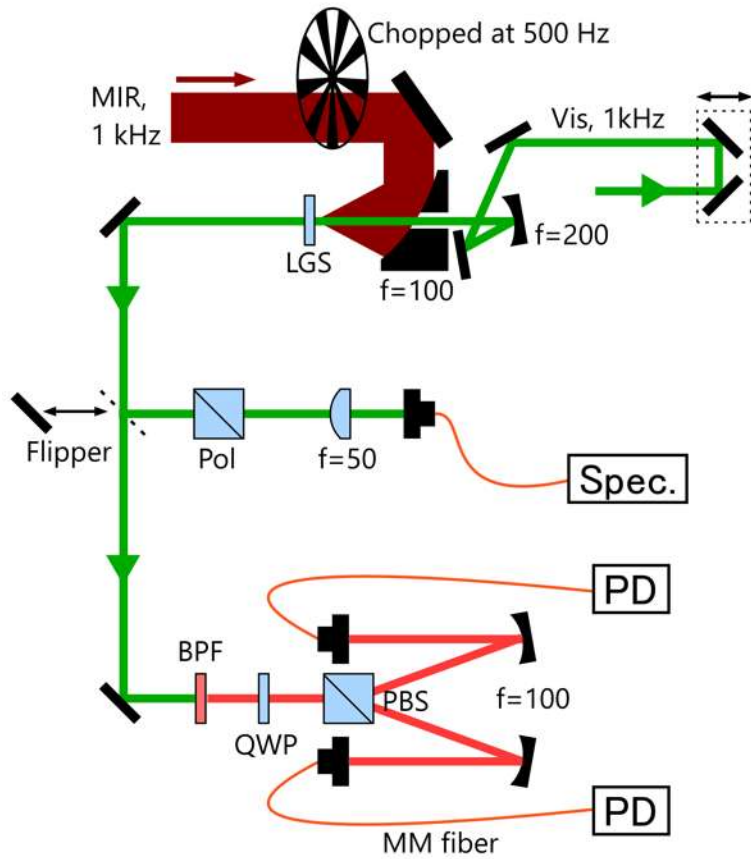


Fig. 8.7: Experimental setup for electro-optic sampling. LGS, 15- μm -thick LGS crystal; Pol, polarizer; BPF, narrow bandpass filter (CWL=630 nm, FWHM=10 nm); QWP, quarter-wave plate; PBS, polarizing beam splitter; MM fiber, multi-mode fiber.

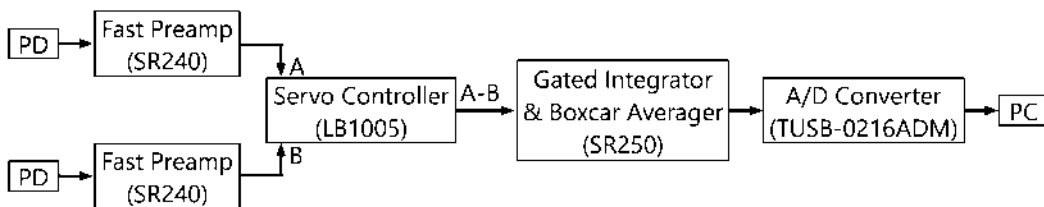


Fig. 8.8: Schematic of the signal processing electronics. PD, photo detector.

Hz by a mechanical chopper (Fig. 8.7) while the visible pulses come in at 1 kHz; therefore, inverting the polarity for every other shot (1kHz) enables us to detect the differential signal between the pump on and pump off. After A/D conversion by TUSB-0216ADM (TURTLE INDUSTRY Co., Ltd.), the signal was read out by a PC and analyzed by a software. This PC is also used to control a delay stage to scan the relative timing between the MIR and the visible.

8.1.4 Results

The gray curve in Fig. 8.9(a) shows a measured waveform. We calibrated this waveform by considering two factors: (i) the temporal resolution determined by the pulse duration of the probe pulses and (ii) the temporal walk-off between the probe and MIR pulses inside the LGS crystal. These factors were considered by defining an effective window function $w(t)$ as

$$w(t) = \int_0^{\Delta\tau} I(t - \tau) d\tau, \quad (8.1)$$

where $I(t)$ is the temporal intensity profile of the probe pulse and $\Delta\tau$ is the difference between the phase delay of the MIR wave and the group delay of the probe pulse in the LGS crystal. In our case, the window function $w(t)$ is mostly determined by the delay time difference $\Delta\tau$ (~ 15 fs). The power spectrum of the measured MIR waveform is divided by the power spectrum of the window function $w(t)$ to obtain a calibrated spectrum, shown as the red curve in Fig. 8.9(b). After the Fourier transform of the calibrated spectrum to the time domain without changing the spectral phase, we obtained a calibrated waveform, shown as the red curve in Fig. 8.9(a). The blue curve in Fig. 8.9(b) shows the group delay of the MIR waveform. The calibrated spectrum (the red curve in Fig. 8.9b) agrees well with the spectrum (the black curve in Fig. 8.9b) measured by a MIR multichannel spectrometer (Infrared Systems Development Corporation, FPAS-6416), which validates the calibration procedure. From the calibrated waveform, the pulse duration was determined to be 70 fs (the full width at half maximum of the intensity distribution). The radius of $1/e^2$ intensity of the MIR beam was measured by a knife-edge method to be 32 μm (Fig. 8.10), corresponding to a peak electric field amplitude of 56 MV/cm at the focal point with a 5- μJ pulse energy. This spot size was about 1.5x diffraction limit.

We also tried an 8-mm-thick LGS crystal in DFG. Figure 8.11 shows the measured MIR field and its spectrum for the case of the 8-mm-thick LGS crystal. The narrowband and relatively long MIR fields (20 μJ , 209 fs, 65 MV/cm) were generated because the phase-matching bandwidth becomes narrow and also the group velocity mismatch between the pump and seed becomes large for thicker crystals. In this case, Wavelength components above 6 μm cannot be generated due to the absorption of the thick LGS crystal (see Fig. 8.4).

We measured the MIR waveforms repeatedly up to ~ 6 hours to evaluate the CEP stability and temporal drift between the MIR and probe pulses. Each scan took 12

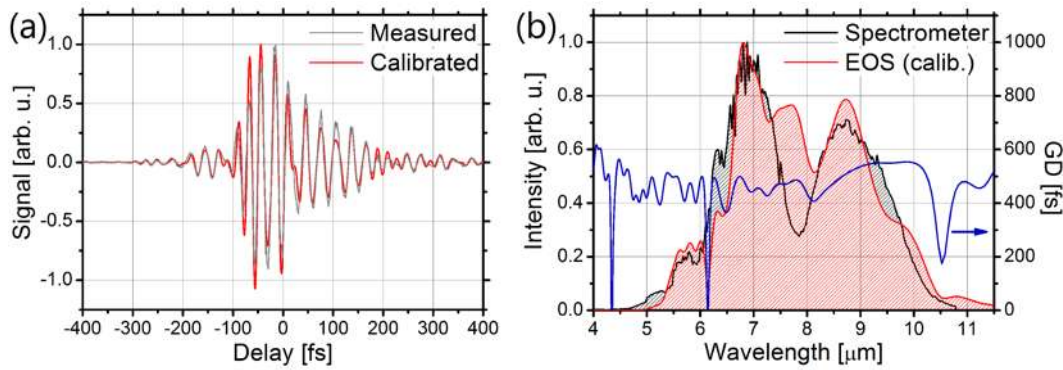


Fig. 8.9: (a) MIR waveform generated in a 1-mm-thick LGS crystal measured by EOS (5 μJ , 70 fs, 56 MV/cm). The gray and red curves are measured and calibrated waveforms, respectively. (b) MIR spectra measured by a MIR spectrometer (black curve) and EOS (red curve). The blue curve is the group delay of the measured waveform.

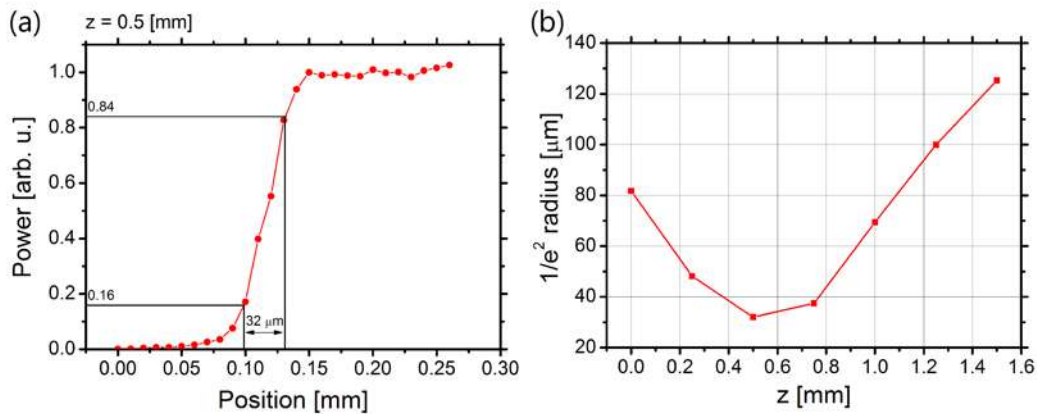


Fig. 8.10: Results of the knife edge measurement.

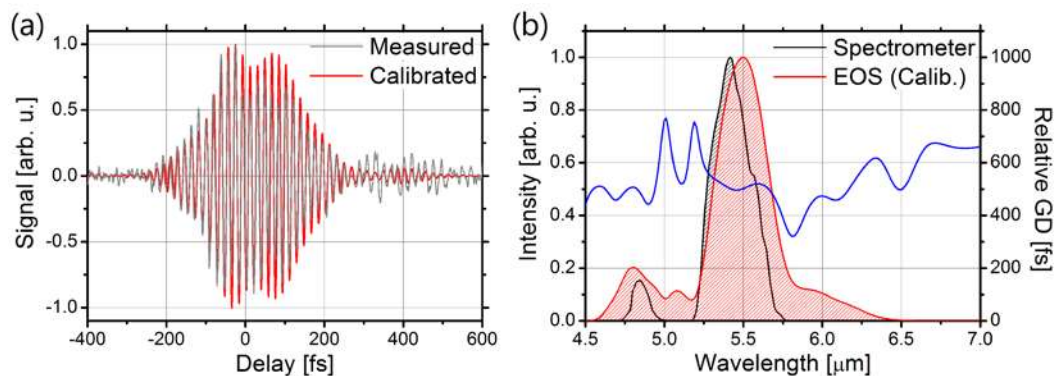


Fig. 8.11: (a) MIR waveform generated in an 8-mm-thick LGS crystal measured by EOS (20 μJ , 209 fs, 65 MV/cm). The gray and red curves are measured and calibrated waveforms, respectively. (b) MIR spectra measured by a MIR spectrometer (black curve) and EOS (red curve). The blue curve is the group delay of the measured waveform.

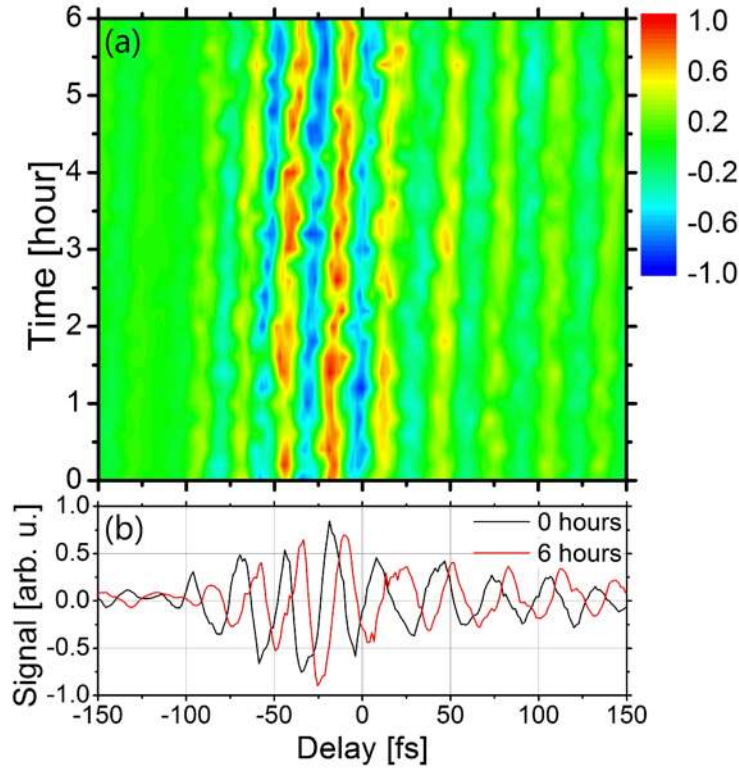


Fig. 8.12: (a) Time evolution of the electro-optically sampled MIR waveforms. (b) Line plots of the waveforms scanned at $t = 0$ and 6 hours.

minutes, and totally 31 scans were taken. Figures 8.12(a, b) show evolution of the MIR waveforms and the waveforms of the first and last scans, respectively. The MIR waveforms show the drift that corresponds to a timing drift of ~ 5 fs over 6 hours. As can be seen in Fig. 8.12(b), the two waveforms are almost identical except the drift. It is likely that this time shift is due to the drift in the differential path length between the MIR and visible probe arms. This drift corresponds to the effective CEP shift of 0.57π rad assuming no timing drift. In the case of MIR generation in DFG using two independent NIR OPAs [131], the long-term CEP stability was reported to be more than π rad over 1 hour without feedback control. Compared to that report, our inline method has better long-term CEP stability by a factor of ~ 10 .

8.2 Summary

In this chapter, the waveform of the CEP-stable MIR fields is characterized using the EOS method by employing a $15\text{-}\mu\text{m}$ -thick LGS crystal, for the first time, to the best of our knowledge. Ultrabroadband MIR pulses generated via DFG in a 1-mm-thick LGS crystals are characterized to have a temporal duration of 2.5 cycles ($5\text{-}11\ \mu\text{m}$, $5\ \mu\text{J}$, 70 fs, 1 kHz), resulting in a peak electric field amplitude of 56 MV/cm. While in the case of DFG in a 8-mm-thick LGS, narrowband long MIR pulses ($\sim 5.5\ \mu\text{m}$, $20\ \mu\text{J}$, 200 fs) were generated, leading to 65 MV/cm. The long term drifts in the CEP and timing between the MIR and probe pulses have been evaluated over

6 hours to be 0.57π rad and approximately 5 fs, respectively. By monitoring the waveforms change during the 6-hour-long measurement, the timing drift seems to be dominant in the system rather than the CEP drift.

Part III

Strong electric field processes in solids
induced by an intense mid-infrared light
source

In this part, we apply the CEP-stabilized intense MIR light source, which was described in Part II, to solids to explore extreme nonlinear phenomena at fields exceeding 10 MV/cm.

In Chap. 10, high-order harmonic generation (HHG) experiments have been conducted using a semiconductor gallium selenide crystal as a target. We demonstrate the ellipsometry of high harmonics radiated from solids, named *high harmonic ellipsometry*. The generated high harmonics and their polarization properties reflect the angstrom-order electronic structures of solids. Furthermore, a drastic transition from *conventional* nonlinear optics to *extreme* nonlinear optics are manifested in crystal-orientation dependence of high harmonic spectra.

In Chap. 11, electron dynamics under the strong MIR fields are explored by sub-cycle transient absorption spectroscopy around the bandgap of solids. With a weak-field excitation, the absorption modulation shows the clear signature of the static Franz-Keldysh effect (FKE). On the other hand, with a strong-field excitation, the absorption spectra are modulated with a clear phase correlation to the driving electric fields, showing the transition from a FKE-originated response to an extremely nonlinear optical response.

Chapter 10

本章については、5年以内に雑誌等で刊行予定のため、非公開。

Chapter 11

本章については、5年以内に雑誌等で刊行予定のため、非公開。

Part IV

Conclusion and outlook

Conclusion and outlook

As my thesis work, I have demonstrated the development of the novel light sources and the novel spectroscopic studies of strong electric field processes of solids. Figures 12.1 and 12.2 are the pictures of the laboratory where I have worked for this thesis. Figure 12.1 was taken when I started my thesis work (March, 2014), and Fig. 12.2 was taken when the light source developments which demonstrated in this thesis was nearly completed (December, 2015). Although I omitted to describe, I started my work from the development of a Ti:sapphire CPA (15 mJ, 40 fs, 1 kHz) which was used to pump the MIR system, starting from scratch. Figure 12.3 shows the layout of the whole laser system.

In Chap. 6, we proposed and demonstrated the novel concept of OPA, which was named as *dual-wavelength OPA*, for the generation of CEP-stable intense MIR pulses. Thanks to this method, CEP-stable MIR fields with a peak electric field exceeding 50 MV/cm, which is enough strong to reach the regime of extreme nonlinear optics (see Fig. 3.4), were generated. For the characterization of the generated MIR fields, we introduced the novel scheme for the generation of sub-10 fs visible pulses with a smooth and stable spectral profile in Chap. 7. By avoiding the use of the fundamental spectral components, the pulse duration was shortened down to 6.5 fs in a simple way. By combining the achievements in Chap. 6 and 7, we have demonstrated the waveform characterization of the MIR fields in Chap. 8. The EOS of MIR fields by visible pulses was enabled by the introduction of a recently developed nonlinear optical crystal, LGS.

In Chap. 10, we proposed and demonstrated the novel spectroscopic concept, which was named as *high harmonic ellipsometry*. Ellipsometric detection of the radiated harmonics enabled us to probe the electronic structure of solids. Furthermore, we observed a dramatic transition from "conventional" nonlinear optics to "extreme" nonlinear optics through the crystal-orientation dependence of harmonics.

In Chap. 11, we tracked the electron dynamics under the irradiation of strong MIR fields by observing the transient absorption around the bandgap. The observations of the Franz-Keldysh oscillation above the bandgap induced by the light field and the coherent electric-field-sign-dependent absorption modulation were demonstrated.



Fig. 12.1: Picture of the laboratory taken in March 2014.



Fig. 12.2: Picture of the laboratory taken in December 2015.

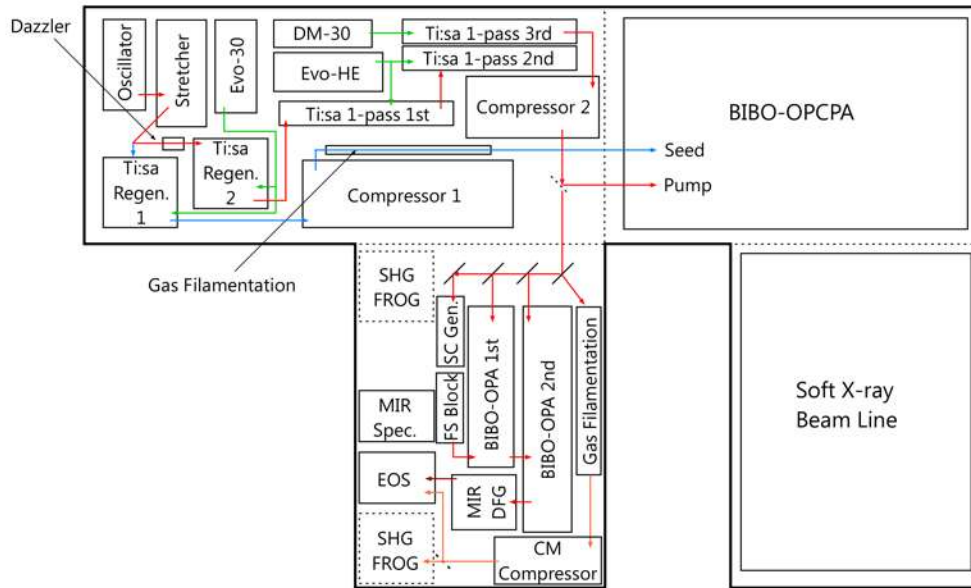


Fig. 12.3: Layout of the developed laser system.

The above experimental results show the possibility of coherent manipulation of crystal electrons by controlling strong light fields, and seem to be opening the way for ultra-high-speed (THz-PHz bandwidth) signal processing by light. I conclude the thesis by discussing the outlook for strong field physics in solids, which is in its dawning.

From the experimental point of view First of all, much more accumulation of the results of systematic experimental studies will be required to deepen the understanding of strong field processes in solids. However, the difficulty of the generation of CEP-stable intense long-wavelength fields is becoming a bottleneck to develop this field. Although I have presented one possible solution in the thesis, i.e. dual-wavelength OPA, further simplification of the experimental setup and improvement of the energy conversion efficiency are desirable. These can be achieved in future by converting Ti:sapphire laser pulses directly into MIR pulses, i.e., by reducing the number of wavelength conversion, which complicates the setup and causes the energy loss. Li-containing chalcogenides like LGS are promising candidates of nonlinear crystals for this scheme.

It is noteworthy here that the air has strong absorption in the MIR, and the operating wavelength of a strong MIR light source should be carefully chosen if the system is operated in the ambient air. Figure 12.4 plots the calculated absorption coefficients of water vapor and carbon dioxide, which dominate the absorption of the air in the MIR range. The high-transmittance region between 8-14 μm is called *the infrared atmospheric window* and suitable for the operation of strong and broadband MIR pulses.

In this thesis, we measured transient absorption on the sub-cycle time scale. This approach can be further elaborated by measuring the phase and polarization of the probe pulses that are expected to be modulated in the sub-cycle time scale as well. In other words, full characterization of the probe pulses will allow us an access to the field-driven electron dynamics in various aspects.

From the theoretical point of view The theory of strong field processes in solids is still not well established because of many difficulties. In addition to that they are essentially many-body problems, many of approximations, e.g., rotating wave approximation (RWA), slowly varying envelope approximation (SVEA), effective mass approximation etc., lost their validity except for the static field approximation. Furthermore, the validity of the band theory is also suspicious because the energies of light matter interaction, i.e., $\hbar\Omega_{\text{tun}}$, $\hbar\Omega_{\text{B}}$, $\hbar\Omega_{\text{R}}$, become comparable or even exceed the energy scales of the bands, i.e., the bandgap energy \mathcal{E}_{g} and the width of the energy dispersion 2Δ (Fig. 2.7). In such situations, it seems necessary to begin with the atomic orbitals as the basis set, and treat quantum mechanical hybridization and interaction with the intense electromagnetic field on the same footing, as pointed out in [138]. The formalism which is not depend on the band theory to treat strong light-matter interaction in solids will be essential for the exact description of the experimental results. The possibility of quantitative prediction, which will lead strong field processes to practical applications, will be the key of the further prosperity of this field.

Considering the rapid development of ultrafast laser technology, new methodology to observe and manipulate crystal electrons on their natural time scales seems to become feasible in near future. I hope my thesis work done here will contribute to establishing the foundation of strong field science in solids.

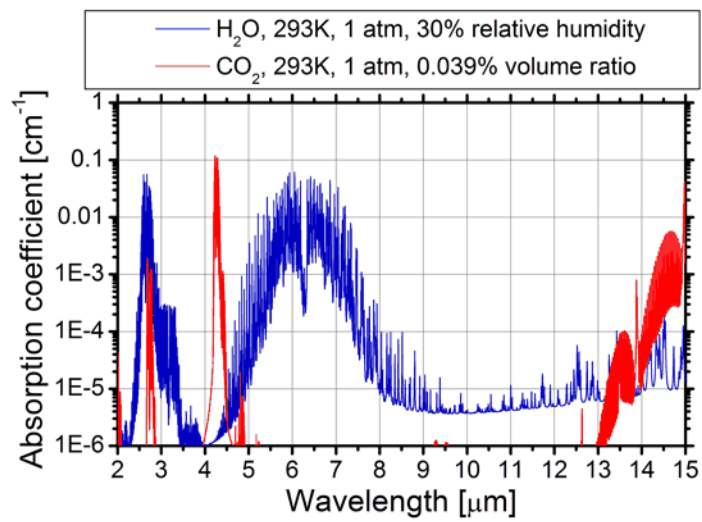


Fig. 12.4: Absorption coefficients of water vapor and carbon dioxide in the air, calculated from HITRAN database [139] by Mr. Takeuchi.

Bibliography

- [1]T. H. Maiman, *Stimulated optical radiation in ruby*, Nature **187**, 493–494 (1960).
- [2]P. A. Franken, A. E. Hill, C. W. Peters, and G. Weinreich, *Generation of optical harmonics*, Phys. Rev. Lett. **7**, 118–119 (1961).
- [3]N. Bloembergen, *Nonlinear optics and spectroscopy*, Rev. Mod. Phys. **54**, 685–695 (1982).
- [4]D. Strickland and G. Mourou, *Compression of amplified chirped optical pulses*, Opt. Commun. **56**, 219–221 (1985).
- [5]G. A. Mourou, T. Tajima, and S. V. Bulanov, *Optics in the relativistic regime*, Rev. Mod. Phys. **78**, 309–371 (2006).
- [6]T. Brabec and F. Krausz, *Intense few-cycle laser fields: Frontiers of nonlinear optics*, Rev. Mod. Phys. **72**, 545 (2000).
- [7]M. Nisoli, S. Stagira, S. De Silvestri, O. Svelto, S. Sartania, Z. Cheng, M. Lenzner, C. Spielmann, and F. Krausz, *A novel-high energy pulse compression system: generation of multigigawatt sub-5-fs pulses*, Appl. Phys. B **65**, 189–196 (1997).
- [8]S. Sartania, Z. Cheng, M. Lenzner, G. Tempea, C. Spielmann, F. Krausz, and K. Ferencz, *Generation of 0.1-TW 5-fs optical pulses at a 1-kHz repetition rate*, Opt. Lett. **22**, 1562–1564 (1997).
- [9]R. Szipöcs, C. Spielmann, F. Krausz, and K. Ferencz, *Chirped multilayer coatings for broadband dispersion control in femtosecond lasers*, Opt. Lett. **19**, 201–203 (1994).
- [10]R. Szipöcs and A. Köhási-Kis, *Theory and design of chirped dielectric laser mirrors*, Appl. Phys. B **65**, 115–135 (1997).
- [11]N. Matuschek, F. X. Kartner, and U. Keller, *Theory of double-chirped mirrors*, IEEE J. Sel. Top. Quantum Electron. **4**, 197–208 (1998).
- [12]M. Wegener, *Extreme nonlinear optics: An introduction*, Advanced Texts in Physics (Springer, 2005).
- [13]S. Hughes, *Breakdown of the area theorem: carrier-wave Rabi flopping of femtosecond optical pulses*, Phys. Rev. Lett. **81**, 3363–3366 (1998).

- [14]S. Hughes, *Subfemtosecond soft-x-ray generation from a two-level atom: Extreme carrier-wave Rabi flopping*, Phys. Rev. A **62**, 055401 (2000).
- [15]O. D. Mücke, T. Tritschler, M. Wegener, U. Morgner, and F. X. Kärtner, *Signatures of carrier-wave Rabi flopping in GaAs*, Phys. Rev. Lett. **87**, 057401 (2001).
- [16]O. D. Mücke, T. Tritschler, M. Wegener, U. Morgner, F. X. Kärtner, G. Khitrova, and H. M. Gibbs, *Carrier-wave Rabi flopping: Role of the carrier-envelope phase*, Opt. Lett. **29**, 2160–2162 (2004).
- [17]T. Tritschler, O. D. Mücke, M. Wegener, U. Morgner, and F. X. Kärtner, *Evidence for third-harmonic generation in disguise of second-harmonic generation in extreme nonlinear optics*, Phys. Rev. Lett. **90**, 217404 (2003).
- [18]T. Tritschler, O. D. Mücke, and M. Wegener, *Extreme nonlinear optics of two-level systems*, Phys. Rev. A **68**, 033404 (2003).
- [19]M. F. Ciappina, J. A. Pérez-Hernández, A. S. Landsman, T. Zimmermann, M. Lewenstein, L. Roso, and F. Krausz, *Carrier-wave Rabi-flopping signatures in high-order harmonic generation for alkali atoms*, Phys. Rev. Lett. **114**, 143902 (2015).
- [20]H. Haug and S. Koch, *Quantum theory of the optical and electronic properties of semiconductors* (World Scientific, 2009).
- [21]W. Schäfer and M. Wegener, *Semiconductor optics and transport phenomena*, Advanced Texts in Physics (Springer, 2002).
- [22]A. P. Jauho and K. Johnsen, *Dynamical Franz-Keldysh effect*, Phys. Rev. Lett. **76**, 4576–4579 (1996).
- [23]K. Johnsen and A.-P. Jauho, *Linear optical absorption spectra of mesoscopic structures in intense THz fields: Free-particle properties*, Phys. Rev. B **57**, 8860–8872 (1998).
- [24]A. H. Chin, J. M. Bakker, and J. Kono, *Ultrafast electroabsorption at the transition between classical and quantum response*, Phys. Rev. Lett. **85**, 3293–3296 (2000).
- [25]D. Volkov, *On a class of solutions of the Dirac equation*, Z. Phys. **94**, 250 (1935).
- [26]H. D. Jones and H. R. Reiss, *Intense-field effects in solids*, Phys. Rev. B **16**, 2466–2473 (1977).
- [27]L. Keldysh, *Ionization in the field of a strong electromagnetic wave*, J. Exp. Theor. Phys. **20**, 1307–1314 (1965).
- [28]A. McPherson, G. Gibson, H. Jara, U. Johann, T. S. Luk, I. A. McIntyre, K. Boyer, and C. K. Rhodes, *Studies of multiphoton production of vacuum-ultraviolet radiation in the rare gases*, J. Opt. Soc. Am. B **4**, 595–601 (1987).

- [29] M. Ferray, A. L'Huillier, X. F. Li, L. Lompre, G. Mainfray, and C. Manus, *Multiple-harmonic conversion of 1064 nm radiation in rare gases*, J. Phys. B **21**, L31 (1988).
- [30] X. F. Li, A. L'Huillier, M. Ferray, L. A. Lompré, and G. Mainfray, *Multiple-harmonic generation in rare gases at high laser intensity*, Phys. Rev. A **39**, 5751–5761 (1989).
- [31] Z. Chang, *Fundamentals of attosecond optics* (Taylor & Francis, 2011).
- [32] S. Haessler, J. Caillat, and P. Salières, *Self-probing of molecules with high harmonic generation*, J. Phys. B **44**, 203001 (2011).
- [33] J. Itatani, J. Levesque, D. Zeidler, H. Niikura, H. Pepin, J. C. Kieffer, P. B. Corkum, and D. M. Villeneuve, *Tomographic imaging of molecular orbitals*, Nature **432**, 867–871 (2004).
- [34] D. Shafir, Y. Mairesse, D. M. Villeneuve, P. B. Corkum, and N. Dudovich, *Atomic wavefunctions probed through strong-field light-matter interaction*, Nat. Phys. **5**, 412–416 (2009).
- [35] S. Haessler, J. Caillat, W. Boutu, C. Giovanetti-Teixeira, T. Ruchon, T. Auguste, Z. Diveki, P. Breger, A. Maquet, B. Carre, R. Taieb, and P. Salieres, *Attosecond imaging of molecular electronic wavepackets*, Nat. Phys. **6**, 200–206 (2010).
- [36] C. Vozzi, M. Negro, F. Calegari, G. Sansone, M. Nisoli, S. De Silvestri, and S. Stagira, *Generalized molecular orbital tomography*, Nat. Phys. **7**, 822–826 (2011).
- [37] W. Franz, *Einfluß eines elektrischen feldes auf eine optische absorptionskante*, Zeitschrift für Naturforschung A **13**, 484–489 (1958).
- [38] L. Keldysh, *The effect of a strong electric field on the optical properties of insulating crystals*, Sov. Phys. JETP **34**, 788–790 (1958).
- [39] Y. Yacoby, *High-frequency Franz-Keldysh effect*, Phys. Rev. **169**, 610–619 (1968).
- [40] K. B. Nordstrom, K. Johnsen, S. J. Allen, A.-P. Jauho, B. Birnir, J. Kono, T. Noda, H. Akiyama, and H. Sakaki, *Excitonic dynamical Franz-Keldysh effect*, Phys. Rev. Lett. **81**, 457–460 (1998).
- [41] J. Hebling, G. Almási, I. Z. Kozma, and J. Kuhl, *Velocity matching by pulse front tilting for large-area THz-pulse generation*, Opt. Express **10**, 1161–1166 (2002).
- [42] H. Hirori, A. Doi, F. Blanchard, and K. Tanaka, *Single-cycle terahertz pulses with amplitudes exceeding 1 MV/cm generated by optical rectification in LiNbO₃*, Appl. Phys. Lett. **98**, 091106 (2011).
- [43] Y. Minami, T. Kurihara, K. Yamaguchi, M. Nakajima, and T. Suemoto, *High-power THz wave generation in plasma induced by polarization adjusted two-color laser pulses*, Appl. Phys. Lett. **102**, 041105 (2013).

- [44]Q. Wu and X.-C. Zhang, *Ultrafast electro-optic field sensors*, Appl. Phys. Lett. **68**, 1604–1606 (1996).
- [45]N. Karpowicz, J. Dai, X. Lu, Y. Chen, M. Yamaguchi, H. Zhao, X.-C. Zhang, L. Zhang, C. Zhang, M. Price-Gallagher, C. Fletcher, O. Mamer, A. Lesimple, and K. Johnson, *Coherent heterodyne time-domain spectrometry covering the entire terahertz gap*, Appl. Phys. Lett. **92**, 011131 (2008).
- [46]Z. Lü, D. Zhang, C. Meng, L. Sun, Z. Zhou, Z. Zhao, and J. Yuan, *Polarization-sensitive air-biased-coherent-detection for terahertz wave*, Appl. Phys. Lett. **101**, 081119 (2012).
- [47]M. C. Hoffmann, J. Hebling, H. Y. Hwang, K.-L. Yeh, and K. A. Nelson, *THz-pump/THz-probe spectroscopy of semiconductors at high field strengths*, J. Opt. Soc. Am. B **26**, A29–A34 (2009).
- [48]T. Kampfrath, K. Tanaka, and K. A. Nelson, *Resonant and nonresonant control over matter and light by intense terahertz transients*, Nat. Photon. **7**, 680–690 (2013).
- [49]A. Pashkin, A. Sell, T. Kampfrath, and R. Huber, *Electric and magnetic terahertz nonlinearities resolved on the sub-cycle scale*, New J. Phys. **15**, 065003 (2013).
- [50]C. W. Luo, K. Reimann, M. Woerner, T. Elsaesser, R. Hey, and K. H. Ploog, *Phase-resolved nonlinear response of a two-dimensional electron gas under femtosecond intersubband excitation*, Phys. Rev. Lett. **92**, 047402 (2004).
- [51]S. Leinß, T. Kampfrath, K. v.Volkman, M. Wolf, J. T. Steiner, M. Kira, S. W. Koch, A. Leitenstorfer, and R. Huber, *Terahertz coherent control of optically dark paraexcitons in Cu₂O*, Phys. Rev. Lett. **101**, 246401 (2008).
- [52]W. Kuehn, P. Gaal, K. Reimann, M. Woerner, T. Elsaesser, and R. Hey, *Coherent ballistic motion of electrons in a periodic potential*, Phys. Rev. Lett. **104**, 146602 (2010).
- [53]B. Zaks, R. B. Liu, and M. S. Sherwin, *Experimental observation of electron-hole recollisions*, Nature **483**, 580–583 (2012).
- [54]S. Fleischer, Y. Zhou, R. W. Field, and K. A. Nelson, *Molecular orientation and alignment by intense single-cycle THz pulses*, Phys. Rev. Lett. **107**, 163603 (2011).
- [55]S. Fleischer, R. W. Field, and K. A. Nelson, *Commensurate two-quantum coherences induced by time-delayed THz fields*, Phys. Rev. Lett. **109**, 123603 (2012).
- [56]K. Kitano, N. Ishii, T. Kanai, and J. Itatani, *Selecting rotational two-level coherence in polar molecules by double terahertz pulses*, Phys. Rev. A **90**, 041402 (2014).
- [57]J. Itatani, F. Quéré, G. L. Yudin, M. Y. Ivanov, F. Krausz, and P. B. Corkum, *Attosecond streak camera*, Phys. Rev. Lett. **88**, 173903 (2002).

- [58] R. Kienberger, E. Goulielmakis, M. Uiberacker, A. Baltuska, V. Yakovlev, F. Bammer, A. Scrinzi, T. Westerwalbesloh, U. Kleineberg, U. Heinzmann, M. Drescher, and F. Krausz, *Atomic transient recorder*, *Nature* **427**, 817–821 (2004).
- [59] E. Goulielmakis, M. Uiberacker, R. Kienberger, A. Baltuska, V. Yakovlev, A. Scrinzi, T. Westerwalbesloh, U. Kleineberg, U. Heinzmann, M. Drescher, and F. Krausz, *Direct measurement of light waves*, *Science* **305**, 1267–1269 (2004).
- [60] M. Schultze, E. M. Bothschafter, A. Sommer, S. Holzner, W. Schweinberger, M. Fiess, M. Hofstetter, R. Kienberger, V. Apalkov, V. S. Yakovlev, M. I. Stockman, and F. Krausz, *Controlling dielectrics with the electric field of light*, *Nature* **493**, 75–78 (2013).
- [61] A. Schiffrin, T. Paasch-Colberg, N. Karpowicz, V. Apalkov, D. Gerster, S. Muhlbrandt, M. Korbman, J. Reichert, M. Schultze, S. Holzner, J. V. Barth, R. Kienberger, R. Ernstorfer, V. S. Yakovlev, M. I. Stockman, and F. Krausz, *Optical-field-induced current in dielectrics*, *Nature* **493**, 70–74 (2013).
- [62] M. Lenzner, J. Krüger, S. Sartania, Z. Cheng, C. Spielmann, G. Mourou, W. Kautek, and F. Krausz, *Femtosecond optical breakdown in dielectrics*, *Phys. Rev. Lett.* **80**, 4076–4079 (1998).
- [63] J. Feldmann, K. Leo, J. Shah, D. A. B. Miller, J. E. Cunningham, T. Meier, G. von Plessen, A. Schulze, P. Thomas, and S. Schmitt-Rink, *Optical investigation of Bloch oscillations in a semiconductor superlattice*, *Phys. Rev. B* **46**, 7252–7255 (1992).
- [64] K. Leo, *High-field transport in semiconductor superlattices*, Springer Tracts in Modern Physics (Springer, 2003).
- [65] A. Sell, A. Leitenstorfer, and R. Huber, *Phase-locked generation and field-resolved detection of widely tunable terahertz pulses with amplitudes exceeding 100 MV/cm*, *Opt. Lett.* **33**, 2767–2769 (2008).
- [66] A. H. Chin, O. G. Calderón, and J. Kono, *Extreme midinfrared nonlinear optics in semiconductors*, *Phys. Rev. Lett.* **86**, 3292–3295 (2001).
- [67] S. Ghimire, A. D. DiChiara, E. Sistrunk, P. Agostini, L. F. DiMauro, and D. A. Reis, *Observation of high-order harmonic generation in a bulk crystal*, *Nat. Phys.* **7**, 138–141 (2011).
- [68] D. Golde, T. Meier, and S. W. Koch, *High harmonics generated in semiconductor nanostructures by the coupled dynamics of optical inter- and intraband excitations*, *Phys. Rev. B* **77**, 075330 (2008).
- [69] O. Schubert, M. Hohenleutner, F. Langer, B. Urbanek, C. Lange, U. Huttner, D. Golde, T. Meier, M. Kira, S. W. Koch, and R. Huber, *Sub-cycle control of terahertz high-harmonic generation by dynamical Bloch oscillations*, *Nat. Photon.* **8**, 119–123 (2014).

- [70]M. Hohenleutner, F. Langer, O. Schubert, M. Knorr, U. Huttner, S. W. Koch, M. Kira, and R. Huber, *Real-time observation of interfering crystal electrons in high-harmonic generation*, *Nature* **523**, 572–575 (2015).
- [71]G. Vampa, C. R. McDonald, G. Orlando, D. D. Klug, P. B. Corkum, and T. Brabec, *Theoretical analysis of high-harmonic generation in solids*, *Phys. Rev. Lett.* **113**, 073901 (2014).
- [72]T. Higuchi, M. I. Stockman, and P. Hommelhoff, *Strong-field perspective on high-harmonic radiation from bulk solids*, *Phys. Rev. Lett.* **113**, 213901 (2014).
- [73]P. G. Hawkins, M. Y. Ivanov, and V. S. Yakovlev, *Effect of multiple conduction bands on high-harmonic emission from dielectrics*, *Phys. Rev. A* **91**, 013405 (2015).
- [74]M. Wu, S. Ghimire, D. A. Reis, K. J. Schafer, and M. B. Gaarde, *High-harmonic generation from Bloch electrons in solids*, *Phys. Rev. A* **91**, 043839 (2015).
- [75]G. Vampa, T. J. Hammond, N. Thire, B. E. Schmidt, F. Legare, C. R. McDonald, T. Brabec, and P. B. Corkum, *Linking high harmonics from gases and solids*, *Nature* **522**, 462–464 (2015).
- [76]T. Tamaya, A. Ishikawa, T. Ogawa, and K. Tanaka, *Diabatic mechanisms of higher-order harmonic generation in solid-state materials under high-intensity electric fields*, *Phys. Rev. Lett.* **116**, 016601 (2016).
- [77]T. T. Luu, M. Garg, S. Y. Kruchinin, A. Moulet, M. T. Hassan, and E. Goulielmakis, *Extreme ultraviolet high-harmonic spectroscopy of solids*, *Nature* **521**, 498–502 (2015).
- [78]G. Ndabashimiye, S. Ghimire, M. Wu, D. A. Browne, K. J. Schafer, M. B. Gaarde, and D. A. Reis, *Solid-state harmonics beyond the atomic limit*, *Nature* **534**, 520–523 (2016).
- [79]M. Garg, M. Zhan, T. T. Luu, H. Lakhota, T. Klostermann, A. Guggenmos, and E. Goulielmakis, *Multi-petahertz electronic metrology*, *Nature* **538**, 359–363 (2016).
- [80]Y. S. You, D. A. Reis, and S. Ghimire, *Anisotropic high-harmonic generation in bulk crystals*, *Nat. Phys.* **advance online publication** (2016) 10.1038/nphys3955.
- [81]H. Liu, Y. Li, Y. S. You, S. Ghimire, T. F. Heinz, and D. A. Reis, *High-harmonic generation from an atomically thin semiconductor*, *Nat. Phys.* **advance online publication** (2016) 10.1038/nphys3946.
- [82]G. Ramian, *The new UCSB free-electron lasers*, *Nucl. Instr. Meth. Phys. Res. A* **318**, 225–229 (1992).

- [83]S. Ghimire, A. D. DiChiara, E. Sistrunk, U. B. Szafruga, P. Agostini, L. F. DiMauro, and D. A. Reis, *Redshift in the optical absorption of ZnO single crystals in the presence of an intense midinfrared laser field*, Phys. Rev. Lett. **107**, 167407 (2011).
- [84]A. Srivastava, R. Srivastava, J. Wang, and J. Kono, *Laser-induced above-band-gap transparency in GaAs*, Phys. Rev. Lett. **93**, 157401 (2004).
- [85]M. Schultze, K. Ramasesha, C. Pemmaraju, S. Sato, D. Whitmore, A. Gandman, J. S. Prell, L. J. Borja, D. Prendergast, K. Yabana, D. M. Neumark, and S. R. Leone, *Attosecond band-gap dynamics in silicon*, Science **346**, 1348–1352 (2014).
- [86]M. Lucchini, S. A. Sato, A. Ludwig, J. Herrmann, M. Volkov, L. Kasmi, Y. Shinohara, K. Yabana, L. Gallmann, and U. Keller, *Attosecond dynamical Franz-Keldysh effect in polycrystalline diamond*, Science **353**, 916–919 (2016).
- [87]I. Ross, *Strong field laser physics*, edited by T. Brabec, Springer Series in Optical Sciences (Springer New York, 2008) Chap. Optical Parametric Amplification Techniques.
- [88]D. Brida, C. Manzoni, G. Cirimi, M. Marangoni, S. Bonora, P. Villoresi, S. De Silvestri, and G. Cerullo, *Few-optical-cycle pulses tunable from the visible to the mid-infrared by optical parametric amplifiers*, J. Opt. **12**, 013001 (2010).
- [89]G. Cerullo, A. Baltuška, O. Mücke, and C. Vozzi, *Few-optical-cycle light pulses with passive carrier-envelope phase stabilization*, Laser Photon. Rev. **5**, 323–351 (2011).
- [90]C. Manzoni, O. D. Mücke, G. Cirimi, S. Fang, J. Moses, S.-W. Huang, K.-H. Hong, G. Cerullo, and F. X. Kärtner, *Coherent pulse synthesis: towards sub-cycle optical waveforms*, Laser Photon. Rev. **9**, 129–171 (2015).
- [91]R. Danielius, A. Piskarskas, A. Stabinis, G. P. Banfi, P. D. Trapani, and R. Righini, *Traveling-wave parametric generation of widely tunable, highly coherent femtosecond light pulses*, J. Opt. Soc. Am. B **10**, 2222–2232 (1993).
- [92]G. Cerullo and S. De Silvestri, *Ultrafast optical parametric amplifiers*, Rev. Sci. Instrum. **74**, 1–18 (2003).
- [93]A. M. Siddiqui, G. Cirimi, D. Brida, F. X. Kärtner, and G. Cerullo, *Generation of < 7 fs pulses at 800 nm from a blue-pumped optical parametric amplifier at degeneracy*, Opt. Lett. **34**, 3592–3594 (2009).
- [94]I. Nikolov, A. Gaydardzhiev, I. Buchvarov, P. Tzankov, F. Noack, and V. Petrov, *Ultrabroadband continuum amplification in the near infrared using BiB₃O₆ nonlinear crystals pumped at 800 nm*, Opt. Lett. **32**, 3342–3344 (2007).

- [95]N. Ishii, K. Kaneshima, K. Kitano, T. Kanai, S. Watanabe, and J. Itatani, *Sub-two-cycle, carrier-envelope phase-stable, intense optical pulses at 1.6 μm from a BiB_3O_6 optical parametric chirped-pulse amplifier*, *Opt. Lett.* **37**, 4182–4184 (2012).
- [96]A. Gaydardzhiev, I. Nikolov, I. Buchvarov, V. Petrov, and F. Noack, *Ultrabroad-band operation of a femtosecond optical parametric generator based on BiB_3O_6 in the near-IR*, *Opt. Express* **16**, 2363 (2008).
- [97]N. Ishii, K. Kaneshima, T. Kanai, S. Watanabe, and J. Itatani, *Generation of ultrashort intense optical pulses at 1.6 μm from a bismuth triborate-based optical parametric chirped pulse amplifier with carrier-envelope phase stabilization*, *J. Opt.* **17**, 094001 (2015).
- [98]Y. Yin, J. Li, X. Ren, K. Zhao, Y. Wu, E. Cunningham, and Z. Chang, *High-efficiency optical parametric chirped-pulse amplifier in BiB_3O_6 for generation of 3 mJ, two-cycle, carrier-envelope-phase-stable pulses at 1.7 μm* , *Opt. Lett.* **41**, 1142–1145 (2016).
- [99]N. Ishii, K. Kaneshima, K. Kitano, T. Kanai, S. Watanabe, and J. Itatani, *Carrier-envelope phase-dependent high harmonic generation in the water window using few-cycle infrared pulses*, *Nat. Commun.* **5**, 3331 EP (2014).
- [100]A. Couairon and A. Mysyrowicz, *Femtosecond filamentation in transparent media*, *Phys. Rep.* **441**, 47–189 (2007).
- [101]R. Boyd, S. Lukishova, and Y. Shen, eds., *Self-focusing: Past and present: Fundamentals and prospects*, *Topics in Applied Physics* (Springer New York, 2008).
- [102]S. Chin, *Femtosecond laser filamentation*, *Springer Series on Atomic, Optical, and Plasma Physics* (Springer New York, 2010).
- [103]M. Bradler, P. Baum, and E. Riedle, *Femtosecond continuum generation in bulk laser host materials with sub- μJ pump pulses*, *Appl. Phys. B* **97**, 561 (2009).
- [104]I. H. Malitson, *Interspecimen comparison of the refractive index of fused silica*, *J. Opt. Soc. Am.* **55**, 1205–1209 (1965).
- [105]V. Petrov, M. Ghotbi, O. Kokabee, A. Esteban-Martin, F. Noack, A. Gaydardzhiev, I. Nikolov, P. Tzankov, I. Buchvarov, K. Miyata, A. Majchrowski, I. Kityk, F. Rotermund, E. Michalski, and M. Ebrahim-Zadeh, *Femtosecond nonlinear frequency conversion based on BiB_3O_6* , *Laser Photon. Rev.* **4**, 53–98 (2010).
- [106]K. Kaneshima, M. Sugiura, K. Tamura, N. Ishii, and J. Itatani, *Ultrabroadband infrared chirped mirrors characterized by a white-light Michelson interferometer*, *Appl. Phys. B* **119**, 347–353 (2015).
- [107]V. Petrov, A. Yelissev, L. Isaenko, S. Lobanov, A. Titov, and J.-J. Zondy, *Second harmonic generation and optical parametric amplification in the mid-IR with orthorhombic biaxial crystals LiGaS_2 and LiGaSe_2* , *Appl. Phys. B* **78**, 543–546 (2004).

- [108]L. Isaenko, A. Yelisseyev, S. Lobanov, P. Krinitsin, V. Petrov, and J.-J. Zondy, *Ternary chalcogenides LiBC₂ (B = In, Ga; C = S, Se, Te) for mid-IR nonlinear optics*, J. Non-Cryst. Solids **352**, 2439–2443 (2006).
- [109]L. Isaenko, A. Yelisseyev, S. Lobanov, P. Krinitsin, V. Petrov, and J.-J. Zondy, *Ternary chalcogenides LiBC₂ (B = In, Ga; C = S, Se, Te) for mid-IR nonlinear optics*, J. Non-Cryst. Solids **352**, 2439–2443 (2006).
- [110]G. Cerullo, M. Nisoli, S. Stagira, and S. D. Silvestri, *Sub-8-fs pulses from an ultrabroadband optical parametric amplifier in the visible*, Opt. Lett. **23**, 1283–1285 (1998).
- [111]A. Shirakawa, I. Sakane, M. Takasaka, and T. Kobayashi, *Sub-5-fs visible pulse generation by pulse-front-matched noncollinear optical parametric amplification*, Appl. Phys. Lett. **74**, 2268–2270 (1999).
- [112]M. Nisoli, S. De Silvestri, and O. Svelto, *Generation of high energy 10 fs pulses by a new pulse compression technique*, Appl. Phys. Lett. **68**, 2793–2795 (1996).
- [113]Y. Matsubara, S. Ogihara, J. Itatani, N. Maeshima, K. Yonemitsu, T. Ishikawa, Y. Okimoto, S.-y. Koshihara, T. Hiramatsu, Y. Nakano, H. Yamochi, G. Saito, and K. Onda, *Coherent dynamics of photoinduced phase formation in a strongly correlated organic crystal*, Phys. Rev. B **89**, 161102 (2014).
- [114]P. B. Corkum, C. Rolland, and T. Srinivasan-Rao, *Supercontinuum generation in gases*, Phys. Rev. Lett. **57**, 2268–2271 (1986).
- [115]A. Braun, G. Korn, X. Liu, D. Du, J. Squier, and G. Mourou, *Self-channeling of high-peak-power femtosecond laser pulses in air*, Opt. Lett. **20**, 73–75 (1995).
- [116]C. Hauri, W. Kornelis, F. Helbing, A. Heinrich, A. Couairon, A. Mysyrowicz, J. Biegert, and U. Keller, *Generation of intense, carrier-envelope phase-locked few-cycle laser pulses through filamentation*, Appl. Phys. B **79**, 673–677 (2004).
- [117]L. Gallmann, T. Pfeifer, P. Nagel, M. Abel, D. Neumark, and S. Leone, *Comparison of the filamentation and the hollow-core fiber characteristics for pulse compression into the few-cycle regime*, Appl. Phys. B **86**, 561–566 (2007).
- [118]B. Prade, M. Franco, A. Mysyrowicz, A. Couairon, H. Buersing, B. Eberle, M. Krenz, D. Seiffert, and O. Vasseur, *Spatial mode cleaning by femtosecond filamentation in air*, Opt. Lett. **31**, 2601–2603 (2006).
- [119]P. E. Ciddor, *Refractive index of air: new equations for the visible and near infrared*, Appl. Opt. **35**, 1566–1573 (1996).
- [120]H. H. Li, *Refractive index of alkaline earth halides and its wavelength and temperature derivatives*, J. Phys. Chem. Ref. Data **9**, 161–290 (1980).
- [121]K. W. DeLong, R. Trebino, J. Hunter, and W. E. White, *Frequency-resolved optical gating with the use of second-harmonic generation*, J. Opt. Soc. Am. B **11**, 2206–2215 (1994).

- [122]A. Baltuska, M. S. Pshenichnikov, and D. A. Wiersma, *Second-harmonic generation frequency-resolved optical gating in the single-cycle regime*, IEEE J. Quant. Electron. **35**, 459–478 (1999).
- [123]D. Grischkowsky, S. Keiding, M. van Exter, and C. Fattinger, *Far-infrared time-domain spectroscopy with terahertz beams of dielectrics and semiconductors*, J. Opt. Soc. Am. B **7**, 2006–2015 (1990).
- [124]Q. Wu and X.-C. Zhang, *Free-space electro-optics sampling of mid-infrared pulses*, Appl. Phys. Lett. **71**, 1285–1286 (1997).
- [125]C. Kübler, R. Huber, S. Tübel, and A. Leitenstorfer, *Ultrabroadband detection of multi-terahertz field transients with GaSe electro-optic sensors: approaching the near infrared*, Appl. Phys. Lett. **85**, 3360–3362 (2004).
- [126]R. Huber, A. Brodschelm, F. Tauser, and A. Leitenstorfer, *Generation and field-resolved detection of femtosecond electromagnetic pulses tunable up to 41 THz*, Appl. Phys. Lett. **76**, 3191–3193 (2000).
- [127]K. Liu, J. Xu, and X.-C. Zhang, *GaSe crystals for broadband terahertz wave detection*, Appl. Phys. Lett. **85**, 863–865 (2004).
- [128]T. Kampfrath, J. Nötzold, and M. Wolf, *Sampling of broadband terahertz pulses with thick electro-optic crystals*, Appl. Phys. Lett. **90**, 231113 (2007) 10.1063/1.2746939.
- [129]S. Keiber, S. Sederberg, A. Schwarz, M. Trubetskov, V. Pervak, F. Krausz, and N. Karpowicz, *Electro-optic sampling of near-infrared waveforms*, Nat. Photon. **10**, 159–162 (2016).
- [130]H. Pires, M. Baudisch, D. Sanchez, M. Hemmer, and J. Biegert, *Ultrashort pulse generation in the mid-IR*, Prog. Quantum Electron. **43**, 1–30 (2015).
- [131]C. Manzoni, M. Först, H. Ehrke, and A. Cavalleri, *Single-shot detection and direct control of carrier phase drift of midinfrared pulses*, Opt. Lett. **35**, 757–759 (2010).
- [132]N. Ferneliuss, *Properties of gallium selenide single crystal*, Prog. Cryst. Growth Charact. Mater. **28**, 275–353 (1994).
- [133]K. Ueno, H. Abe, K. Saiki, A. Koma, H. Oigawa, and Y. Nannichi, *Hetero-epitaxy of layered compound semiconductor GaSe onto GaAs surfaces for very effective passivation of nanometer structures*, Surf. Sci. **267**, 43–46 (1992).
- [134]I. Catalano, A. Cingolani, A. Minafra, and C. Paorici, *Second harmonic generation in layered compounds*, Opt. Commun. **24**, 105–108 (1978).

- [135]X. Gonze, B. Amadon, P.-M. Anglade, J.-M. Beuken, F. Bottin, P. Boulanger, F. Bruneval, D. Caliste, R. Caracas, M. Côté, T. Deutsch, L. Genovese, P. Ghosez, M. Giantomassi, S. Goedecker, D. Hamann, P. Hermet, F. Jollet, G. Jomard, S. Leroux, M. Mancini, S. Mazevet, M. Oliveira, G. Onida, Y. Pouillon, T. Rangel, G.-M. Rignanese, D. Sangalli, R. Shaltaf, M. Torrent, M. Verstraete, G. Zerah, and J. Zwanziger, *Abinit: first-principles approach to material and nanosystem properties*, *Comput. Phys. Commun.* **180**, 2582–2615 (2009).
- [136]T. Otake, Y. Shinohara, S. A. Sato, and K. Yabana, *Femtosecond time-resolved dynamical Franz-Keldysh effect*, *Phys. Rev. B* **93**, 045124 (2016).
- [137]T. G. Pedersen and T. B. Lyngé, *Analytic Franz-Keldysh effect in one-dimensional polar semiconductors*, *J. Phys. Condens. Matter* **15**, 3813 (2003).
- [138]Y. Mizumoto, Y. Kayanuma, A. Srivastava, J. Kono, and A. H. Chin, *Dressed-band theory for semiconductors in a high-intensity infrared laser field*, *Phys. Rev. B* **74**, 045216 (2006).
- [139]L. Rothman, I. Gordon, Y. Babikov, A. Barbe, D. C. Benner, P. Bernath, M. Birk, L. Bizzocchi, V. Boudon, L. Brown, A. Campargue, K. Chance, E. Cohen, L. Coudert, V. Devi, B. Drouin, A. Fayt, J.-M. Flaud, R. Gamache, J. Harrison, J.-M. Hartmann, C. Hill, J. Hodges, D. Jacquemart, A. Jolly, J. Lamouroux, R. L. Roy, G. Li, D. Long, O. Lyulin, C. Mackie, S. Massie, S. Mikhailenko, H. Müller, O. Naumenko, A. Nikitin, J. Orphal, V. Perevalov, A. Perrin, E. Polovtseva, C. Richard, M. Smith, E. Starikova, K. Sung, S. Tashkun, J. Tennyson, G. Toon, V. Tyuterev, and G. Wagner, *The HITRAN2012 molecular spectroscopic database*, *Journal of Quantitative Spectroscopy and Radiative Transfer* **130**, 4–50 (2013).

List of Publications

Peer-Reviewed Journal Papers

As Primary Author

- **K. Kaneshima**, K. Takeuchi, N. Ishii, and J. Itatani, “*Generation of spectrally stable 6.5-fs visible pulses via filamentation in krypton,*” High Power Laser Science and Engineering, **4**, e17 (2016).
- **K. Kaneshima**, N. Ishii, K. Takeuchi, and J. Itatani, “*Generation of carrier-envelope phase-stable mid-infrared pulses via dual-wavelength optical parametric amplification,*” Optics Express, **24**, 8660-8665 (2016).
- **K. Kaneshima**, M. Sugiura, K. Tamura, N. Ishii, and J. Itatani, “*Ultrabroadband infrared chirped mirrors characterized by a white-light Michelson interferometer,*” Applied Physics B, **119**, 347-353 (2015).

As Co-Author

- H. Geiseler, N. Ishii, **K. Kaneshima**, F. Geier, T. Kanai, O. I. Tolstikhin, T. Morishita, and J. Itatani, “*Carrier-envelope phase mapping in laser-induced electron diffraction,*” Physical Review A, **94**, 033417 (2016).
- N. Ishii, **K. Kaneshima**, T. Kanai, S. Watanabe, and J. Itatani, “*Generation of ultrashort intense optical pulses at 1.6 μm from a bismuth triborate-based optical parametric chirped pulse amplifier with carrier-envelope phase stabilization,*” Journal of Optics, **17**, 094001 (2015).
- N. Ishii, **K. Kaneshima**, K. Kitano, T. Kanai, S. Watanabe, and J. Itatani, “*Carrier-envelope phase-dependent high harmonic generation in the water window using few-cycle infrared pulses,*” Nature Communications, **5**, Article number 3331 (2014).
- H. Geiseler, N. Ishii, **K. Kaneshima**, K. Kitano, T. Kanai, and J. Itatani, “*High-energy half-cycle cutoffs in high harmonic and rescattered electron spectra using waveform-controlled few-cycle infrared pulses,*” Journal of Physics B, **47**, 204011 (2014).

- H. Geiseler, N. Ishii, **K. Kaneshima**, T. Kanai, and J. Itatani, “Long-term passive stabilization of the carrier-envelope phase of an intense infrared few-cycle pulse source,” *Applied Physics B*, **117**, 941-946 (2014).
- N. Ishii, **K. Kaneshima**, K. Kitano, T. Kanai, S. Watanabe, and J. Itatani, “Sub-two-cycle, carrier-envelope phase-stable, intense optical pulses at 1.6 μm from a BiB_3O_6 optical parametric chirped-pulse amplifier”, *Optics Letters*, **37**, 4182-4184 (2012).

Presentations in International Conferences

As Primary Author

- **K. Kaneshima**, N. Ishii, K. Takeuchi, J. Itatani, “Generation of CEP-stable Mid-infrared Fields Exceeding 20 MV/cm,” the 20th International Conference on Ultrafast Phenomena, Santa Fe (USA), (2016.7) (Oral)
- **K. Kaneshima**, N. Ishii, K. Takeuchi, J. Itatani, “Waveform characterization of CEP-stable intense mid-infrared pulses generated via dual-wavelength OPA,” Conference on Lasers and Electro-Optics 2016, San Jose (USA), (2016.6) (Oral)
- **K. Kaneshima**, N. Ishii, J. Itatani, “Tunable mid-IR pulse generation via frequency-selective optical parametric amplification,” Ultrafast Optics 2015, Beijing (CHN), (2015.8) (Oral)
- **K. Kaneshima**, “Tunable mid-IR pulse generation via frequency-selective optical parametric amplification,” Joint IMPRS-MPC-AS Workshop, Max Planck Institute of Quantum Optics and Technical University of Munich, Munich (DEU), 2015.6 (Oral)
- **K. Kaneshima**, “Millijoule few-cycle IR OPCPA for the generation of high harmonics in the water window,” Joint IMPRS-MPC-AS Workshop, Max Planck Institute of Quantum Optics and Technical University of Munich, Munich (DEU), 2015.6 (Poster)
- **K. Kaneshima**, N. Ishii, T. Kanai, S. Watanabe, J. Itatani, “Laser-Based Soft X-ray Light Source Resolving X-ray Absorption Near Edge Structure at the Carbon K Edge,” Conference on Lasers and Electro-Optics 2015, San Jose (USA), (2015.5) (Postdeadline, Oral)

As Co-Author

- H. Geiseler, N. Ishii, **K. Kaneshima**, T. Kanai, T. Morishita, and J. Itatani, “Carrier-Envelope Phase Mapping in Laser-Induced Electron Rescattering,” The High-Intensity Lasers and High-Field Phenomena (HILAS), Long Beach (USA), (2016.3) (Oral)

- H. Geiseler, N. Ishii, **K. Kaneshima**, T. Kanai, J. Itatani, “*Generation of Millijoule Infrared Few-Cycle Pulses and Their Application to Strong-Field Experiments*,” Ultrafast Optics 2015, Beijing (CHN), (2015.8) (Oral)
- H. Geiseler, N. Ishii, F. Geier, **K. Kaneshima**, T. Kanai, and J. Itatani, “*Carrier-Envelope Phase Mapping of Laser-Induced Electron Scattering*,” 5th International Conference on Attosecond Physics (ATTO2015), Saint-Sauveur (CAN), (2015.7) (Oral)
- N. Ishii, **K. Kaneshima**, T. Kanai, S. Watanabe, and J. Itatani, “*High-Resolution Absorption Spectroscopy at the Carbon K Edge Using Isolated Soft X-Ray Continua Generated by Millijoule Few-Cycle IR Pulses*,” 5th International Conference on Attosecond Physics, Saint-Sauveur (CAN), (2015.7) (Oral)
- N. Ishii, **K. Kaneshima**, T. Kanai, S. Watanabe, and J. Itatani, “*Development of a Millijoule Few-Cycle IR Light Source and its Application to High-Flux High Harmonics in the Water Window*,” Conference on Lasers and Electro-Optics – European Quantum Electronics Conference 2015, Munich (DEU), (2015.6) (Oral)
- N. Ishii, **K. Kaneshima**, T. Kanai, S. Watanabe, and J. Itatani, “*Sub-Two-Cycle Millijoule Optical Pulses at 1600 nm from a BiB_3O_6 Optical Parametric Chirped-Pulse Amplifier*,” Conference on Lasers and Electro-Optics 2015, San Jose (USA), (2015.5) (Oral)
- N. Ishii, **K. Kaneshima**, T. Kanai, S. Watanabe, and J. Itatani, “*Generation of 1.5 mJ Few-Cycle Infrared Pulses in a BiB_3O_6 Optical Parametric Chirped Pulse Amplifier*,” The 4th Advanced Lasers and Photon Sources (ALPS’15), Yokohama (JPN), (2015.4) (Oral)
- H. Geiseler, N. Ishii, **K. Kaneshima**, F. Geier, T. Kanai, J. Itatani, “*Looking into Sub-Cycle Dynamics of Electron Rescattering Induced by Intense Infrared Few-Cycle Pulses*,” The 4th Advanced Lasers and Photon Sources (ALPS’15), Yokohama (JPN), (2015.4) (Oral)
- Henning Geiseler, Nobuhisa Ishii, **K. Kaneshima**, Teruto Kanai, Jiro Itatani, “*Probing Atomic Structure with Carrier-Envelope Phase-Stable Few-Cycle Pulses in the Infrared*,” Frontiers in Optics/Laser Science (FiO/LS) 2014, Tucson (USA), (2014.10) (Poster)
- N. Ishii, **K. Kaneshima**, K. Kitano, T. Kanai, S. Watanabe, and J. Itatani, “*Generation of Isolated Soft X-Ray Pulses Around the Carbon K-Edge Using CEP-Stabilized Few-Cycle IR Pulses*,” 19th International Conference on Ultrafast Phenomena, Ginowan (JPN), (2014.7) (Poster)

- H. Geiseler, N. Ishii, **K. Kaneshima**, T. Kanai, and Jiro Itatani, “*Probing Elastic Rescattering through Half-Cycle Cutoffs in Above-Threshold Ionization Spectra*,” 19th International Conference on Ultrafast Phenomena, Ginowan (JPN), (2014.7) (Oral)
- H. Geiseler, N. Ishii, **K. Kaneshima**, K. Kitano, T. Kanai, and J. Itatani, “*Extraction of Elastic Scattering Cross Sections from Half-Cycle Cutoffs in Photoelectron Spectra*,” Conference on Lasers and Electro-Optics 2014 QELS Fundamental Science, San Jose (USA), (2014.6) (Oral)
- N. Ishii, **K. Kaneshima**, H. Geiseler, T. Kanai, S. Watanabe, J. Itatani, “*Isolated Attosecond Continua in the Water Window via High Harmonic Generation using a Few-cycle Infrared Light Source*,” Conference on Lasers and Electro-Optics 2014: Science and Innovations, San Jose (USA), (2014.6) (Oral)
- N. Ishii, **K. Kaneshima**, H. Geiseler, K. Kitano, T. Kanai, S. Watanabe, and J. Itatani, “*Generation of Coherent Continua in Soft X-Rays using a Carrier-envelope Phase-controlled Few-cycle Infrared Light Source*,” The 3rd Advanced Lasers and Photon Sources (ALPS’14), Yokohama (JPN), (2014.4) (Invited, Oral)
- N. Ishii, **K. Kaneshima**, K. Kitano, T. Kanai, S. Watanabe, and J. Itatani, “*Generation of isolated attosecond continua in the water window using CEP-locked, few-cycle IR pulses from a BiB₃O₆ OPCPA system*,” 4th International Conference on Attosecond Physics (ATTO2013), Paris (FRA), (2013.7) (Oral)
- N. Ishii, **K. Kaneshima**, K. Kitano, T. Kanai, S. Watanabe, and Jiro Itatani, “*Carrier-Envelope Phase-Dependent High Harmonic Generation in the Water Window by Few-Cycle IR Pulses*,” Conference on Lasers and Electro-Optics 2013, San Jose (USA), (2013.6) (Oral)
- N. Ishii, **K. Kaneshima**, K. Kitano, T. Kanai, S. Watanabe, and J. Itatani, “*Carrier-Envelope Phase-Dependent High-Harmonic Generation in the Water Window Using a Few-Cycle Infrared Light Source*,” Conference on Lasers and Electro-Optics Europe, Munich (DEU), (2013.5) (Oral)
- N. Ishii, **K. Kaneshima**, K. Kitano, T. Kanai, S. Watanabe, and J. Itatani, “*Carrier-envelope phase-dependent high harmonic generation in the water window by use of waveform-controlled infrared pulses*,” Ultrafast Optics 2013, Davos (CHE), (2013.3) (Postdeadline, Oral)
- N. Ishii, **K. Kaneshima**, K. Kitano, T. Kanai, S. Watanabe, and J. Itatani, “*Sub-two-cycle, CEP-stabilized, millijoule-class IR optical pulses from a BiB₃O₆-based OPCPA using Ti:sapphire lasers*,” Ultrafast Optics 2013, Davos (CHE), (2013.3) (Oral)

- N. Ishii, **K. Kaneshima**, K. Kitano, T. Kanai, S. Watanabe, and J. Itatani, “*CEP-dependent HHG in the water window by few-cycle, sub-mJ IR OPCPA*,” Gordon Research Conference on Multiphoton Process, South Hadley (USA), (2012.6) (Poster)
- N. Ishii, K. Kitano, **K. Kaneshima**, T. Kanai, S. Watanabe, and J. Itatani, “*Nearly-octave, sub-two-cycle, CEP-locked, intense IR pulses from BIBO OPCPA using 810-nm pump pulses*,” Conference on Laser and Electro-Optics 2012, San Jose (USA), (2012.5) (Oral)

Acknowledgment

Here, I would like to thank all the people who helped me to achieve the results presented in this thesis.

First and foremost I would like to express my gratitude to Prof. Jiro Itatani for his supervision of my PhD study. He guided me with many thoughtful suggestions and provided me the ideal environment for experimental work. Without the warm and stimulating atmosphere in his group, I could not finish my thesis.

Just as much I would like to thank Dr. Nobuhisa Ishii. From my first day in the group, he shared his extensive scientific knowledge and experimental skills with me, which are almost everything I know in the Lab. Without him, I would have been totally lost my way.

I am deeply obliged to Prof. Hiroshi Okamoto, my assistant supervisor in the MERIT Course, for his kind advice and encouragement.

I would like to show my appreciation to Prof. Kenichi L. Ishikawa and Dr. Yasushi Shinohara for the fruitful discussions on high harmonic ellipsometry.

I am indebted to Muneo Sugiura and Koichi Tamura from Tokai Optical Co., Ltd., for their excellent work on design and production of dielectric mirrors.

I would like to acknowledge Kengo Takeuchi for his hard work and his contribution to the pointing stability measurement of the visible pulses. I would like to thank Teruto Kanai and Florian Geier for their help in improving and maintaining the laboratory environment.

The collaborative researches with Prof. Yoichi Okimoto and Tsugumi Umanodan for an organic ferroelectric material, and with Takeshi Morimoto for strongly correlated materials were fruitful for me, although I could not include the obtained results in the thesis.

I am grateful to all the colleagues in our group, namely Dr. Kenta Kitano, Dr. Jost Henning Geiseler, Dr. Faming Lu, Dr. Tomoya Mizuno, Tianjiao Shao, Justinas Pupeikis, Yoshiyuki Matsumoto, and Nariyuki Saito, for their kindness and encouragement of the research. I also appreciate the kind support of Tomoko Igarashi.

I would also like to thank all the other colleagues whom I couldn't mention here for creating an excellent atmosphere to work in ISSP.

I would like to thank very much Prof. Junji Yumoto, Prof. Fumio Komori, Prof. Shingo Katsumoto, Prof. Takeo Kato, and Dr. Takuro Ideguchi for refereeing and improving the present thesis.

I gratefully acknowledge the financial supports of the MERIT Course and the JSPS Research Fellowship for Young Scientists.

Finally, I would like to express special thanks to my parents, Takakazu and Kayoko Kaneshima, for their kind support and understanding.

